Bralower, T.J., Premoli Silva, I., Malone, M.J., et al., 2002
Proceedings of the Ocean Drilling Program, Initial Reports Volume 198

5. Site 1209[1]

Shipboard Scientific Party[2]

PRINCIPAL RESULTS

Background

Site 1209 is located in middle bathyal (2387 m) water depth close to the most elevated, central part of the Southern High of Shatsky Rise. The site is located on seismic line TN037-14A (Fig. F1). This profile is hard to correlate with other profiles on the southern and western flanks of the Southern High that are tied to drill holes. A tentative predrilling correlation with the Southern High seismic units of Sliter and Brown (1993) suggests a moderately thick Unit 1 (Neogene), an expanded Unit 2 (Paleogene), and a moderately thick Unit 3 (Upper Cretaceous). The site is close to the point where the stratigraphic sequence appears to be most complete; however, the section was expected to contain a number of minor disconformities as indicated by prominent horizontal reflectors. The total thickness of the sedimentary section at Site 1209 is estimated at ~1147 m. Basement underlying the site was formed during Magnetochron CM20 in the Tithonian (Nakanishi et al., 1989).

The major goals of Site 1209 drilling were to core a shallow, relatively expanded Paleogene and uppermost Cretaceous section. Holes 1209A and 1209B were cored largely with the advanced piston corer (APC). Only two cores were taken with the extended core barrel (XCB). Hole 1209C was drilled down to the lower Miocene, and then the Oligocene to Maastrichtian section was cored. The three holes terminated at different levels in the Maastrichtian due to difficulty penetrating chert horizons with the XCB center bit. The deepest recovered sediment was early Maastrichtian in age from 297.6 meters below seafloor (mbsf) in Hole 1209B.

Coring recovered a relatively thin (111.2 m) lower Miocene to Holocene (0–16.4 Ma) section of nannofossil ooze, clayey nannofossil ooze, and nannofossil ooze with clay (lithologic Unit I) (Fig. F2). This unit

F1. Interpretation of seismic reflection profile, Site 1209, p. 37.

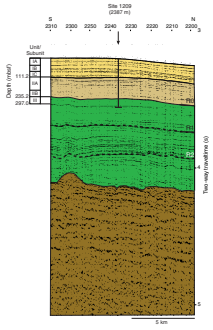

F2. Coring results, Site 1209, p. 38.

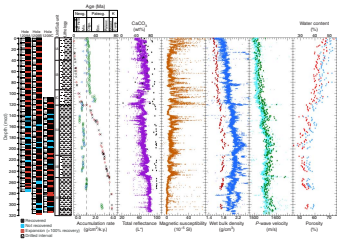

[1]Examples of how to reference the whole or part of this volume.
[2]Shipboard Scientific Party addresses.

Ms 198IR-105

has an unconformity (11.19 to 15.1 Ma) separating the uppermost middle Miocene and the uppermost lower Miocene. Lithologic Unit I rests unconformably on lithologic Unit II (111.2 and 235 mbsf), which consists of nannofossil ooze and nannofossil ooze with clay of early Oligocene to early Paleocene age (28.6–65 Ma). Preliminary nannofossil and planktonic foraminiferal biostratigraphy suggests that the succession is largely complete. However, minor unconformities may be present, especially in the upper to middle Eocene interval (between 38 and 42 Ma) that is characterized by low sedimentation rates. Underlying lithologic Unit III of Maastrichtian age (65 to 70 Ma) is composed of nannofossil ooze and chert. Three prominent chert layers were encountered in the ~50-m Maastrichtian section in Hole 1209C. However, no horizons were found in the same interval in Hole 1209B, suggesting that chert layers are laterally discontinuous. The ooze surrounding the chert at the bottom of each hole was often still fluid and almost completely unlithified.

Summary of Results

The upper middle Miocene to Holocene section at Site 1209 is apparently continuous and similar to contemporaneous sequences at Sites 1207 and 1208. Unconformities from the lower to middle Miocene and the lower Miocene to the lower Oligocene are partially equivalent to those observed at Sites 1207 and 1208, suggesting that regional oceanographic processes controlling erosion and dissolution had a major effect on sedimentation. The Neogene section at Site 1209 was deposited at much lower sedimentation rates than at the other sites, at least partially as a result of the lower production of biosiliceous and carbonate materials. Moreover, sedimentation at Site 1209 was exclusively pelagic, whereas the other two sites appear to have received a large supply of fine sediment from bottom water currents and eolian transport. A progression of decimeter- to meter-scale orbital cycles is observed in the sedimentary record at Site 1209. Preliminary ages suggest that dominant frequencies are eccentricity (100 k.y.) subsequent to 0.6 Ma, obliquity (40 k.y.) from 0.6 to 2.5 Ma, and then a gradual transition from long obliquity (1.25 m.y.) to long eccentricity (400 k.y.) to eccentricity (100 k.y.) through the lower Neogene and Paleogene section.

The lower Maastrichtian to lower Oligocene section at Site 1209 is also apparently complete. The highlights of Site 1209 coring were clearly associated with the recovery of the sedimentary record of several critical events in this interval, most of them in multiple holes. These include the Eocene–Oligocene transition, the Paleocene–Eocene Thermal Maximum (PETM), a prominent biological event in the early late Paleocene, the Cretaceous/Tertiary (K/T) boundary, and the mid-Maastrichtian deepwater event (MME). Sediments are almost completely unlithified, and the site appears to have remained above the calcite composite depth (CCD) for most of this time interval; hence, foraminiferal preservation is good to excellent. The stable isotope and paleontological records from Site 1209 will provide important information on the nature of environmental changes during the critical events and their effect on marine biotas. Site 1209 will provide a firm shallow end-member in the Shatsky Rise depth transect.

Highlights

Eocene–Oligocene Transition

The Eocene to Oligocene transition represents the true end of the "greenhouse" world of the Mesozoic and Early Cenozoic. Although this transition occurred over a period of several million years, stable isotopic records reveal that much of the cooling occurred over a relatively brief (350 k.y.) interval in the earliest Oligocene known as Oi-1 (33.15–33.5 Ma) (e.g., Miller et al., 1991; Zachos et al., 1996). The deep oceans cooled by ~3°C during Oi-1, and large permanent ice-sheets became established in Antarctica (Zachos et al., 1992a, 1992b). Current reconstructions of ocean temperature and chemistry for the Eocene–Oligocene transition, however, are based primarily on pelagic sediments collected in the Atlantic and Indian Oceans (Miller et al., 1987; Zachos et al., 1996). Very few sections suitable for such work have been recovered from the Pacific (e.g., Miller and Thomas, 1985). As a consequence, we still lack a robust understanding of how global ocean chemistry or circulation evolved in response to high-latitude cooling and glaciation.

The Eocene/Oligocene boundary was recovered in Cores 198-1209A-14H, 198-1209B-14H and 15H, and 198-1209C-4H. Preliminary nannofossil and planktonic foraminiferal biostratigraphy suggests that the boundary interval is complete. The most marked feature in the transition record at Site 1209 is a gradual change, over ~7.5 m in the lowermost Oligocene and uppermost Eocene, from light brown to tan nannofossil ooze with clay to a light gray to white nannofossil ooze. A similar lithologic transition was observed in an identical stratigraphic position at Site 1208. However, the Site 1208 record is far more condensed than the Site 1209 record.

The distinctive color change in the Site 1209 record reflects a pronounced deepening in the CCD. This oceanwide event is thought to be related to the intensification of ocean circulation and/or to increased continental weathering (Zachos et al., 1996). Cycles from within the transition show that the transition was nonlinear and likely affected by orbital climatic variations. This observation will help constrain the cause of deepening of the CCD. Planktonic and benthic foraminiferal preservation in this interval is moderate. Thus, stable isotope stratigraphies from Site 1209 have the potential to provide a firm understanding of the evolution of Pacific surface and deep waters through this important climatic transition.

Paleocene–Eocene Thermal Maximum

At the other end of the climatic spectrum from the Eocene–Oligocene transition, the PETM is an abrupt and short-term (~210 k.y.) warming event at ~55.5 Ma that led to major transformation of marine plankton and benthos. This climatic event involved an increase of some 8°C of high-latitude surface water temperature and some 5°C of deep ocean water temperature. Warming is thought to have been driven by the input of a massive quantity of greenhouse gas, most likely methane, into the ocean-atmosphere system (e.g., Dickens et al., 1995). The response of the tropics and the Pacific Ocean to this climatic event is currently poorly known (Bralower et al., 1995).

The PETM at Site 1209 corresponds to a 12.5-cm-thick medium brown layer of clayey nannofossil ooze with a sharp basal contact and a gradational upper contact. This horizon was recovered in Sections 198-

1209A-21H-7, 198-1209B-22H-1, and 198-1209C-11H-3. The detailed lithostratigraphy of the three PETM records recovered varies significantly on a millimeter scale as a result of deformation of the soft horizons during coring and splitting. Core 198-1209C-11H shows the most complete upper Paleocene to lower Eocene transition as indicated by multisensor track (MST) data. The event corresponds to a sharp change from a white nannofossil ooze to a brown nannofossil ooze with clay (Fig. **F3**). In Hole 1209B, these two lithologies are separated by an extremely thin (1 mm) dark brown clay seam. In the other two holes, this seam has been disturbed during coring and splitting.

The micropaleontological record of the PETM interval is summarized in Figure **F3.** Preliminary biostratigraphy shows that the event lies toward the top of nannofossil Zone CP8 and planktonic foraminiferal Zone P5. In addition, a single specimen of *Gavelinella beccariiformis,* a benthic foraminiferal species that goes extinct at the onset of the PETM (e.g., Thomas, 1990) was found in Section 198-1209A-21H-CC, several decimeters below the event (see **"Biostratigraphy,"** p. 16). The abrupt decrease in the nannofossil *Fasciculithus* that occurs just above the PETM in other sections (Bralower et al., 1995, 1997; Aubry et al., 1996; Monechi et al., 2000) lies at the top of the clayey nannofossil ooze layer at Site 1209 (Fig. **F3**). The PETM layer corresponds to a prominent magnetic susceptibility peak followed by a 6- to 7-m interval of relatively high susceptibility that shows cyclic variation. The top of the event is currently undefined. However, preliminary biostratigraphy—in particular the first occurrence (FO) of the nannofossil *Discoaster diastypus* that lies 1.73 m above the base of the PETM (between Samples 198-1209A-21H-5, 130 cm, and 21H-6, 30 cm), and the last occurrence (LO) of the planktonic foraminifer *Morozovella velascoensis* that lies 2.38 m above the base of the event (between 198-1209A-21H-5, 129–130 cm, and 49–50 cm)—indicates that the section is condensed compared to continental margin records from the Atlantic and Tethys (i.e., Kennett and Stott, 1991; Norris and Röhl, 1999; Röhl et al., 2000).

The PETM interval is associated with dramatic turnover in nannofossil assemblages. One of the dominant nannolith genera, *Fasciculithus,* is replaced by *Zygrhablithus bijugatus,* a nannolith that is often a highly abundant or dominant component of Eocene assemblages (Fig. **F3**). The genus *Discoaster* is often highly abundant within the event itself, likely as a result of warming or increased oligotrophy (Bralower, in press). Common to abundant calcispheres are found in sediments from the PETM interval at Site 1209. These fossils are likely produced by calcareous dinoflagellates during intervals of adverse surface water conditions.

Low-latitude planktonic foraminiferal assemblages in the PETM also experienced a significant transformation with the sudden appearance of an ephemeral group of ecophenotpyes or new species of the genera *Acarinina* and *Morozovella* (Kelly et al., 1996). The range of these transient taxa is limited to the interval of the carbon isotope excursion; hence, they are known as the "excursion" taxa. Although preliminary observations did not yield any of the end-member excursion taxa, several forms that are intermediate between the true excursion taxa and their ancestors were observed. No detailed observations were made on benthic foraminifers at Site 1209 because of sampling limitations.

The response of the CCD is a sensitive indicator of change in carbon cycling during the PETM, likely as a result of the input of large quantities of methane into the ocean-atmosphere system (e.g., Dickens et al., 1997). This response can be monitored by changes in carbonate content and preservation. Nannofossil preservation below the event at Site 1209

F3. Paleontological summary of the PETM interval, p. 39.

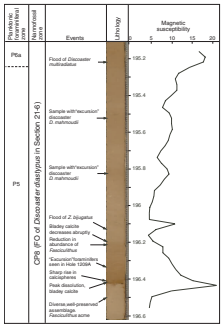

is moderate, indicating that the site was located in the broad range of the lysocline. Preservation declines markedly in the 1-mm clay lens at the base of the event as shown by pervasive etching of coccolith shields and nannolith rims. Preservation remains poor for several centimeters above this level, but nannofossils never completely disappear from the record. This interval of poor preservation is accompanied by a high abundance of bladey rhombs that may be reprecipitated calcite. The deterioration in nannofossil preservation is evidence for an abrupt rise in the level of the CCD and lysocline during the PETM. The effects of this rise are not nearly as dramatic at Site 1209 as at Site 1208, which was situated almost 1 km deeper (see **"Principal Results,"** p. 1, in the "Site 1208" chapter).

Mid-Paleocene Biological Event

A prominent, 23-cm thick, dark brown nannofossil ooze with clay was found in Sections 198-1209A-23H-3, 198-1209B-23H-5, and 198-1209C-12H-CC. This layer shows a sharp magnetic susceptibility increase and a slight density decrease. Preliminary micropaleontological investigations suggest that this interval may represent a previously unrecognized event of considerable evolutionary significance. This interval lies within planktonic foraminiferal Zone P4 and coincides exactly with the evolutionary FO of the nannolith *Heliolithus kleinpellii,* an important component of late Paleocene assemblages and a marker for the base of Zone CP5. The interval immediately below the brown ooze layer contains significant numbers of the species *Bomolithus elegans,* which may be the ancestor of *H. kleinpellii.* The abundance of *H. kleinpellii* increases sharply in a transitional interval at the base of the brown ooze layer. Planktonic foraminifers in the ooze layer are characterized by a low-diversity, largely dissolved assemblage dominated by representatives of the genus *Igorina*. This low-diversity assemblage suggests some kind of oceanic perturbation.

A contemporaneous and prominent magnetic susceptibility peak was found on the Blake Nose at Site 1051 (U. Röhl et al., unpubl. data); this peak is associated with a dark brown chalk and correlates almost exactly with the FO of *H. kleinpellii.* Isotopic and further paleontological investigations are required to understand the oceanographic conditions that gave rise to this mid-Paleocene event as well as the detailed evolutionary relationships of the key taxa.

Cretaceous/Tertiary Boundary

At Site 1209 the base of lithologic Unit II coincides with the K/T boundary, marked by a significant lithologic change from uppermost Maastrichtian, white to very pale orange nannofossil ooze to basal Paleocene, darker grayish orange foraminiferal nannofossil ooze. This boundary is located in Sections 198-1209A-25H-6 and 198-1209C-15H-3 but occurs within an unrecovered interval in Hole 1209B. The most complete boundary sequence is found in Hole 1209C. Here the top of the Maastrichtian is slightly indurated, possibly indicating an incipient hardground, and overlain by lowermost Paleocene mottled, light orange, slightly indurated foraminiferal nannofossil ooze that grades into softer and paler tan-gray nannofossil ooze. The lowermost Paleocene layer is strongly bioturbated as shown by the pale orange roots within the irregular surface of the top of the white Maastrichtian ooze (Fig. **F4**). The basal Paleocene unit is ~14 cm thick and overlain by a 23-cm-thick

pure white ooze. In Hole 1209A, the uppermost Maastrichtian white nannofossil ooze is separated from the lowermost Paleocene light orange foraminiferal nannofossil ooze by a watery, disturbed, orange brown clay horizon. This horizon was formed by disturbance during coring and splitting and does not correspond to the "clay horizon" that defines the K/T boundary in classic sections such as El Kef, Tunisia; Caravaca, southern Spain; and Gubbio (Bottaccione), Italy.

The micropaleontological record of the K/T interval is summarized in Figure **F4.** Preliminary biostratigraphy shows the well-known abrupt change in nannofossil and planktonic foraminiferal assemblages. The white nannofossil ooze (Hole 1209A: sample F2) yields a diverse, but dissolved, highly fragmented fauna of the latest Maastrichtian *Abathomphalus mayaroensis* planktonic foraminiferal Zone; the washed residue also contains rare, minute, well-preserved heterohelicids, predominantly *Guembelitria,* that suggests a possible preservation of Zone P0 fauna in the deepest burrows. Nannofossil assemblages below this interval (Hole 1209A: sample N1) are diverse, well preserved, and include relatively common *Micula prinsii* indicating correlation to the uppermost Maastrichtian nannofossil Zone CC26. The light orange foraminiferal nannofossil ooze burrows (Hole 1209C: sample F1) yield highly abundant, minute (<100 µm), and well-preserved planktonic foraminiferal assemblages that are dominated by heterohelicids and belong to the basal Paleocene *Parvularugoglobigerina eugubina* (Pα) Zone. Nannofossils in the gray orange ooze (Hole 1209C: sample N2) are limited to "disaster" taxa (calcispheres) and reworked Cretaceous taxa. In the overlying pale nannofossil ooze horizon, the average size of the foraminiferal assemblage increases associated with increasing abundance of trochospiral forms with respect to heterohelicids (Hole 1209A: sample F3; Hole 1209C: sample F2). The lower part of the white ooze unit (Hole 1209C: sample N3; Hole 1209A: Sample N4) is dominated by ultrafine micrite, calcispheres, and the survivor coccolith taxon *Cyclagelosphaera reinhardtii*. Finally, the upper part of the white ooze unit (Hole 1209C: sample N4) contains fine micrite, *C. reinhardtii,* another survivor, *Markalius inversus,* and small species of the Danian coccolith genus *Neobiscutum*. This whole interval thus belongs to nannofossil Subzone CP1a. In Hole 1209A, the orange-brown soupy clay, containing a late Danian planktonic fauna, coats indurated ooze above the burrows fragmented by drilling.

The lowermost 2–3 cm of basal Paleocene darker grayish orange foraminiferal nannofossil ooze contains common spherules, probably altered tektites. The thin (1–2 cm) boundary clay unit that corresponds to planktonic foraminiferal Zone P0 in a few deep-sea and shelf sites (e.g., El Kef, Tunisia; and Caravaca, southern Spain) is not found at this site. However, Zone P0 fauna seems to be present in the deepest burrows.

We postulate that this interval has been affected by bioturbation soon after the boundary (Fig. **F4**). Nevertheless, the substantial thickness of the uppermost Maastrichtian *M. prinsii* (CC26) Zone and the lowermost Danian Pα Zone at Site 1209 indicates that the K/T boundary is paleontologically complete. In most deep sea-sites, the Pα Zone is either unrecovered or poorly preserved. Thus, the section represents one of the best preserved and least disrupted deep-sea records of this major extinction event, as well as of the subsequent radiation.

F4. Paleontological summary of K/T boundary, Holes 1209A and 1209C, p. 40.

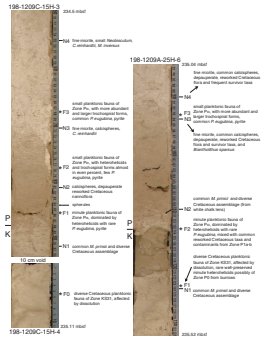

Mid-Maastrichtian Event

The long-term cooling of the Late Cretaceous was interrupted by a dramatic event in the mid-Maastrichtian (~69–70 Ma; nannofossil Zone CC24), when oceanic deep waters appear to have switched abruptly from low- to high-latitude sources (e.g., MacLeod and Huber, 1996; Frank and Arthur, 1999). This event appears to have coincided with the extinction of the inoceramid bivalves. Growing evidence, however, suggests that this biotic event is distinctly diachronous in the Atlantic, Tethys, and Pacific Oceans (MacLeod et al., 1996). Moreover, the magnitude and direction of stable isotope changes are quite variable from site to site (Frank and Arthur, 1999), possibly as a result of uncertainties in stratigraphic correlation or of true differences in deepwater properties.

The MME appears to have been recovered in Section 198-1209C-21H-1, which lies in nannofossil Zone CC24. In this section and several below it, large inoceramid prisms can be seen with the naked eye. Although the LO of inoceramids has not yet been determined in Hole 1209C, the abrupt disappearance is a likely sign of the event. Shore-based stable isotopic and benthic assemblage studies will help us refine our understanding of the origin and implications of this deepwater change.

BACKGROUND AND OBJECTIVES

Site 1209 is located in middle bathyal (2387 m) water depth close to the most elevated, central part of the Southern High of Shatsky Rise. According to the reconstruction of Nakanishi et al. (1989), basement underlying the site was formed in the latest Jurassic within Magnetochron M20 (~145 Ma). Site 1209 is the shallowest site in the Leg 198 transect. The paleodepth of this site was ~550 m in the early Maastrichtian based on the estimate of Barrera et al. (1997) for Site 305. However, subsidence likely occurred more rapidly than typical crust (e.g., McNutt et al., 1990).

The site is located on seismic line TN037-14A (Fig. **F1**). This profile is difficult to correlate with other profiles on the southern and western flanks of the Southern High that have drill hole control. A tentative predrilling correlation with the Southern High seismic units of Sliter and Brown (1993) suggests a moderately thick Unit 1 (Neogene), an expanded Unit 2 (Paleogene), and a moderately thick Unit 3 (Upper Cretaceous). The site is close to the point where the stratigraphic sequence appears to be most complete; however, the section is expected to contain a number of minor disconformities as indicated by prominent, horizontal reflectors. The total thickness of the sedimentary section at Site 1209 is estimated at ~1147 m.

The major goals of Site 1209 drilling are to core a shallow, relatively expanded Paleogene and uppermost Cretaceous section. Our drilling strategy was to double APC/XCB core the sequence down to the first thick chert horizon, then to drill through the Neogene to core the Paleogene and uppermost Cretaceous in a third hole. The site will be included in broad leg-based objectives that include

1. Reconstructing changes in the properties of surface and deep waters through the Late Cretaceous and Paleogene. This will help to constrain the character and stability of intermediate- and

deepwater circulation, vertical thermal gradients, and basin fractionation during ancient intervals of extreme warmth as well as during transitions from and to cooler intervals.
2. Shedding light on the origin of abrupt climatic events such as the Eocene/Oligocene boundary, the PETM, late Paleocene and early Eocene hyperthermals, and the mid-Maastrichtian event. The depth transect will also help address questions concerning the nature of chemical (i.e., CCD, nutrients, and oxygenation) and physical oceanographic changes (i.e., temperature gradients) during these events.
3. Studying changes in biotic assemblages through time and relating them to fluctuations in temperature and nutrients over long time periods as well as during transient climatic events.
4. Understanding the origin of orbital cycles in the sedimentary record and determining the origin of these cycles using biotic and geochemical data.
5. Using independently generated biostratigraphy, magnetostratigraphy, and orbital stratigraphy to improve the Paleogene and Late Cretaceous timescale.

OPERATIONS

Transit from Site 1208 to Site 1209

The 210-nmi transit to Site 1209 was made in 18.4 hr at an average speed of 11.4 kt. Upon arriving on site, the thrusters and hydrophones were lowered, and the ship was switched over to dynamic positioning mode, initiating Site 1209 at 0755 hr on 18 September.

Hole 1209A

An APC/XCB bottom-hole assembly (BHA) was assembled, and the bit was positioned above the seafloor at 2397.0 meters below rig floor (mbrf). Hole 1209A was officially spudded at 1405 hr on 18 September, recovering 8.21 m, which established a seafloor depth of 2398.3 mbrf, or 2387.2 meters below sea floor (mbsl) (Table T1). APC coring continued through Core 26H to a depth of 245.7 mbsf. An incomplete stroke on Core 26H led to abandoning APC coring in favor of using the XCB. Recovery with the APC averaged 101.9%. Cores 4H through 26H were oriented. Coring with the XCB continued through Core 198-1209-28X to a depth of 259.6 mbsf. Coring was terminated after 30 min of rotating time on a hard layer, presumably chert, with no advancement. The drill string was tripped up, clearing the seafloor at 1335 hr on 19 September, ending drilling at Hole 1209A.

T1. Coring summary, p. 80.

Hole 1209B

After offsetting the drill ship 15 m north, the drill string was spaced out with the bit placed 3.0 m higher than the spudding depth of Hole 1209A. Hole 1209B was spudded at 1454 hr on 19 September. Recovery on the first core measured 5.16 m, yielding a seafloor depth of 2398.4 mbrf, or 2387.4 mbsl. APC coring advanced to a depth of 297.6 mbsf through Core 32H with 98.2% recovery. Cores 4H through 32H were oriented, and Adara temperature shoe deployments were made on Cores 6H, 8H, 10H, and 12H. Three of the Adara tool measurements

were good quality, but the tool deployed with Core 6H failed. Core 32H was not a complete piston stroke; hence, an XCB center bit was deployed to drill through the presumed chert layer. With 1.5 hr of rotating time and only 0.4 m advancement, we decided to terminate coring in Hole 1209B. While attempting to recover the XCB center bit, we discovered that a sub on the pulling tool had backed off. In addition, the forward wireline was damaged, which required 150 m of line to be removed. While effecting repairs, the aft wireline was used in an attempt to fish the core stub of the pulling tool. However, after two unsuccessful attempts, we had to trip the drill string back to the ship, clearing the rig floor at 0710 hr on 21 September and ending drilling at Hole 1209B.

Hole 1209C

The ship was offset 15 m east of Hole 1209A, and Hole 1209C was spudded at 1155 hr on 21 September. The hole was drilled to a depth of 98.0 mbsf, and then APC coring was initiated, continuing to a depth of 251.5 mbsf. At this depth, Core 17H contacted chert after stroking ahead only 1.5 m. An XCB center bit was deployed, drilling ahead to 252.5 mbsf. APC coring resumed (Cores 198-1209C-18H and 19H), progressing to 264.9 mbsf before encountering another chert layer. The XCB center bit was used to drill ahead to a depth of 268.4 mbsf. The next APC core barrel (Core 20H) failed to fully stroke, and shear pins in the overshot connecting the nonmagnetic sinker bars failed. This barrel was recovered after a second wireline run, and core orientation activities were suspended to avoid further complications with the nonmagnetic components. APC coring continued with Cores 21H and 22H to 296.9 mbsf, where a chert layer impeded progress. The XCB center bit was deployed and used to advance the hole through chert to 299.7 mbsf. While attempting to shoot APC Core 198-1209C-23H, the pins failed to shear and the barrel did not penetrate into the formation. Upon recovery, this barrel was inspected and seals were changed to ensure that the barrel was functioning correctly. It was redeployed, but the pins did not shear again. We then switched to the XCB to determine if the problem was related to the APC barrel or the BHA. XCB Core 23X was advanced to 307.5 mbsf; however, despite latching properly, the barrel was recovered empty. A final APC core was attempted, but the APC barrel could not be landed correctly. Convinced that there was a mechanical problem with the bit and/or lockable float valve (LFV), coring was suspended, and the drill string was retrieved. Total recovery for Hole 1209C was 99.2%, with APC recovery averaging 103%.

At 0425 hr on 23 September, the pipe cleared the rotary table on the rig floor, ending operations at Site 1209. A subsequent inspection of the coring assembly showed that the primary bit was heavily damaged on the inner row cutters and that the flapper hinge pin in the LFV was broken (Fig. F5). Chert was found behind the flapper, likely preventing it from fully opening when the core barrels attempted to pass through. This resulted in overloading the flapper hinge, leading to the failure.

LITHOSTRATIGRAPHY

Description of Lithologic Units

The 297 m of sediment cored in three holes at Site 1209 consists largely of nannofossil ooze and nannofossil ooze with clay (Fig. F6).

F5. Damaged bit and LFV, p. 41.

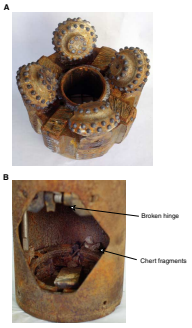

F6. Core recovery, lithologic units, age with corresponding biostratigraphic zonations, color reflectance, and percent carbonate, p. 42.

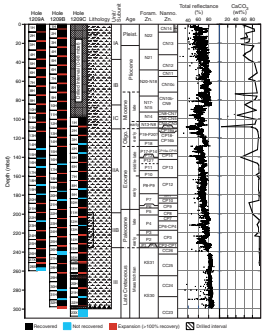

Several discrete clay-rich units representing condensed intervals are also present. Minor components throughout the sequence include foraminifers, diatoms, and radiolarians. Other minor to trace components include pyrite, Fe-oxides, and zeolites. Volcanic glass is a disseminated trace component concentrated in a few discrete ash layers in the Neogene portion of the sequence. Both the Neogene and Paleogene are characterized by pervasive color/lithologic cycles on decimeter to meter scales.

The sequence has been subdivided into three major lithologic units. In Hole 1209A, Unit I extends from 0 to 111.2 mbsf, the base of an upper lower Miocene unconformity. The unit consists primarily of nannofossil ooze with clay interbedded with clayey nannofossil ooze and nannofossil ooze. These variations are expressed as decimeter-scale light–dark color cycles. Unit II begins at the base of a condensed interval and/or unconformity at 111.2 mbsf representing the Oligocene/Miocene boundary and extends to 235.2 mbsf, the base of the Cenozoic. It consists of alternating nannofossil ooze and ooze with clay and contains several discrete centimeter-thick clay-rich horizons. Unit II is distinguished from Unit I by higher carbonate contents and more oxidized, reddish colored sediments, as indicated by higher red/blue ratios (Fig. F7). Unit III extends from the K/T boundary at 235.2 mbsf to the lower Maastrichtian at the bottom of the drilled section at 297 mbsf and consists primarily of very pale orange (10YR 8/2) to white (N9) nannofossil ooze.

F7. Magnetic susceptibility and color reflectance red/blue ratio, Hole 1209B, p. 43.

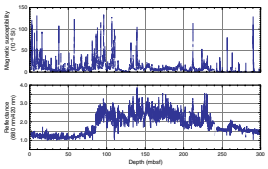

Lithologic Unit I

Intervals: 198-1209A-1H-1, 0 cm, through 12H-6, 50 cm; 198-1209B-1H-1 through 13H-1, 130 cm; and 198-1209C-1H-1, 0 cm, through 2H-3, 23 cm
Depths: 0.0 to 111.2 mbsf in Hole 1209A, 0 to 110.63 mbsf in Hole 1209B, and 0 to 110.73 mbsf in Hole 1209C
Age: Holocene to early Miocene

Unit I has been subdivided into three subunits (Fig. F6). Subunit IA extends from 0 to 37 mbsf in Hole 1209A (Holocene to upper Pliocene). It consists mostly of alternating nannofossil ooze with clay and clayey nannofossil ooze, and is characterized by relatively high amplitude, high-frequency variance in color reflectance (Fig. F6). Subunit IB extends from 37 to 84.2 mbsf in Hole 1209A (upper Pliocene to upper Miocene) and consists of alternating nannofossil ooze with clay and nannofossil ooze. It is distinguished from Subunit IA primarily on the basis of carbonate content, color, and cycle amplitude. Subunit IC extends from 85.0 to 111.2 mbsf (middle to upper lower Miocene). It is characterized by more variable carbonate content (5–90 wt%; Table T10) and high red/blue ratios relative to Subunits IA and IB.

Subunit IA

The periodic lithologic variations of Subunit IA are expressed as decimeter-scale light–dark color cycles ranging in wavelength between 40 and 150 cm (Figs. F6, F7). The longer wavelength cycles are most pronounced in the upper 10-m, upper Pleistocene portion of the unit. The thinner (30–50 cm) dark beds are light olive gray (5Y 6/1) to olive gray (5Y 4/1) in color, whereas the thicker (~50–150 cm) light beds range from very light gray (N8) to light gray (N7). The contacts between the

interbeds tend to be gradational, although some contacts from light to dark are sharp. Millimeter-scale pyrite laminae and blebs are common throughout Subunit IA. Dark gray to pale green millimeter-scale bands and laminae are randomly distributed, although they appear to be more frequent in the light intervals and around some lithologic contacts. Disseminated volcanic glass and discrete centimeter-thick ash bands are frequent in this subunit. As many as three to four ash layers occur in some cores. Common sedimentary structures include burrows and indistinct mottling. Bioturbation is rare to moderate throughout Subunit IA, and with the exception of Core 198-1209A-1H, there is no indication of significant deformation by drilling. Several contacts present in Core 198-1209A-2H are inclined at high angles and thus appear to be erosional in nature. Section 198-1209A-2H-6 also contains a fault with a normal offset.

Subunit IB

Subunit IB extends from 37 to 84.2 mbsf in Hole 1209A and 37 to 86.06 mbsf in Hole 1209B (intervals 198-1209A-5H-1, 99 cm, through 10H-1, 0 cm, and 198-1209B-5H-3, 40 cm, through 10H-4, 46 cm) and consists primarily of very light gray (N8) nannofossil ooze and light gray (N7) nannofossil ooze with clay. The concentration of biosiliceous components reaches 20% at ~51 mbsf, the highest value recorded at this site (Fig. F8). The transition from Subunit IA is marked by an increase in the overall reflectance as well as a distinct decrease in the amplitude of the high-frequency color cycles and an increase in the amplitude of long (5–8 m) wavelength color cycles (Fig. F7). Note that similar transitions at other sites are not distinguished with a subunit boundary with the exception of Site 1212. Carbonate content increases slightly downhole in this unit to Core 198-1209A-10H (Fig. F6). Trace pyrite is present as blebs, in burrows, and in millimeter-scale faint black bands or laminae. Clusters of pale green laminae with traces of pyrite are present as well. Siliceous microfossils, primarily radiolarians, and volcanic glass are present in minor to trace quantities. Although this subunit is moderately bioturbated, distinct, identifiable ichnofossils are very rare.

F8. Estimates of biosiliceous material from smear slides, Hole 1209A, p. 44.

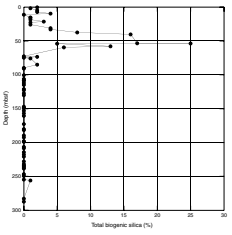

Subunit IC

Subunit IC extends from 84.2 to 111.2 mbsf in Hole 1209A, 86.06 to 110.6 mbsf in Hole 1209B, and 98 to 110.7 mbsf in Hole 1209C (Sections 198-1209A-10H-1, 0 cm, through 12H-6, 50 cm; 198-1209B-10H-4, 46 cm, through 13H-1, 130 cm; and 198-1209C-1H-1 through 2H-3, 23 cm). The lithology is predominantly clayey nannofossil ooze and nannofossil ooze with clay. Sediment hues vary from grayish orange (10YR 7/4), to pale yellowish brown (10YR 6/2) and dark yellowish brown (10YR 4/2), to very pale orange (10YR 8/2). The transition from the overlying subunit is marked by a very distinct rise in the red/blue ratios (Fig. F9). Note that this transition is analogous to the Subunit IA/IB boundary at the other sites (except for Site 1212). The unit also contains several clay layers, the most prominent of which is a 30-cm-thick dusky yellowish brown (10YR 2/2) clay in Section 198-1209A-12H-4. This clay represents a condensed interval that includes much of the upper lower Miocene. Well-developed ichnofossils, primarily *Zoophycos* burrows, are common at the contacts between the dark and light beds

F9. Composite digital photograph and color reflectance red/blue ratio, Core 198-1209A-10H, p. 45.

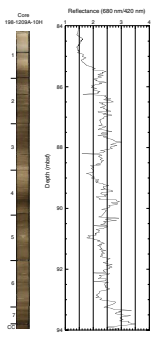

in this unit. Bioturbation is rare to moderate throughout the unit, and there is virtually no drilling disturbance.

Lithologic Unit II

Intervals: 198-1209A-12H-6, 50 cm, through 25H-6, 112 cm; 198-1209B-13H-1, 103 cm, through 25H-5, 134 cm; and 198-1209C-2H-3, 23 cm through 15H-3, 85 cm
Depths: 111.2 to 235.2 mbsf in Hole 1209A, 110.6 to 230.9 mbsf in Hole 1209B, and 110.7 to 234.85 mbsf in Hole 1209C
Age: early Oligocene to early Paleocene

Unit II at Site 1209 has been subdivided into two subunits. The contact with Unit I, which occurs in Section 198-1209A-12H-6, is marked by a major lower Miocene/upper Oligocene unconformity (Fig. F6). Moreover, the contact with Unit I is marked by an abrupt shift in the apparent stiffness of the sediment. In Unit I, the nannofossil ooze is firm and stiff, whereas in Unit II the ooze tends to be much softer with a pastelike consistency. The latter property, which contributed to some flow-in and stretching during coring, persists to the bottom of the hole.

Subunit IIA

Subunit IIA extends from 111.2 to 198.0 mbsf in Hole 1209A (lower Oligocene to Paleocene/Eocene [P/E] boundary). This unit contains primarily nannofossil ooze with occasional intervals of nannofossil ooze with clay. Color in the Oligocene and upper Eocene portion of the Subunit (112–130 mbsf in Hole 1209A) ranges from grayish orange (10YR 7/4) to very pale orange (10YR 8/2). The Eocene–Oligocene transition (127–128 mbsf in Hole 1209A) is marked by an upcore increase in carbonate content as inferred from reflectance (Fig. F10). The lithology of the lower and middle Eocene (157–217 mbsf in Hole 1209A) is relatively uniform with nannofossil ooze and nannofossil ooze with clay. With the exception of disseminated white burrows with dark halos, sedimentary structures are relatively rare in this subunit. Decimeter-scale (50–80 cm) lithologic cycles occur throughout the unit (Fig. F7). The cycle amplitudes as expressed in color reflectance are lower than in overlying units, suggesting reduced amplitude variations in carbonate/clay content. The exceptions are several distinct darker, more clay-rich intervals, which are easily distinguished in all holes as peaks in reflectance or magnetic susceptibility. One of these clay-rich intervals occurs at the base of Subunit IIA at 198.0 mbsf (Sections 198-1209A-21H-7, 25 cm; 198-1209B-22H-1, 132 cm; and 198-1209C-11H-3, 130 cm; Figs. F11, F12). Biostratigraphy indicates that this horizon lies approximately at the Paleocene/Eocene boundary and is thus coincident with the PETM. In the sediment just a few centimeters below the clay-rich layer, we find moderate amounts of inorganic calcite needles (Fig. F13). Note that the Paleocene/Eocene boundary is not distinguished by a subunit boundary at the other sites with the exception of Site 1212.

Subunit IIB

Subunit IIB extends from 198.0 mbsf to the K/T boundary at 235.2 mbsf in Hole 1209A. It primarily comprises very pale orange (10YR 8/2) nannofossil ooze and pale yellowish brown (10YR 6/2) nannofossil ooze with clay. These two major lithologies tend to alternate on a meter

F10. Composite digital photograph and color reflectance, Core 198-1209A-14H, p. 46.

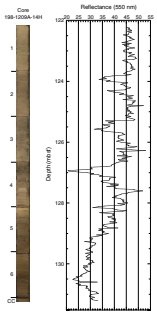

F11. Composite digital photograph, color reflectance, and bulk density, Core 198-1209A-21H, p. 47.

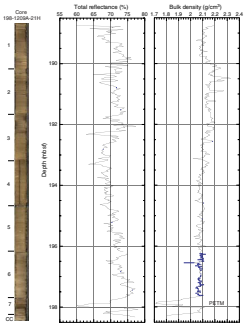

F12. Contact between clay-poor and clay-rich sediment at the base of the Paleocene, p. 48.

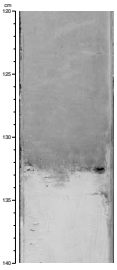

F13. Needles of inorganic calcite dispersed within nannofossil ooze, p. 49.

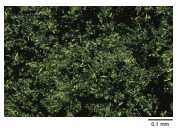

scale with very gradational contacts. There are also several centimeter-scale horizons characterized by darker more clay-rich lithologies with more abrupt contacts. The most prominent of these occurs in Section 198-1209A-23H-5. Disseminated white burrows and blebs occur throughout the unit. Minor amounts of pyrite are also present, primarily as foraminiferal infill. The base of Unit II, the K/T boundary, is marked by a thin nondistinct horizon. The sediments both above and below this horizon are white (N9) to very pale orange (10YR 8/2) nannofossil ooze. Above the boundary, this light foraminiferal nannofossil ooze gradually grades into a darker, grayish orange (10YR 7/4) nannofossil ooze. A similar trend in total reflectance indicates that this gradation represents an uphole transition into sediment with lower carbonate content (Fig. **F14**).

F14. Composite digital photograph, color reflectance, and bulk density, Core 198-1209A-25H, p. 50.

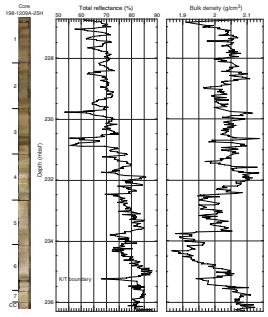

Lithologic Unit III

Intervals: Sections 198-1209A-25H-6, 112 cm, through 28X-5; Section 198-1209B-26H-5, 134 cm, through Core 198-1209B-32H; and Section 198-1209C-15H-3, 85 cm, through Core 23X
Depths: 235.2 mbsf to 297.0 in Hole 1209A, 230.9 to 297.4 mbsf in Hole 1209B, and 234.85 to 297 mbsf in Hole 1209C
Age: Maastrichtian

Lithologic Unit III consists predominantly of a uniform white (N9) to very pale orange (10YR 8/2) nannofossil ooze with carbonate content in excess of 96 wt%. The top of Unit III is defined by the K/T boundary transition. The base of the unit is marked by a chert layer of unknown thickness that prevented further coring. All sediments are moderately bioturbated, and mild coring disturbance is common. A thin (3 cm) bed of Inoceramid shell fragments is present in Section 198-1209B-31H-1 and large fragments of *Inoceramus* extend from Section 198-1209C-21H-1, 125 cm, to Section 21H-3, 128 cm. Three chert layers were encountered in Hole 1209C. The absence of these layers in Hole 1209B, however, suggests that the layers are discontinuous or nodular or were not recovered.

Interpretation

Sedimentation

Unit I

Cyclic variations in the position of the lysocline and CCD have exerted a strong influence on the composition of sediment in the Pacific through the Cenozoic. At present, Site 1209 is situated well above the lysocline and CCD, which are at 3.5 and 4.1 km, respectively, in the region. As such, the uppermost Holocene sediments at Site 1209 have a relatively higher carbonate content than the Holocene of Sites 1207 (3.5 km) and 1208 (3.3 km). Because the CCD generally deepens in the Pacific during glacials (Farrell and Prell, 1989), its role in driving the Pleistocene lithologic cycles recorded in Unit I is probably minor. Instead, productivity and sediment transport may be more important. As with the deeper-water Sites 1207 and 1208, the darker-colored intervals generally contain higher amounts of biosiliceous material and clay and probably represent intervals of higher surface water productivity and increased in situ carbonate dissolution. The frequency of cycles in color reflectance through the Pleistocene suggest that they are

related to glacial/interglacial cycles. The cycle amplitudes are smaller than the deeper site, owing to a lower contribution of clay and siliceous microfossils to the sediment. Moreover, despite the shallower water depth, the sedimentation rate is significantly lower at Site 1209, ~13–14 m/m.y. over the Pleistocene compared to 42.4 m/m.y. at Site 1208 (Fig. F23). This indicates that carbonate production and preservation may have played a more important role in driving the Pleistocene lithologic cycles. As at the other sites, the dominant period of the cycles corresponds to eccentricity (100 k.y.) subsequent to 0.6 Ma, and obliquity (41 k.y.) for the period from 0.6 to 2.5 Ma. The cycle wavelength at Site 1209, however, is much more irregular, suggesting that accumulation rates were highly variable through time.

Below 37 m (Subunit IB) in Hole 1209A, which roughly corresponds to the onset of Northern Hemisphere glaciation at 2.6 Ma, the high-frequency (~41 k.y.) cycle amplitude decreases. The decrease results primarily from the absence of the low-carbonate "glacial" end-member of the cycles, despite a relative increase in silica content in the mid-Pliocene. Moreover, there is an apparent shift in power to a lower-frequency, longer-wavelength (9–13 m) oscillation. Assuming an average sedimentation rate of 13.4 m/m.y., these cycles would have periods close to those of the long obliquity (1.25 m.y.) cycles. The peak in siliceous microfossil deposition at Site 1209 occurred in the mid-Pliocene, at roughly the same time as in regions of the North Pacific (Rea et al., 1995).

The sediment of Subunit IC shows evidence of greater oxidation as reflected by the predominance of shades of pale orange and gray orange. This is also reflected in the red/blue reflectance values, which are three times those of Subunit IB, and magnetic susceptibility (Fig. F7), which is also higher owing to the greater Fe oxide content (see "Physical Properties," p. 29). The decrease in carbonate content within Subunit IC is accompanied by the presence of several more clay-rich intervals, most notably in Section 198-1209A-12H-3. This pattern is similar to those observed at the deeper Sites 1207 and 1208. The biostratigraphy demonstrates that these clay horizons are condensed intervals, most likely produced by dissolution of carbonate at the seafloor during the middle and late early Miocene. Such a phenomenon would be consistent with the reported shoaling of the global lysocline and CCD through the early and middle Miocene (Rea and Leinen, 1986). Studies of previously drilled sites suggest that the lysocline was as shallow as 3 km during the early Miocene. The data collected here indicate that the lysocline might have been even shallower (<2.4 km) during much of this period.

Unit II

On average, Unit II sediment shows evidence of greater oxidation than Unit I. This is illustrated by the red/blue reflectance ratios, which are three times more than the average for Unit I. Carbonate content on average is also much higher than that in Unit I (Core 198-1209A-15H; Fig. F6). As observed at the deeper sites on Shatsky Rise, a low rate of sedimentation (<6 m/m.y.) in the Paleogene indicates that the oxidized character is partially a product of lower surface water productivity. Another potential contributing factor is global deep-sea circulation, which for most of the period prior to the late Miocene lacked deepwater formation in the North Atlantic (Wright et al., 1992). The net result was that Pacific deep waters were relatively less nutrient rich and corrosive, and more oxygenated, than prior to the Miocene. An increase in car-

bonate accumulation in the early Oligocene is consistent with a global deepening of the CCD coincident with the Eocene/Oligocene boundary. At Site 1208, the deepening trend appears to have been nonlinear, or punctuated by periodic reversals or oscillations (Fig. **F9**). The cycle wavelengths (~1.6 m) and sedimentation rate (~3.9 m/m.y.) suggest concentration of power at a frequency close to that of the long eccentricity (400 k.y.) cycle. These may be related to fluctuations in the global carbon cycle, as similar cycle frequencies have also been recognized in late Eocene and early Oligocene deep-sea carbon isotope time series (Diester-Haass and Zahn, 1996; Zachos et al., 1996).

The style of early to middle Eocene sediment accumulation in the lower portion of Subunit IIA indicates deposition under oxic conditions and low productivity. The subtle color cycles also hint at some influence of orbital oscillations on regional sedimentation. For example, in the middle Eocene, the dominant cycles have 50- to 60-cm wavelengths and sedimentation rates average 0.52 cm/k.y., thus indicating a primary response to 100-k.y. eccentricity forcing (Fig. **F15**). The most prominent feature of this subunit, however, is the clay-rich layer at the P/E boundary. This layer most likely represents an episode of enhanced dissolution related to a hypothesized rapid shoaling of the global CCD (Dickens et al., 1995, 1997). The CCD rise is attributed to the effects of dissolving ~2000 Gt of carbon (as CO_2) on the pH and carbonate ion content of deep waters. The Site 1209 P/E boundary horizon is characterized by a sharp basal contact rich in clay, which then grades upward into more carbonate-rich sediment (Fig. **F12**). This carbonate dissolution and recovery pattern is similar to that observed in Atlantic pelagic and hemipelagic sequences (Kennett and Stott, 1991; Bralower et al., 1997; Thomas et al., 1999). Because this represents the first documentation of this pattern in the Pacific, it lends substantial support to the methane outflux model, which calls for shoaling of the CCD in all ocean basins.

The base of Unit II is marked by the K/T boundary. Because this appears to be one of the more complete K/T boundary sequences for the Pacific (see **"Biostratigraphy,"** p. 16), the primary lithologic changes observed across this interval should reflect on the regional ecological and water column chemical variations associated with this biotic crisis. For example, the thin, basal clay most likely formed in the immediate aftermath of the impact, a period of widespread extinction of nanno- and zooplankton, and collapse in global primary and net production (Thierstein, 1981; Zachos and Arthur, 1986; Zachos et al., 1989).

Unit III

The Maastrichtian is known for the widespread deposition of calcareous nannofossil-rich sediments. The Maastrichtian at Site 1209 is no exception. It is characterized by the accumulation of exceptionally pure calcareous nannofossil ooze. The primary difference is that the Site 1209 Maastrichtian sediments are poised at the ooze–chalk transition, whereas elsewhere the vast majority are chalks or limestones. The high carbonate content and pale orange color indicate oxidizing conditions and low rates of eolian and other dilution in the central Pacific. The presence of *Inoceramus* in the mid-Maastrichtian may be an important finding, as Inoceramid debris are generally restricted to sediments older than mid-Maastrichtian elsewhere (MacLeod et al., 1996). More detailed examination of the Site 1209 cores should provide insight as to the nature of the environmental conditions in the Pacific at the time of this extinction event.

F15. Total reflectance and magnetic susceptibility for a middle Eocene interval, p. 51.

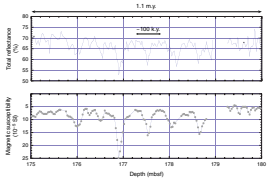

BIOSTRATIGRAPHY

The Neogene section of nannofossil ooze, chalk, and clay in Holes 1209A and 1209B ranges from the Pleistocene to the lower Miocene. Hole 1209C was cored down from the middle Miocene. Two unconformities or condensed intervals are present within the upper Miocene (Samples 198-1209A-9H-CC to 10H-CC and 198-1209B-10H-CC to 11H-CC) and between the upper and lower Miocene (Samples 198-1209B-11H-CC to 12H-CC and 198-1209C-1H-CC to 2H-CC) as revealed by calcareous plankton bioevents. A second major unconformity separates the lower Miocene from the Oligocene (Samples 198-1209B-12H-CC to 13H-CC and 198-1209C-2H-CC to 3H-CC). The Eocene and the Paleocene sections were triple-cored and appear to be complete, including the P/E boundary transition, the PETM critical interval, and the K/T boundary, at least to within the calcareous plankton biostratigraphic resolution achieved shipboard. A thick and continuous middle–upper Maastrichtian sequence of white nannofossil ooze was also triple-cored at Site 1209. The main calcareous nannofossil and foraminiferal datums are summarized in Tables T2 and T3.

Calcareous nannofossils are generally abundant and moderately to well preserved throughout the Cenozoic and Mesozoic sediments of Holes 1209A, 1209B, and 1209C. Neogene planktonic foraminifers are moderately to well preserved, but foraminiferal abundance is relatively low, due to selective dissolution and fragmentation. Dissolution and generally poor preservation characterizes the Oligocene and upper and middle Eocene assemblages, whereas the preservation improves slightly in the remainder of the Eocene and Paleocene section. Cretaceous planktonic foraminifers are well preserved and abundant. All core catcher samples were examined and supplementary samples used to refine datums and the stratigraphy in and around critical intervals.

Studies on benthic foraminifers were conducted on selected core catcher samples from Holes 1209A and 1209C. The >250-µm size fraction was examined for the Neogene samples, and the >125-µm size fraction was examined for the Paleogene and Cretaceous samples. Neogene benthic foraminifers are well preserved and common; Paleogene and Cretaceous taxa are moderately well preserved but rare.

T2. Calcareous nannofossil datums, ages, and depths, p. 83.

T3. Planktonic foraminifer datums, ages, and depths, p. 84.

Calcareous Nannofossils

Neogene

The Pleistocene and Neogene section ranges from the upper Pleistocene (Subzone CN14b) to the lower–middle Miocene (Zones CN1 to CN3). Calcareous nannofossils are generally abundant and moderately to well preserved throughout, and most of the zones of Okada and Bukry (1980) were recognized. Zones CN8, CN6, and CN5 were not identified, most likely due to condensed intervals and/or short unconformities; calculations reveal a marked decrease in sedimentation rate around 7 Ma in Zone CN9.

The middle to lower Miocene (Zones CN3 to CN2) is difficult to subdivide, due to the sporadic occurrence of the nominal taxon *Sphenolithus heteromorphus,* as reported from previous Leg 198 sites. At Site 1209, *S. heteromorphus* was recorded from Samples 198-1209B-12H-CC and 198-1209C-2H-CC. A lower Miocene interval (Zones CN1 to CN3) was identified based on the presence of abundant *Discoaster deflandrei* (acme top within Zone CN3) and *Cyclicargolithus floridanus,* the absence

of *S. heteromorphus* and *Calcidiscus premacintyrei,* and the absence of older, robust taxa such as *Cyclicargolithus abisectus, Reticulofenestra bisectus,* and *Zygrhablithus bijugatus,* which have LOs in Subzone CN1a and lower Subzone CN1b.

Paleogene

An unconformity and/or condensed interval separates the lower Miocene (Zone CN1 to CN3) and lower Oligocene (Subzone CP19a), but the lower Oligocene and Oligocene–Eocene transition appears to be complete.

The Eocene and Paleocene section also appears to be complete, including the Paleocene/Eocene boundary transition and the PETM critical interval. Events constraining this interval include the abundance decline and last occurrence of the genus *Fasciculithus* (e.g., interval 198-1209B-22H-1, 12–134 cm), the FO of *Discoaster diastypus* (e.g., Sample 198-1209B-21H-6, 120 cm; base of Subzone CP9a), and the FO of *Tribrachiatus orthostylus* (e.g., Sample 198-1209B-21H-4, 100 cm; base of Subzone CP9b). Other biostratigraphically significant species of the *Tribrachiatus* lineage are also present but are not well preserved.

The K/T boundary also appears to be complete and includes a relatively expanded series of datum events following the LO of Cretaceous taxa (see Fig. **F3**). The boundary is overlain by a 16-cm carbonate layer dominated by fine micrite and abundant calcispheres and tiny foraminifers, with rare to few reworked Cretaceous nannofossil taxa and frequent survivor taxa (e.g., *Cyclagelosphaera* and *Markalius inversus*) (e.g., Samples 198-1209A-25H-6, 90 and 94 cm) (see Fig. **F3**). This is followed by influxes of *Neobiscutum* (Sample 198-1209A-25H-6, 40 cm) and, subsequently, *Cruciplacolithus* (Sample 198-1209A-25H-6, 10 cm).

Cretaceous

An apparently continuous section of Maastrichtian sediments was recovered from Site 1209. The calcareous nannofossils from this interval are well preserved and the assemblages diverse. Zones CC26 to CC24 were identified; however, the nominal taxon *Lithraphidites quadratus* was rare and sporadically distributed, and *Tranolithus orionatus* was very rare. We had difficulty identifying the LO of *Reinhardtites levis*. Therefore, there is a degree of uncertainty in our datum depths, and this is borne out by the position of these datums with respect to the best-fit sedimentation rate curve (see Fig. **F22**).

Planktonic Foraminifers

Neogene

The Neogene section ranges from upper Pleistocene to middle Miocene, with two possible unconformities separating parts of the upper and middle Miocene; another unconformity separates the middle Miocene and lower Oligocene. Planktonic foraminifers at Site 1209 are generally moderately preserved. They are abundant to common in the Pleistocene and Pliocene but then decline in abundance and preservation downward through the Miocene.

The youngest sediments recovered in Holes 1209A and 1209B are assigned to Pleistocene Zone N22 based on the co-occurrence of *Truncorotalia tosaensis* and *Truncorotalia truncatulinoides* in Samples 198-1209A-

1H-CC and 2H-CC and 198-1209B-1H-CC to 3H-CC. Common Pleistocene taxa include *Globigerina bulloides, Globorotalia inflata, Globorotalia crassaformis, Orbulina universa, Neogloboquadrina dutertrei,* and *Neogloboquadrina pachyderma* (dextral). These are supplemented by few *Globorotalia menardii, Globorotaliatumida,* and pulleniatinids. Within the Pliocene sediments the FOs of *T. tosaensis, T. crassaformis* (Samples 198-1209A-6H-CC and 198-1209B-5H-CC), and *Sphaeroidinella dehiscens* (Samples 198-1209A-7H-CC and 198-1209B-8H-CC) allow the differentiation of Zones N21 and N20–N19, respectively. Other useful bioevents are the LOs of *Dentoglobigerina altispira* (Samples 198-1209A-6H-CC and 198-1209B-8H-CC), *Sphaeroidinellopsis seminulina* (Samples 198-1209A-5H-CC and 198-1209B-5H-CC), and *Globoturborotalita nepenthes* (Samples 198-1209A-7H-CC and 198-1209B-8H-CC).

The Miocene sequence at Site 1209 is interrupted by unconformities, and planktonic foraminiferal preservation is slightly improved compared with Sites 1207 and 1208. The uppermost Miocene is present in Sample 198-1209B-8H-CC, which contains common *Globorotalia tumida, Globorotalia conoidea, Globorotalia miozea, Globoturborotalita nepenthes,* and *Sphaeroidinellopsis seminulina.* This sample is assigned to Zone N18 based on the presence of *G. tumida* and the absence of *Sphaeroidinella dehiscens*. The presence of common late Miocene taxa such as *Globorotalia plesiotumida, Dentoglobigerina altispira, Globoquadrina venezuelana, G. nepenthes,* and *G. conoidea* (from Samples 198-1209A-9H-CC to 10H-CC and 198-1209B-9H-CC) permit the identification of Zone N17 based on the absence of *G. tumida*. A minor unconformity separates this interval from the remainder of the upper Miocene sequence drilled in Holes 1209A (Samples 198-1209A-10H-CC and 11H-CC) and 1209B (Sample 198-1209B-11H-CC), which yield few to common *Globoquadrina dehiscens, G. nepenthes, Globoturborotalita woodi, Globoturborotalita decoraperta,* and *Dentoglobigerina altispira.* In the absence of *Neogloboquadrina acostaensis* and based on the presence of *G. nepenthes,* the assemblages are attributed to Zones N14 to N15. This interval overlies middle Miocene sediments recovered in Samples 198-1209B-12H-CC and 198-1209C-1H-CC, which contain *Fohsella peripheroronda, G. dehiscens, Sphaeroidinellopsis disjuncta, Globigerinoides mitra,* and *Praeorbulina glomerosa* and indicate Zones N8 and N9.

Paleogene

An unconformity separates the Miocene and Oligocene at Site 1209. The paucity of planktonic foraminiferal marker species renders age determination problematic for much of the Oligocene examined at this site. Dissolution is a likely factor for the absence of many taxa based on the abundance of foraminiferal fragments and crystals of phillipsite in Oligocene age samples. For example, Sample 198-1209B-13H-CC contains the robust taxa *Catapsydrax dissimilis, Catapsydrax unicavus, "Globigerina" euapertura,* and *"Globoquadrina" pseudovenezuelana,* but no zonal marker species are present. A similar assemblage is present in Sample 198-1209C-2H-CC; however, the presence of *Subbotina angiporoides* without *Pseudohastigerina* spp. indicates Zones P19 and P20. The presence of numerous specimens of *Globoquadrina dehiscens* in this sample suggests that downhole contamination is a problem. Lower Oligocene Zone P18 is identified in Sample 198-1209A-13H-CC based on the presence of *Pseudohastigerina* spp. together with *Cassigerinella chipolensis, "Globigerina" ampliapertura, Tenuitella gemma, Tenuitellinata an-*

gustiumbilicata, Catapsydrax spp., *"Globoquadrina" pseudovenezuelana,* and *Subbotina gortanii*.

Dissolution and generally poor preservation continues down into the upper Eocene. Sample 198-1209A-14H-CC is assigned to Zones P16 to P17 based on the presence of *"Globigerina" ampliapertura,* spines of *Hantkenina,* and poorly preserved specimens of *Hantkenina alabamensis*. The sample is dominated by dissolution-resistant taxa, including *Globigerinatheka senni, Catapsydrax unicavus,* and *"Globigerina" euapertura*. A similar assemblage, including *H. alabamensis,* is present in Sample 198-1209B-14H-CC. Sample 198-1209C-4H-CC contains a nearly monogeneric assemblage of *Globigerinatheka* spp.

Preservation improves somewhat in the upper part of the middle Eocene. Sample 198-1209B-15H-CC contains an assemblage indicative of Zones P12 to P15 that includes *Globigerinatheka index, Globigerinatheka mexicana, G. senni, Turborotalia pomeroli, C. unicavus,* and spines of *Hantkenina*. Zone P13 is based on the total range of *"Orbulinoides" beckmanni;* rare specimens of this taxon are present in Sample 198-1209A-15H-CC together with *G. index, G. mexicana, G. senni, Acarinina bullbrooki,* and *Acarinina primitiva*. Middle Eocene Zone P11 is present in Samples 198-1209A-16H-CC, 198-1209B-16H-CC, and 198-1209C-6H-CC. This zone is characterized by the presence of *Morozovella aragonensis, A. bullbrooki, Igorina broedermanni, Globigerinatheka index, Globigerinatheka subconglobata, Hantkenina mexicana,* and *Guembelitrioides higginsi*. The co-occurrence of *Hantkenina* (observed only as isolated spines) together with *Morozovella caucasica* and *Acarinina pentacamerata* serves to distinguish Zone P11 from P10. The FO of *Hantkenina* defines the Zone P9/P10 boundary.

Lower Eocene Zones P8 and P9 are not differentiated because of the absence of *Planorotalites palmerae*. Samples 198-1209A-18H-CC and 19H-CC, 198-1209B-17H-CC and 18H-CC, and 198-1209C-7H-CC and 8H-CC are assigned to Zones P8 to P9. These samples are characterized by *Morozovella aragonensis, M. caucasica, Acarinina pentacamerata, Acarinina soldadoensis, Igorina broedermanni,* and *Acarinina quetra,* as well as *Globigerinatheka subconglobata micra* in the upper part and *M. subbotinae* in the lower part of this interval. Zone P7 is distinguished from the overlying sediments by the co-occurrence of *M. aragonensis* and *Morozovella formosa* and by the absence of *A. pentacamerata* in Samples 198-1209A-20H-CC, 198-1209B-20H-CC, and 198-1209C-9H-CC. The boundary between Zones P6 and P7 is present between Samples 198-1209A-21H-3, 68–69 cm, and 21H-4, 129–130 cm. Characteristic taxa of Zone P6 include *M. subbotinae, M. aequa* (in Subzone P6a), *M. formosa, M. gracilis, Subbotina velascoensis,* and *A. soldadoensis* in the absence of both *M. aragonensis* and *M. velascoensis*.

The extinction level of *Morozovella velascoensis* is used to define the P6/P5 zonal boundary, as well as the Paleocene/Eocene epoch boundary, and this datum occurs between Samples 198-1209A-21H-5, 49–50 cm, and 21H-5, 129–130 cm. The PETM (Zachos et al., 1993) and benthic foraminiferal extinction (BFE) event (Thomas and Shackleton, 1996) occur within Zone P5, and the interval is identified in Section 198-1209A-21H-6 based, in part, on the presence of the benthic foraminifer *Gavelinella beccariiformis* in Sample 198-1209A-21H-CC, a taxon that goes extinct at the BFE. Zone P5 contains a rich assemblage of *M. velascoensis, Morozovella occlusa, M. subbotinae, M. aequa, Morozovella pasionensis,* and *Acarinina soldadoensis*. The total range of *Globanomalina pseudomenardii* defines upper Paleocene Zone P4, which co-occurs with a diverse assemblage, including *M. aequa* (in the upper part), *M. velas-*

coensis, M. occlusa, M. pasionensis, Igorina pusilla, Igorina albeari, Igorina tadjikistanensis, Acarinina mckannai, Acarinina nitida, and *Acarinina subsphaerica* (in the lower part). Samples 198-1209A-22H-CC and 23H-CC, 198-1209B-22H-CC, and 198-1209C-11H-CC are assigned to Zone P4. *Morozovella angulata, M. conicotruncata, Subbotina triloculinoides,* and *Parasubbotina pseudobulloides* mark Zone P3 in Sample 198-1209C-13H-CC.

Lower Paleocene Zone P2 (Samples 198-1209A-24H-CC, 198-1209B-24H-CC, and 198-1209C-14H-CC) contains *Praemurica uncinata, Praemurica inconstans, Morozovella praeangulata,* and *Parasubbotina pseudobulloides*. The interval containing Zone P1 and its subzones is thin at Site 1209 and was not observed in core catcher samples. However, several samples taken across the K/T boundary permit the recognition of the *Parvularugoglobigerina eugubina* Zone (Zone Pα) in the interval between Samples 198-1209A-25H-6, 93–94 cm, and 113–114 cm, and between Samples 198-1209C-15H-3, 67–68 cm, and 85–86 cm (see Fig. **F3**). The assemblage includes the species *P. eugubina, Parvularugoglobigerina extensa,* woodringinids, and *Parasubbotina pseudoinconstans*.

Cretaceous

Cretaceous planktonic foraminifers recovered at Site 1209 are generally abundant and well preserved. The highest Cretaceous assemblages are present in Samples 198-1209A-25H-6, 113–114 cm, 198-1209B-26H-CC, and 198-1209C-15H-3, with few Paleocene taxa indicative of the P0 and Pα Zones in the burrows (see Fig. **F3**). The large-sized Cretaceous taxa include *Abathomphalus mayaroensis, Pseudoguembelina costulata, P. excolata,* and *P. hariaensis,* as well as the small taxa *Schackoina cenomana, Globigerinelloides subcarinatus, Globotruncanella havanensis,* and *Globotruncanella petaloidea,* indicating the upper Maastrichtian *A. mayaroensis* Zone (KS31).

The underlying Upper Cretaceous interval (Samples 198-1209A-25H-6, 123–124 cm, to 28H- CC, 198-1209B-27H-CC to 28H-CC, and 198-1209C-16H-CC to 18H-CC) is characterized by a moderately to well-preserved planktonic foraminiferal assemblage yielding *Abathomphalus mayaroensis, Abathomphalus intermedius, Contusotruncana contusa, Racemiguembelina fructicosa, Pseudotextularia elegans,* common pseudoguembelinids, *Globotruncanita stuarti, Globotruncanita stuartiformis, Globotruncana orientalis, Heterohelix rajagopalani,* and rugoglobigerinids. Based on the presence of *A. mayaroensis* this interval is still assigned to the upper Maastrichtian *A. mayaroensis* Zone (KS31).

The older Cretaceous sequence has been recovered only in Holes 1209B and 1209C. Samples 198-1209B-29H-CC to 30H-CC and from 198-1209C-19H-CC to 20H-CC yield common *Contusotruncana contusa* and *Racemiguembelina fructicosa* in the absence of *A. mayaroensis,* indicating that this interval belongs to the lower Maastrichtian *C. contusa–R. fructicosa* Zone (upper KS30). Other species present in this interval are *Contusotruncana patelliformis, Globotruncana bulloides, Globotruncana linneiana, G. stuarti, G. stuartiformis, Rugotruncana subcircumnodifer* associated with rare *Gansserina gansseri* and *Gansserina wiedenmayeri,* and common pseudoguembelinids and rugoglobigerinids. The lowest parts of Holes 1209B (Samples 198-1209B-31H-CC to 32H-CC) and 1209C (Samples 198-1209C-21H-CC to 22H-CC) are assigned to the lower Maastrichtian–upper Campanian *G. gansseri* Zone (KS30), based on the absence of *C. contusa* and *R. fructicosa* and the presence of few *G. gansseri*.

Benthic Foraminifers

Benthic foraminifers were examined in selected core catcher samples from Holes 1209A and 1209C. In these holes, Neogene sediments contain generally well-preserved and rare to few benthic foraminifers. In Samples 198-1209A-25H-CC and 198-1209C-3H-CC and 25H-CC, planktonic foraminifers are strongly dissolved, and consequently, the relative abundance of benthic foraminifers is higher. The test size of benthic foraminifers is generally small in the Paleogene- and Cretaceous-age sediments, so the >125-µm size fraction was examined in these intervals. Distributions of the Cenozoic and Cretaceous benthic foraminifers are plotted in Tables **T4** and **T5.**

T4. Cenozoic and Cretaceous benthic foraminifers, Hole 1209A, p. 85.

T5. Cenozoic and Cretaceous benthic foraminifers, Hole 1209C, p. 87.

Neogene

Samples 198-1209A-1H-CC to 2H-CC yield *Oridorsalis umbonatus, Pullenia bulloides,* uvigerinids, and *Pyrgo murrhina*. In Samples from 198-1209A-5H-CC to 9H-CC, *Oridorsalis tener, Pullenia bulloides, Stilostomella subspinosa,* uvigerinids, gyroidinoidids, and cibicidoidids characterize the benthic assemblage, except for Sample 198-1209A-7H-CC, in which uvigerinids are absent. The stilostomellids become more frequent in Sample 198-1209A-11H-CC.

Sample 198-1209C-1H-CC, which is Miocene in age, contains common calcareous trochospiral forms such as *Anomalinoides semicribratus, Gyroidinoides girardanus, Oridorsalis tener,* and *Pullenia bulloides* and the agglutinated taxa *Martinottiella* sp. and *Eggerella bradyi*. Uvigerinids and *Pyrgo murrhina* are present as a minor component of the assemblage in this sample.

Paleogene

Bulimina trinitatensis, Oridorsalis umbonatus, nodosariids, stilostomellids, *Vulvulina mexicana,* and *V. spinosa* are the main components in Sample 198-1209A-12H-CC and 13H-CC. Uvigerinids that characterized the Neogene section are absent.

The preservation of benthic foraminifers is poor to moderate in the lower Oligocene to lower Eocene (Samples 198-1209A-14H-CC to 20H-CC), and their test size is generally small. Buliminids (*Bulimina impendens, Bulimina jarvisi, Bulimina semicostata, B. trinitatensis,* and *Quadratobuliminella pyramidata*) are the characteristic group in this interval. Stilostomellids are also present, but they decline in abundance. The 250-µm size fraction of Sample 198-1209A-21H-CC, which is late Paleocene in age, is characterized by the dominance of agglutinated forms such as *Tritaxia* spp., *Pseudoclavulina rugolosa,* and *Spiroplectammina jarvisi,* whereas *Gavelinella beccariiformis* and *Conorbinoides hillebrandti* are common in the 125- to 250-µm size fraction.

Samples 198-1209A-23H-CC and 24H-CC are dominated by *Nuttallides truempyi, Oridorsalis umbonatus, Aragonia velascoensis,* and buliminids (*Bulimina trinitatensis, Bulimina velascoensis,* and *Buliminella grata*). *Marssonella trochoides* commonly occurs in Sample 198-1209A-24H-CC. In Samples 198-1209C-3H-CC and 5H-CC, buliminids (*Bulimina impendens, B. jarvisi*, and *B. semicostata*) and the stilostomellids (*Stilostomella* spp., *Stilostomella abyssorum, Stilostomella gracillima,* and *S. subspinosa*) characterize the benthic assemblage. The virtual absence of the calcareous trochospiral morphotypes in Sample 198-1209C-5H-CC is notable. In Samples 198-1209C-7H-CC through 10H-CC, trochospiral

forms (*N. truempyi, O. umbonatus,* and *O. tener*), buliminids such as *Bulimina glomarchallengeri, B. jarvisi,* and *B. semicostata* and species of *Stilostomella* represent the main components of the benthic assemblage. *Chrysalogonium breviloculum* is common in Sample 198-1209C-9H-CC. *Oridorsalis umbonatus* and *N. truempyi* are the main components in the interval from Sample 198-1209C-11H-CC to 13H-CC. Agglutinated taxa (*M. trochoides, Spiroplectammina jarvisi,* and *Pseudoclavulina rugolosa*) rarely occur in this interval.

Cretaceous

Maastrichtian Samples 198-1209A-25H-CC and 27H-CC contain common *Nuttallides truempyi* and *Oridorsalis umbonatus* as well as *Aragonia velascoensis, Lenticulina* spp., and *Nodosaria* spp. *Pseudoclavulina rugolosa* is common in the >250-µm size fraction of Sample 198-1209A-25H-CC.

In Samples 198-1209C-15H-CC to 25H-CC (Maastrichtian), the benthic assemblage is generally characterized by *N. truempyi, O. umbonatus,* and a variety of agglutinated species (*Gaudryina pyramidata, Gaudryina* spp., *Marssonella trochoides, Pseudoclavulina rugolosa, Spiroplectammina jarvisi,* and *Tritaxia* spp.), *Lenticulina* spp., and *Dentalina* spp. Other benthic foraminifers sporadically present in this interval are *Conorbinoides hillebrandti, Gyroidinoides* spp., *Cibicidoides velascoensis, Quadrimorphina allomorphinoides, Sliterella lobulata, Gavelinella beccariiformis,* and *Aragonia velascoensis.*

Paleowater Depth

Paleodepth estimates are based on the work of Pflum et al. (1976), Tjalsma and Lohmann (1983), Woodruff (1985), and van Morkhoven et al. (1986) for the Cenozoic section. For the Cretaceous section, estimates are mainly based on the study of Nyong and Olsson (1984) and the backtracked paleodepth curve from Deep Sea Drilling Program (DSDP) and Ocean Drilling Program (ODP) data (Kaiho, 1999).

The miliolids *Pyrgo murrhina* and *Pyrgo lucernula,* and the uvigerinids *Uvigerina hispida* and *Uvigerina peregina* indicate upper abyssal (2000–3000 m) depth during the Neogene (Pflum et al., 1976; Woodruff, 1985). These taxa are associated with calcareous trochospiral species (*Oridorsalis tener, Pullenia bulloides, Cibicidoides subhaidingeri, Cibicidoides wuellerstorfi,* and *Gyroidinoides girardanus*) that exhibit a wider bathymetric range from the upper bathyal to abyssal zone (Pflum et al., 1976). In the Paleogene, benthic assemblages are generally represented by *Nuttallides truempyi, Oridorsalis umbonatus, Aragonia velascoensis,* and buliminids (Tjalsma and Lohmann, 1983) that also indicate deep water. The genus *Aragonia* typically characterizes Late Cretaceous benthic assemblages. *A. velascoensis* and *Aragonia ouezzanensis* indicate lower bathyal and abyssal paleodepths, respectively (Nyong and Olsson, 1984). In addition, *Pyramidina szajnochae,* a characteristic Late Cretaceous form from Section 198-1209C-22H-CC, suggests an uppermost abyssal depth (2000–2500 m) (Nyong and Olsson, 1984). Therefore, the paleodepth during the Maastrichtian is similar to that of the Paleogene. These estimates are consistent with backtracked paleodepths of Kaiho (1999).

PALEOMAGNETISM

All archive halves of core sections from Holes 1209A, 1209B, and 1209C that did not show a large degree of drilling-related deformation were measured on the shipboard pass-through magnetometer. In all, 546 core sections were measured from 83 cores recovered in the three holes. All but two are APC cores. As at Site 1208, many of the measured cores from the Oligocene–Paleocene and Cretaceous part of the section are in poor condition due to disturbance related to drilling, core recovery, and core splitting.

The natural remanent magnetization (NRM) of core sections was measured at 5-cm intervals, followed by measurement after two alternating-field (AF) demagnetization steps (10- and 20-mT peak fields). When time was available, additional AF demagnetization steps (usually at peak fields of 15 mT) were measured. NRM intensity values typically ranged over three orders of magnitude, from 10^{-4} to 10^{-1} A/m. As for samples from other Leg 198 sites, cores from Site 1209 have acquired a steep downward-directed magnetic overprint that masks the primary magnetization. This magnetic overprint appears to be largely removed by AF demagnetization at peak fields of 20 mT. A plot of magnetization intensity after 20-mT demagnetization shows an initial decline of two orders of magnitude in the upper 30 m of the sedimentary section. This decline is followed at greater depths by a recovery in magnetization intensities to ~10^{-3} A/m (Fig. **F16**).

Paleomagnetic data acquired from the shipboard pass-through magnetometer from Site 1209 were uninterpretable for the pre-Pliocene section. In the upper ~60 meters composite depth (mcd), however, it was generally possible to recognize Pliocene–Pleistocene polarity chrons (Fig. **F17**). The polarity zone correlative to C2An (the Gauss Chron) is recognized from ~38 to ~59 mcd, although the upper boundary is poorly defined, and the two short reversed polarity subzones within it are not recognizable. The Gilbert Chron (C3n) is only partially recognizable. For cores below ~60 mcd, the record cannot be reliably interpreted in terms of polarity chrons. Although some parts of cores yield apparently consistent results, the directions are scattered, and patterns in one hole are not replicated in the others. Weak magnetization intensities are not the cause of the poor-quality data. The cores have magnetization intensities at least an order of magnitude above magnetometer noise level, equivalent to a magnetization intensity of ~3×10^{-5} A/m (Fig. **F16**). The probable cause of the poor data quality is the effect of drilling disturbance on the poorly consolidated Upper Cretaceous and Paleocene–Oligocene sediments. In many places, it was noted that identifiable bedding features in these watery sediments are highly deformed, pushed downward at the edges of the core, sometimes by tens of centimeters. If these cores are to produce a magnetic stratigraphy, it must come from discrete samples to be analyzed on shore.

Although only a few polarity zone boundaries can be recognized, these are sufficient to construct an age-depth curve for sediments in the upper 60 m of the section. The curve is remarkably linear, implying a nearly constant sedimentation rate of ~16 m/m.y. in Pliocene–Pleistocene time (Fig. **F18**). This sedimentation rate is in good agreement with that derived from biostratigraphy (~13.4 m/m.y.).

F16. Archive-half magnetization intensities after AF demagnetization at peak fields of 20 mT, Hole 1209A, p. 52.

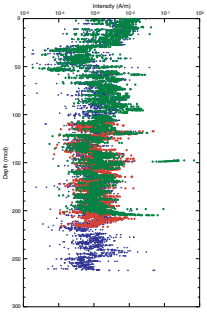

F17. Inclination after AF demagnetization at peak fields of 20 mT, Holes 1209A and 1209B, p. 53.

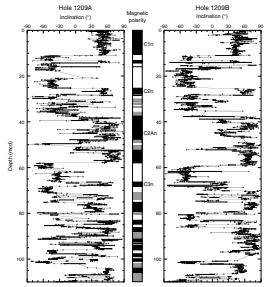

F18. Age-depth curve derived from magnetic stratigraphy, p. 54.

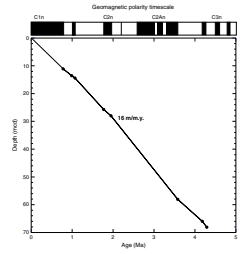

COMPOSITE DEPTHS

MST and spectral reflectance (L*) data collected from Holes 1209A, 1209B, and 1209C were used to determine depth offsets in the composite section. Magnetic susceptibility, gamma ray attenuation (GRA) bulk density, and spectral reflectance measurements were the primary parameters used for core-to-core correlation. GRA bulk density and magnetic susceptibility data were collected at 2.5-cm (Hole 1209A) and 3-cm (Holes 1209B and 1209C) intervals on all APC cores, and at 3-cm intervals on two XCB cores from Hole 1209A. Spectral reflectance data were collected at 2.5-cm intervals on all cores from Site 1209 (see **"MST Measurements,"** p. 29, in "Physical Properties" and **"Lithostratigraphy,"** p. 9, for details about MST and spectral reflectance data).

The data used to construct the composite section and determine core overlaps are presented in a composite depth scale in Figure **F19.** The depth offsets that comprise the composite section for Holes 1209A, 1209B, and 1209C are given in Table **T6.** Units for the composite depth scale are mcd.

The composite data show that the APC cores from Site 1209 provide a continuous overlap to at least 260 mcd (K/T boundary; e.g., in Core 198-1209C-15H). Below the K/T boundary, most of the cores from Holes 1209B and 1209C could not be correlated and placed into a composite depth framework.

Following construction of the composite depth section for Site 1209, a single spliced record was assembled for the aligned cores over the upper 260 mcd by using cores from all three holes. Intervals having significant disturbance or distortion were avoided. Expansion of sedimentary features in one hole relative to coeval cores in the other hole indicate distortion of the cored sequence. Because some distortion occurred within individual cores on depth scales of <9 m, it was not possible to align accurately every feature in the MST and color reflectance records by simply adding a constant to the mbsf core depth. The K/T boundary interval in the composite was taken from Core 198-1209C-15H. Magnetic susceptibility data from the three holes for the Eocene/Oligocene boundary and Paleocene/Eocene boundary intervals are shown in Figures **F20** and **F21.** The Site 1209 splice (Table **T7**) can be used as a sampling guide to recover a single sedimentary sequence between 0 and 260 mcd and can be used to plot other data sets from this site.

SEDIMENTATION AND ACCUMULATION RATES

Unconformities and changes in sedimentation rate at Site 1209 are illustrated in a plot of calcareous microfossil datum ages (first and last occurrences) vs. depth (Fig. **F22**). These rates rely on major calcareous nannofossil and planktonic foraminiferal datums presented in Tables **T2** and **T3.** The Pleistocene–Maastrichtian section cored at Site 1209 is punctuated by one major unconformity between the lower Miocene and lower Oligocene, as well as an interval of diastems and/or multiple condensed intervals in the upper Miocene to lower Miocene (Figs. **F23, F24**).

An expanded view of the Nogene (Fig. **F23**) shows that the upper Miocene–Pleistocene part of the section accumulated at an average rate of 13.4 m/m.y. Dark-colored, clay-rich sediments in Cores 198-1209A-10H and 11H and Core 198-1209B-10H and 11H may represent multiple condensed intervals and/or diastems in the upper Miocene to lower

F19. Magnetic susceptibility and GRA bulk density data, p. 55.

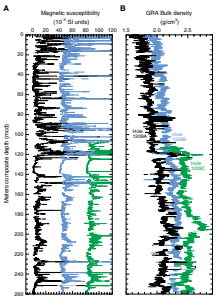

T6. Composite depth section, p. 89.

F20. Magnetic susceptibility data, 135 to 157 mcd, p. 56.

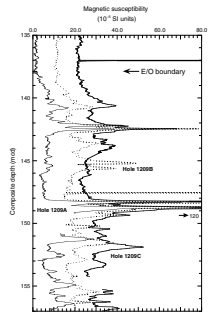

F21. Magnetic susceptibility data, 202 to 217 mcd, p. 57.

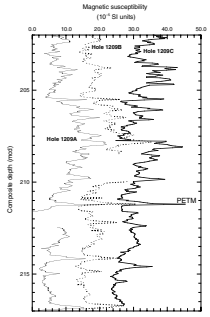

T7. Splice tie points, p. 90.

Miocene interval. The dark-colored layers in Sections 198-1209A-12H-4 through 12H-6 and Sections 198-1209B-12H-6 through 12H-CC and 13H-1 likely correspond to condensed section and/or major unconformity separating the lower Miocene and the lower Oligocene (Fig. F24).

Sedimentation rates in the lower Oligocene–lower Paleocene interval range between 1.5 and 5.2 m/m.y., with the lowest rates occurring in the upper middle Eocene to upper Eocene and in the basal Paleocene (Figs. F25, F26). Rates for the Maastrichtian were significantly higher, ranging from 8.1 to 23.9 m/m.y. (Fig. F26).

Mass accumulation rates for the bulk sediment, carbonate, and noncarbonate fractions were calculated using dry bulk density (see "Physical Properties," p. 29) and carbonate concentration (see "Organic Geochemistry," p. 25) data through 12 linear sedimentation rate segments in the Cretaceous–Neogene section recovered at Site 1209 (Table T8). These segments were chosen to reflect the major changes in sedimentation rate. Physical properties and carbonate content analyses were not performed within certain intervals of stratigraphic importance. Mass accumulation rate data are not available for these intervals (Table T8).

During the Maastrichtian, the average bulk sediment accumulation rate decreased from 2.7 to 1.0 g/cm²/k.y. Further decrease in the average rate of bulk sediment accumulation to 0.5 g/cm²/k.y. coincided with the K/T boundary (Fig. F27). With the exception of an interval during the middle to late Eocene (~44–34 Ma) when the average decreased to 0.2 g/cm²/k.y., the bulk sediment accumulation rate remained relatively constant from early Paleocene to early Oligocene time (Fig. F25). Age-depth relationships for segments 2 and 3 (Table T8), which lie between middle Miocene and lower Miocene–upper Oligocene unconformities, indicate that sedimentation rates were 18.9 and 4.4 m/m.y., respectively. The average bulk sediment accumulation rates that correspond to these segments are 0.5 g/cm²/k.y. (segment 3) and 1.9 g/cm²/k.y. (segment 2). By contrast, the upper Miocene–Pleistocene was characterized by continuous sedimentation (Fig. F23), although the bulk accumulation rate decreased slightly through this interval, from 1.3 g/cm²/k.y. at 5.8 Ma to ~1.0 g/cm²/k.y. in the youngest sediments recovered. The carbonate accumulation rate approximates that of the bulk sediment in segments 2–12 (Table T8). The noncarbonate fraction, composed largely of siliceous biogenic material, clay, and volcanic ash, became more significant during the last 6 m.y., making up an average of 27 ± 15 wt% of the accumulating sediment.

ORGANIC GEOCHEMISTRY

Volatile Hydrocarbons

Headspace gas analysis was conducted as part of the standard protocol required for shipboard safety and pollution prevention monitoring. A total of 21 cores from Hole 1209A were evaluated (Table T9). The concentrations of CH_4 were at background levels (range = 1.7–2.3 ppmv); no hydrocarbon gases higher than C_1 were detected.

Carbonate

Carbonate determinations by coulometry were made for a total of 67 samples from Hole 1209A (Table T10). Samples were selected to provide

F22. Age-depth plot of calcareous nannofossil and planktonic foraminiferal datums, p. 58.

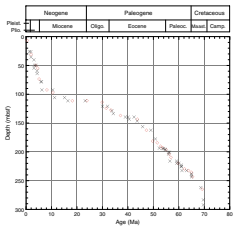

F23. Age-depth plot of Neogene calcareous nannofossil and planktonic foraminiferal datums, p. 59.

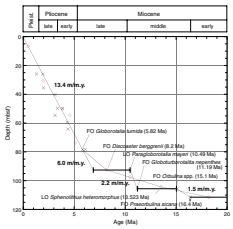

F24. Age-depth plot of early Miocene–late Eocene calcareous nannofossil and planktonic foraminiferal datums, p. 60.

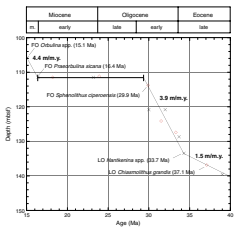

F25. Age-depth plot of early Oligocene–late Paleocene calcareous nannofossil and planktonic foraminiferal datums, p. 61.

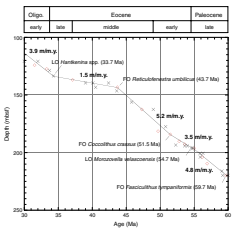

a measure of the carbonate contents within different units and to assess the influence of carbonate content on color reflectance. The values for carbonate range from 4 to 89 wt% (Table T10) in Unit I, reflecting antithetic variations in the proportions of biogenic silica and carbonate. The profile of carbonate contents shows considerable variation downcore (Fig. F28), which primarily reflects the choice of intervals representative of extremes in color and lithology. The highest carbonate contents measured in Unit II exceed those in Unit I, and variability decreases. The calcareous oozes of the Maastrichtian (Unit III) have uniformly high carbonate contents.

INORGANIC GEOCHEMISTRY

Interstitial Water Chemistry

A total of 14 interstitial water samples were collected from Hole 1209A: 11 samples between 0 and 100 mbsf (one sample per core) and 3 between 137 and 250 mbsf. The lower sampling resolution toward the bottom of the hole reflects an effort to avoid disturbing intervals of critical stratigraphic importance. Details of analytical methods can be found in "Inorganic Geochemistry," p. 21, in the "Explanatory Notes" chapter. Filtered (0.45 µm) samples were analyzed for pH, salinity, chlorinity (Cl^-), alkalinity, sulfate (SO_4^{2-}), phosphate (HPO_4^{2-}), ammonium (NH_4^+), silica ($Si(OH)_4$), boron (H_3BO_3), iron (Fe^{2+}), manganese (Mn^{2+}), and major cations (Na^+, K^+, Mg^{2+}, Ca^{2+}, Li^+, Sr^{2+}, and Ba^{2+}). A compilation of data is provided in Table T11. Cited values for average seawater composition are from Millero and Sohn (1992) and Broecker and Peng (1982).

The pore water samples span lithologic Units I (0.0–84.2 mbsf) and II (84.2–235.0 mbsf) and extend into the uppermost part of Unit III (235.0–297.0 mbsf). The compositional differences among these lithologic units play a role in controlling downcore trends in pore water geochemistry. Lithologic Unit I, primarily nannofossil ooze with varying amounts of clay, contains disseminated volcanic glass and discrete ash layers. Pyrite in laminae and blebs is common in the upper ~37 m. Lithologic Unit II, composed of nannofossil ooze and clayey nannofossil ooze with clay-rich horizons, is marked by a higher overall carbonate content and an absence of volcanic ash and pyrite. The sediment of lithologic Unit III consists of clay-poor nannofossil ooze, and chert in discrete layers.

pH, Salinity, Chloride, and Sodium

The pH of pore waters in Hole 1209A range from 7.12 to 7.54, with an average value of 7.36 ± 0.12 (Table T11). All values are lower than that of average seawater (pH = 8.1). Much of the variability in the pH profile is contained within the Neogene sediments of lithologic Unit I, which is characterized by a high proportion of noncarbonate sediment (biogenic silica, ash, detrital silicates, and hemipelagic mud) relative to underlying sediments (see "Lithostratigraphy," p. 9). The relatively narrow range of values below ~100 mbsf reflects the buffering capacity of the carbonate-dominated Paleogene–Cretaceous sediment. Salinity remains at 35 g/kg throughout the profile.

As at other Leg 198 sites, the chloride (Cl^-) profile exhibits only minor fluctuations. Concentrations increase from 551 mM in the shallow-

F26. Age-depth plot of middle Eocene–Maastrichtian calcareous nannofossil and planktonic foraminiferal datums, p. 62.

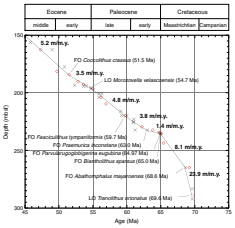

T8. Linear sedimentation rate segments and average accumulation rates, p. 91.

F27. Mass accumulation rates vs. depth and age for the Maastrichtian–Pleistocene, p. 63.

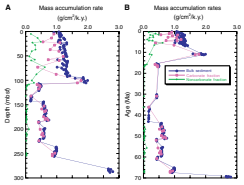

T9. Headspace CH_4 concentrations, p. 92.

T10. Carbonate contents, p. 93.

F28. Carbonate profile, p. 64.

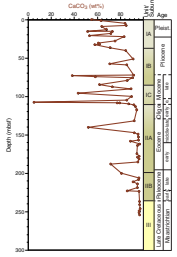

T11. Results of geochemical analyses, p. 94.

est sample (5.95 mbsf) to 569 mM near the bottom of the profile at 164.40 mbsf (Table T11). Sodium (Na^+) concentrations, calculated by charge balance, show a slight increase downcore from ~470 mM at the top to ~480 mM near the bottom of the profile (Table T11). Broad downcore variations in pore water Na^+ and Cl^- profiles of pelagic sediments have been linked to variations in mean ocean salinity associated with changes in ice volume (McDuff, 1985).

Alkalinity, Sulfate, Ammonium, Phosphate, Iron, and Manganese

Relative to Sites 1207 and 1208, pore water SO_4^{2-}, alkalinity, NH_4^+, and HPO_4^{2-} concentrations are low and uniform (Fig. F29A, F29B, F29C, F29D). The SO_4^{2-} concentrations decrease steadily from the average seawater value of 28 mM in the shallowest sample (5.95 mbsf) to 23 mM at the base of the profile. Given that sulfate reduction tends to increase alkalinity at the rate of 2 moles of HCO_3^- for every mole of SO_4^{2-} reduced, a downcore increase in alkalinity on the order of 10 mM would be expected at Site 1209. Alkalinity values, however, are low throughout the profile (2.94 ± 0.32 mM) and show a slight decrease downcore from values slightly higher to values similar to that of the overlying seawater (Fig. F29A). The decreasing trend suggests that ~7–10 mM of alkalinity have been consumed. Carbonate precipitation is one process that might be responsible for the observed alkalinity decrease. Ammonium (NH_4^+) and HPO_4^{2-} concentrations are extremely low throughout Hole 1209A, with values ranging from 49 to 64 µM and 1 to 3 µM, respectively. These low and uniform values reflect the very low organic matter content of the sedimentary section (see "Organic Geochemistry," p. 25).

The Fe^{2+} and Mn^{2+} concentrations decrease sharply through the upper ~40 m of the sediment column (Fig. F29E, F29F). The Fe^{2+} concentrations decrease from 47 to 17 µM over this interval; the lower part of the Fe^{2+} profile fluctuates between values of 16 and 28 µM. These variations are attributed largely to the proximity of iron sources (i.e., volcanic ash) to sites of pyrite formation in the Neogene section (see "Lithostratigraphy," p. 9). Variations in pore water Fe^{2+} are generally more subdued than those observed at Sites 1207 and 1208 and reflect lower rates of sulfate reduction at Site 1209, as indicated by the SO_4^{2-} profile (Fig. F29B).

The Mn^{2+} profile at Site 1209 is similar to the profiles at Sites 1207 and 1208 (Fig. F29F). Manganese concentrations decrease from 8 µM in the shallowest sample at 5.95 mbsf to 1 µM at ~40 mbsf. Elevated concentrations in the upper part of the sediment column suggest that degradation of the little organic matter present is sufficient to drive manganese reduction. An excursion to higher manganese concentrations in the lower part of the profile (~80–30 mbsf) encompasses a number of condensed intervals and disconformities within the lower Neogene and upper Paleogene section, which contain inferred Mn-rich phases (see "Lithostratigraphy," p. 9). As such, this increase in Mn^{2+} concentrations is interpreted to reflect the dissolution of Mn minerals and diffusion of Mn^{2+} away from Mn-rich horizons.

F29. Alkalinity, sulfate, ammonium, phosphate, iron, and manganese profiles, p. 65.

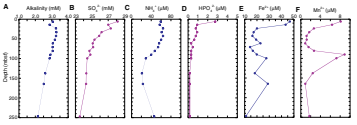

Potassium, Calcium, Magnesium, Lithium, and Strontium

Potassium (K^+) concentrations show a gradual decrease downcore in Hole 1209A from a maximum of 11.8 mM in the shallowest sample (5.95 mbsf) to values approaching that of average seawater (10.2 mM) in the deepest sample at 257.15 mbsf (Fig. F30A). Elevated concentrations correspond to the distribution of volcanic ash in the upper ~80 m of the hole (see "Lithostratigraphy," p. 9), suggesting that the major source for K^+ in the pore water is glass-rich, silicic volcanic material. K^+ is liberated from the solid phase via leaching and weathering reactions that produce clays (i.e., smectite). The downcore decrease in K^+ is interpreted to reflect the absence of ash in the Paleogene and Cretaceous sediments, diffusion toward greater depths, and possible exchange with basaltic basement.

Concentrations of Ca^{2+} and Mg^{2+} are similar to that of average seawater (10.3 and 53.2 mM, respectively) at the top of the pore water profile and show an antithetic relationship downcore (Fig. F30B, F30C). Ca^{2+} concentrations increase downcore from 10.8 mM at the top to 15.7 mM at the base of the profile, whereas Mg^{2+} concentrations decrease from 53.1 to 44.8 mM. The most likely influences on Ca^{2+} and Mg^{2+} concentrations in pore waters at Site 1209 include calcium carbonate dissolution, weathering reactions involving volcanic ash in the Neogene section, and alteration processes involving the volcanic basement. Whereas carbonate dissolution releases both cations to pore waters, the latter two processes release Ca^{2+} and remove Mg^{2+} from the system.

The Li^+ profile (Fig. F30D) shows a gradual increase from a concentration similar to that of overlying seawater throughout the upper ~100 m of the profile (19.4 ± 1.6 µM) to 69.0 µM at the base of the profile (247.15 mbsf). The lower concentrations through the upper ~100 m of the profile may reflect uptake by clay minerals formed through the weathering of volcanic material and, possibly, zeolites (Gieskes, 1981) in lithologic Unit I. The similarity of the Li^+ profile to the Ca^{2+} profile (increasing concentration with increasing depth) and its antithetic relationship with the Mg^{2+} and K^+ profiles suggests that increasing concentrations of Li^+ with depth may reflect alteration reactions involving volcanic basement (~850 mbsf). Geochemical studies of seafloor vent systems have demonstrated that significant quantities of Li^+ may be released as a consequence of exchange between seawater and basalt, even at low temperatures (Millero and Sohn, 1992).

The convex-upward nature of the upper parts of the Sr^{2+} and Sr/Ca pore water profiles (Fig. F30E) suggests that the highest rates of carbonate alteration are occurring within the upper ~50–80 m of the sediment column (e.g., Baker et al., 1982). Below this depth, there is little change in either the Sr^{2+} or Sr/Ca profile, indicating that little additional Sr^{2+} is being added to the system. The lack of variability in the lower part of the profile likely reflects buffering capacity of the carbonate-dominated Paleogene–Cretaceous sediment, which has not been buried to sufficient depth for the onset of pressure solution.

F30. Potassium, calcium, magnesium, strontium, and lithium profiles, p. 66.

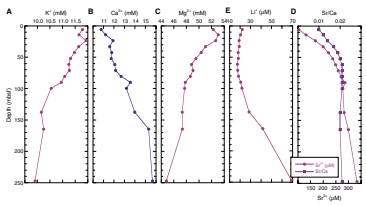

Silica

Although maximum concentrations are lower, the morphology of the dissolved silica ($Si(OH)_4$) profile at Site 1209 is similar to those observed at Sites 1207 and 1208 (Fig. F31; also see Fig. F42, p. 95, in the

F31. Silica profile, p. 67.

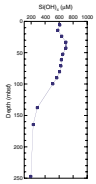

"Site 1207" chapter and Fig. F32, p. 66, in the "Site 1208" chapter). Pore water silica concentrations are highest in the upper ~100 m of the profile in Neogene sediments, with average concentrations of 620 ± 55 µM. Concentrations decrease sharply to 287 µM at 137.65 mbsf. The lowest $Si(OH)_4$ concentration, 197 µM, is encountered at the bottom of the profile. High concentrations in the upper part of the profile are interpreted to reflect the leaching and weathering of volcanic ash in lithologic Unit I. Lower pore water $Si(OH)_4$ concentrations correspond to the disappearance of ash at ~100 mbsf and the appearance of chert in Cretaceous sediments encountered in Holes 1209B and 1209C. The removal of $Si(OH)_4$ from pore waters may be induced by the recrystallization of opal-A to opal-CT or quartz (Baker, 1986; Gieskes, 1981).

Boron and Barium

The significance of variations in the Ba^{2+} and dissolved boron (generated mostly as boric acid, H_3BO_3, at the measured pH levels) concentrations in pore waters of pelagic sediments are not well understood. Pore water profiles at Site 1209 are described largely for purposes of documentation. The data are provided in Table T11. The average dissolved boron concentration (444 ± 13 µM) is somewhat higher than that of average seawater (416 µM). H_3BO_3 concentrations show an increase below ~100 mbsf to 469 µM. The Ba^{2+} concentrations in interstitial waters of Hole 1209A average 0.5 ± 0.4 µM and show little variability with depth. Concentrations in the upper half of the profile are extremely low, but on average, higher than those of average seawater, indicating that Ba^{2+} is being added to the system. Possible sources of Ba^{2+} include skeletal debris and volcanic ash, which may be undergoing leaching and/or dissolution.

PHYSICAL PROPERTIES

Physical properties at Site 1209 were measured on both whole-round sections and discrete samples from split core sections. Continuous whole-round measurements were made of magnetic susceptibility, GRA bulk density, and compressional *P*-wave velocity using the MST. Whole-round sections of some cores were also measured for natural gamma radiation (using the MST) and discrete measurements of thermal conductivity. Discrete compressional *P*-wave velocity was measured at a frequency of at least one measurement per split-core section in Holes 1209A, 1209B, and 1209C. Index properties were measured on discrete samples from split core sections at a frequency of one measurement per section throughout Hole 1209A and in Cores 198-1209B-27H and 31H.

MST Measurements

All core sections from Holes 1209A, 1209B, and 1209C were routinely measured on the MST for magnetic susceptibility and GRA density at 2.5-cm (Hole 1209A) or 3-cm (Holes 1209B and 1209C) intervals (Figs. F32, F33). MST *P*-wave velocity was routinely measured at 10-cm intervals in all APC cores (Fig. F34), but was not measured on XCB cores because of the poor contact between the sediment and core liner. Natural gamma radiation was measured on the MST at 30-cm intervals in some Cenozoic cores and at 20-cm intervals in some cores of late

F32. Whole-core MST magnetic susceptibility, p. 68.

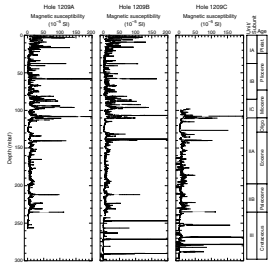

F33. Whole-core MST GRA bulk density, p. 69.

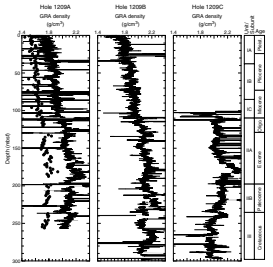

F34. Whole-core MST and discrete *P*-wave velocity, p. 70.

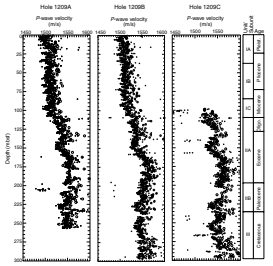

Eocene, late Paleocene, and Late Cretaceous age (Fig. **F35**). All collected MST data are archived in the Ocean Drilling Program Janus database.

Magnetic susceptibility values (Fig. **F32**) are generally higher in the uppermost ~115 m of the Site 1209 sedimentary column. The low magnetic susceptibility values in the sediments below ~115 mbsf correlate with the collection of weak magnetic inclination data from these sediments (see **"Paleomagnetism,"** p. 23). Peaks in magnetic susceptibility in lithologic Subunits IA and IB may correlate with distinct ash layers (see **"Lithostratigraphy,"** p. 9). In the Pleistocene–Pliocene section an excellent correlation is observed between magnetic susceptibility data and color reflectance measurements, primarily the total reflectance value (L*) and the 550-nm wavelength (see **"Lithostratigraphy,"** p. 9). Both magnetic susceptibility and color reflectance data in this interval reveal a pronounced cyclicity, which may be useful in identifying astronomically controlled depositional processes. Magnetic susceptibility values are higher in lithologic Subunit IC, relative to Subunit IB. At ~130 mbsf there is a small downhole increase in magnetic susceptibility, which corresponds closely to the Eocene/Oligocene boundary. Subunits IIA and IIB are generally characterized by fairly constant magnetic susceptibility values. Small magnitude peaks in magnetic susceptibility within Subunits IIA and IIB are generally short-lived events such as that at ~198 mbsf that correlates with the Paleocene/Eocene boundary (see **"Lithostratigraphy,"** p. 9 and **"Biostratigraphy,"** p. 16). The Cretaceous/Tertiary boundary is marked in Holes 1209A and 1209C by a large, sharp peak in magnetic susceptibility, associated with an increase in clay content and perhaps corresponding to a microspherule horizon (see **"Lithostratigraphy,"** p. 9, and **"Organic Geochemistry,"** p. 25). In lithologic Unit III magnetic susceptibility values are generally close to background and do not exhibit any consistent downhole variation, except some excursions that are related to chert horizons.

MST GRA bulk density data exhibit a general downhole increase in magnitude from the seafloor to ~111 mbsf (Fig. **F33**), resulting from sediment compaction and dewatering processes with increased overburden pressure. Cyclical variation in GRA bulk density values, similar to that evident in magnetic susceptibility and color data (see **"Lithostratigraphy,"** p. 9), is found within Pleistocene–Miocene lithologic Unit I. At the boundary between lithologic Subunit IC and Subunit IIA (~111 mbsf; Paleogene/Neogene boundary) there is a distinct downhole increase in GRA bulk density. GRA bulk density values then gradually increase, reach a peak, and then decrease between ~111 and 150 mbsf. From 150 mbsf, GRA bulk density values increase rapidly to a maximum value at ~185 mbsf. Between 185 and 200 mbsf, GRA bulk density values decrease somewhat between 200 and 235 mbsf. At the boundary between Subunit IIB and Unit III (~235 mbsf; Cretaceous/Tertiary boundary) a pronounced high peak in GRA density values is recorded.

GRA bulk density values are consistently higher than the discrete wet bulk density measurements (Fig. **F33;** Table **T12**) throughout Hole 1209A. These overestimated GRA bulk density values can be explained by the relatively high carbonate content, porosity, and moisture content of sediments; the calibration procedure for the MST GRA sensor is optimized for mixed-lithology sediments. Consequently, the GRA method overestimates the density in carbonate-rich sediments of all lithologic units. This phenomenon is most pronounced in lithologic Units II and III because these sediments have the highest carbonate contents (see **"Lithostratigraphy,"** p. 9, and **"Organic Geochemistry,"** p. 25). During the acquisition of GRA bulk density data from Site 1209,

F35. MST natural gamma radiation, p. 71.

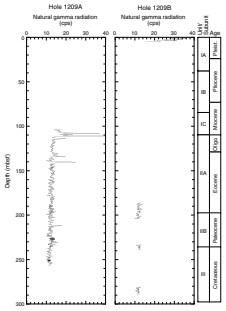

T12. Discrete index properties measurements, p. 95.

a number of steps to extremely high values (~>2.4 g/cm^3) were noted and these data are clearly offset from the general downhole trends within the data set. These anomalous data were subsequently traced to a malfunction of the GRA detector, and this problem was rectified during the collection of Site 1209 MST data.

MST *P*-wave velocities were recorded at 10-cm intervals in Holes 1209A, 1209B, and 1209C to a depth of ~300 mbsf (Fig. F34). Despite some obviously "out of range" values, a general trend to higher velocities with increased depth in the sediment column can be discerned from values lying between 1500 and 1600 m/s. MST *P*-wave values generally increase in magnitude with depth through lithologic Unit I and most of Subunit IIA. Between ~150 and ~165 mbsf, *P*-wave values increase relatively abruptly from ~1525 to ~1550 m/s. In the lower part of lithologic Subunits IIA and IIB, between ~165 and ~235 mbsf, MST *P*-wave values maintain an almost constant velocity of ~1550 m/s. At ~235 mbsf there is a short-lived increase in *P*-wave velocity that is associated with an interval just above the K/T boundary and the boundary between lithologic Units II and III. In the lower half of lithologic Unit III, *P*-wave velocities are highly variable relative to other parts of the sedimentary column, possibly due to localized lithification. The downhole trend recorded by the reliable MST *P*-wave logger (PWL) values also compare well with the discrete measurements of *P*-wave velocity (Table T13; Fig. F36). However, MST PWL values are consistently lower than discrete values; this may be due to an assumption in the calibration of the MST PWL that the core liner is full of sediment and that there is no water between the liner and the sediment.

Natural gamma radiation data were collected at 30-cm intervals for some cores of Cenozoic age and at 20-cm intervals in cores of late Eocene, late Paleocene, and Late Cretaceous age from Holes 1209A and 1209B (Fig. F35). Natural gamma radiation data were not collected in the upper 100 m of Hole 1209A. Below 100 mbsf, natural gamma radiation values are generally constant. Peak natural gamma radiation values occur at the Oligocene/Miocene boundary, in the upper Eocene sediments, and at the Cretaceous/Paleocene boundary, reflecting a small increase in clay content in the sedimentary record (see "Lithostratigraphy," p. 9).

P-Wave Velocity

Discrete measurements of compressional *P*-wave velocity were made on Site 1209 split-core sections using the modified Hamilton frame (PWS3) velocimeter. These data are listed in Table T13 and illustrated in Figure F36. Data were collected at a routine sampling frequency of one measurement per section. Velocities vary between ~1500 m/s in the soft surface sediments and ~1600 m/s in the more consolidated sediments at Site 1209. Discrete *P*-wave measurements show an increase in velocity with depth between 0 and ~130 mbsf, which is similar to the trend in the reliable data obtained with the MST PWL. The lack of evidence for early diagenetic cementation near the seafloor, as shown by high-percentage porosity in the interval 0–110 mbsf (Fig. F37; Table T12), suggests that increasing *P*-wave velocity with depth in the upper 110 m of the sedimentary column is primarily the consequence of compaction and pore fluid expulsion. A downhole increase in discrete *P*-wave velocities between 0 and 110 mbsf broadly correlates with an increase in the magnitude of discrete bulk density values through this stratigraphic interval (Fig. F38). *P*-wave values then exhibit a slight increase in magni-

T13. Discrete measurements of *P*-wave velocity, p. 98.

F36. *P*-wave velocities for discrete samples, p. 72.

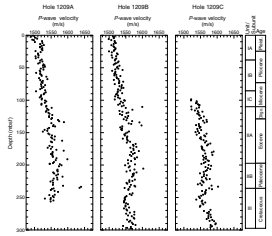

F37. Water content, porosity, and void ratio, p. 73.

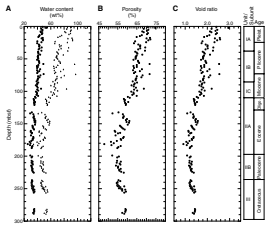

F38. *P*-wave velocities vs. wet bulk density, p. 74.

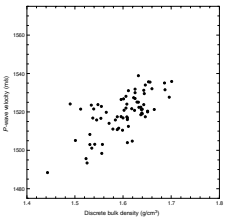

tude between ~110 and ~300 mbsf, from ~1540 to ~1570 m/s. An exception to this general trend occurs (in Holes 1209A and 1209C) at ~235 mbsf, where *P*-wave velocities of up to 1650 m/s are recorded over a thin stratigraphic interval. This peak in *P*-wave velocity is at the boundary between lithologic Subunit IIB and Unit III, which marks the K/T boundary. Recorded *P*-wave velocities in the upper part of lithologic Unit III are slower than those measured at the base of this lithologic unit. The variation in *P*-wave velocity in lithologic Unit III may be due to localized lithification of the Cretaceous sediments increasing with depth in the sedimentary column (see "Lithostratigraphy," p. 9).

Thermal Conductivity

Thermal conductivity data from Site 1209, obtained using the TK04, are listed in Table T14 and shown in Figure F39. Measurements were made on Sections 1 and 3 of each core in Hole 1209A and in Cores 1209B-8H, 10H, and 12H. Average thermal conductivity for the 79 data points is 1.01 W/(m·K), with a standard deviation of 0.18. Thermal conductivity values also exhibit a general increase in magnitude with increasing depth below seafloor from ~0.9 W/(m·K) near the seafloor to ~1.20 W/(m·K) at ~250 mbsf. The downhole increase does not strongly correlate with a decrease in porosity (R^2 = 0.37) (Fig. F40), which could be due to the high degree of scatter in the thermal conductivity data set (Fig. F39).

In Situ Temperature Measurements and Heat Flow

The Adara tool was deployed four times in Hole 1209B, but reliable in situ temperature data were only collected for Cores 198-1209B-8H, 10H, and 12H (Table T15). The bottom-water temperature (~2.2°C) was calculated using the temperature data collected when the Adara tool was equilibrated with ambient temperatures at the mudline. The temperature record from Core 198-1209B-8H (a typical deployment record) shows a well-developed thermal decay subsequent to the penetration of the tool into the sediment (Fig. F41). Penetration of the Adara tool into the formation results in an instantaneous rise in recorded temperature, the result of frictional heating, which is followed by an exponential decrease in temperature as the tool equilibrates with the ambient in situ temperature. The calculated Hole 1209B bottom-water and in situ sediment temperatures are illustrated in Figure F42. The geothermal gradient in Hole 1209B was determined from the four data points shown on the temperature profile in Figure F42. These data values can be fitted with a linear least-squares regression (R^2 = 0.98), with the solution resulting in a 26.65°C/km geothermal gradient. Average heat flow at Site 1209B, determined using an average thermal conductivity value of 1.11 W/(m·K), is 29.58 mW/m².

Index Properties

Index properties were determined for discrete samples from Hole 1209A and Cores 198-1209B-27H and 31H. These data are listed in Table T12 and shown in Figures F37 and F43. Index properties primarily reflect progressive sediment compaction and fluid expulsion with depth in the sediment column, but also indicate changes in sediment composition as defined by lithologic units and subunits (see "Lithostratigraphy," p. 9). Bulk and dry density increase in magnitude

T14. Discrete measurements of thermal conductivity, p. 101.

F39. Whole-core thermal conductivity, p. 75.

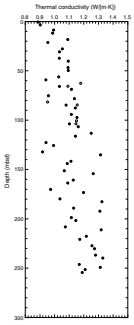

F40. Whole-core thermal conductivity vs. discrete porosity values, p. 76.

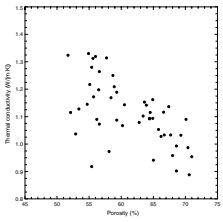

T15. In situ Adara temperature tool measurements, p. 102.

F41. Example Adara temperature data, p. 77.

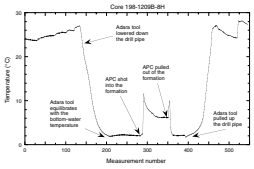

F42. Adara temperature measurements vs. depth, p. 78.

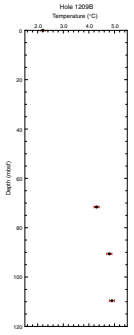

between the seafloor and ~110 mbsf, within lithologic Unit I. Bulk and dry density continue to increase to maximum values within the lower part of lithologic Subunit IIA (~180 mbsf). Between 180 mbsf and the bottom of Hole 1209A (~300 mbsf), both bulk and dry density exhibit a trend to decreasing magnitude. By comparison, grain density exhibits a small general downhole decrease in magnitude. Water content, porosity, and void ratio all show a general decrease in magnitude downhole between the seafloor and ~190 mbsf (lithologic Unit I [Pleistocene–Miocene] and the upper part of Subunit IIA [Oligocene–middle Eocene]). Water content, porosity, and void ratio increase slightly in magnitude between ~200 and ~300 mbsf within lithologic Subunit IIB (Paleocene) and Unit III (Cretaceous). These trends are of interest as the sediments in this interval are less indurated than those recovered above, and this observation is somewhat counterintuitive to the expected general trend of increasing lithification with greater burial depth.

F43. Wet bulk, dry, and grain density vs. depth, Holes 1209A and 1209B, p. 79.

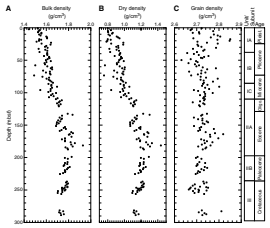

Summary

Physical properties data at Site 1209 show variation with depth below seafloor to ~200 mbsf that suggests control by progressive compaction and fluid expulsion. The physical properties data further suggest that below ~200 mbsf the expected trend of increasing compaction with depth is absent (i.e., downhole, between ~200–300 mbsf, there is generally decreasing GRA density, constant *P*-wave velocity and increasing porosity, void ratio, and water content). A long temporal break in sedimentation at Site 1209, followed by rapid deposition, could explain these phenomena (such as is evident at Site 1207), but at Site 1209 sedimentation rates were almost constant from the Maastrichtian to the middle Eocene (see **"Sedimentation and Accumulation Rates,"** p. 24). Thus, the unusual physical properties data from below ~200 mbsf cannot be explained solely by the sediment burial history at this location. The physical properties data from below ~200 mbsf suggest that there has been less diagenesis and compaction in the sediments below 200 mbsf, relative to those in the interval ~111–200 mbsf. This observation may be a reflection of varying microfossil composition within the Site 1209 sediments and the so-called "diagenetic potential" of different sediments (Schlanger and Douglas, 1974), which in the case of the Site 1209 sediments below ~200 mbsf is obviously low.

REFERENCES

Aubry, M.-P., Berggren, W.A., Stott, L., and Sinha, A., 1996. The upper Paleocene–lower Eocene stratigraphic record and the Paleocene/Eocene boundary carbon isotope excursion: implications for geochronology. *In* Knox, R.W.O'B., Corfield, R.M., and Dunay, R.E. (Eds.), *Correlation of the Early Paleogene in Northwestern Europe*. Spec. Publ.—Geol. Soc. Am., 101:353–380.

Baker, P.A., 1986. Pore-water chemistry of carbonate-rich sediments, Lord Howe Rise, Southwest Pacific Ocean. *In* Kennett, J. P., von der Borch, C.C., *Init. Repts. DSDP,* 90: Washington (U.S. Govt. Printing Office), 1249–1256.

Baker, P.A., Gieskes, J.M., and Elderfield, H., 1982. Diagenesis of carbonates in deep-sea sediments—evidence from Sr^{2+}/Ca^{2+} ratios and interstitial dissolved Sr^{2+} data. *J. Sediment. Petrol.,* 52:71–82.

Barrera, E., Savin, S.M., Thomas, E., and Jones, C.E., 1997. Evidence for thermohaline-circulation reversals controlled by sea level change in the latest Cretaceous. *Geology,* 25:715–718.

Bralower, T.J., in press. Evidence of surface water oligotrophy during the Paleocene–Eocene Thermal Maximum: nannofossil assemblage data from Ocean Drilling Program Site 690, Maud Rise, Weddell Sea. *Paleoceanography.*

Bralower, T.J., Thomas, D.J., Zachos, J.C., Hirschmann, M.M., Röhl, U., Sigurdsson, H., Thomas, E., and Whitney, D.L., 1997. High-resolution records of the late Paleocene thermal maximum and circum-Caribbean volcanism: is there a causal link? *Geology,* 25:963–966.

Bralower, T.J., Zachos, J.C., Thomas, E., Parrow, M., Paull, C.K., Kelly, D.C., Premoli Silva, I., Sliter, W.V., and Lohmann, K.C., 1995. Late Paleocene to Eocene paleoceanography of the equatorial Pacific Ocean: stable isotopes recorded at Ocean Drilling Program Site 865, Allison Guyot. *Paleoceanography,* 10:841–865.

Broecker, W.S., and Peng, T.H., 1982. *Tracers in the Sea*. New York (Eldigio Press).

Caldeira, K., Rampino, M.R., Volk, T., and Zachos, J.C., 1990. Results of biogeochemical modeling at mass extinction boundaries: atmospheric carbon dioxide and ocean alkalinity at the K/T boundary. *In* Walliser, O.H, and Kauffman, E. (Eds.), *Extinction Events in Earth History.* Lect. Notes Earth Sci., 30:333–346.

Cande, S.C., and Kent, D.V., 1995. Revised calibration of the geomagnetic polarity timescale for the late Cretaceous and Cenozoic. *J. Geophys. Res.,* 100:6093–6095.

Dickens, G.R., Castillo, M.M., and Walker, J.G.C., 1997. A blast of gas in the latest Paleocene: simulating first-order effects of massive dissociation of oceanic methane hydrate. *Geology,* 25:258–262.

Dickens, G.R., O'Neil, J.R., Rea, D.K., and Owen, R.M., 1995. Dissociation of oceanic methane hydrate as a cause of the carbon isotope excursion at the end of the Paleocene. *Paleoceanography,* 10:965–971.

Diester-Haass, L., and Zahn, R., 1996. Eocene-Oligocene transition in the Southern Ocean: history of water mass circulation and biological productivity. *Geology,* 24:136–166.

Farrell, J.W., and Prell, W.L., 1989. Climatic change and $CaCO_3$ preservation: an 800,000 year bathymetric reconstruction from the central equatorial Pacific Ocean. *Paleoceanography,* 4:447–466.

Frank, T.D., and Arthur, M.A., 1999. Tectonic forcings of Maastrichtian ocean-climate evolution. *Paleoceanography,* 14:103–117.

Gieskes, J.M., 1981. Deep-sea drilling interstitial water studies: implications for chemical alteration of the oceanic crust, Layers I and II. SEPM Special Publication 32:149–167.

Kaiho, K., 1999. Evolution in the test size of deep-sea benthic foraminifera during the past 120 million years. *Mar. Micropaleontol.,* 37:53–65.

Kelly, D.C., Bralower, T.J., Zachos, J.C., Premoli Silva, I., and Thomas, E., 1996. Rapid diversification of planktonic foraminifera in the tropical Pacific (ODP Site 865) during the late Paleocene thermal maximum. *Geology,* 24:423–426.

Kennett, J.P., and Stott, L.D., 1991. Abrupt deep-sea warming, paleoceanographic changes and benthic extinctions at the end of the Paleocene. *Nature,* 353:225–229.

MacLeod, K.G., and Huber, B.T., 1996. Reorganization of deep ocean circulation accompanying a Late Cretaceous extinction event. *Nature,* 380:422–425.

MacLeod, K.G., Huber, B.T., and Ward, P.D., 1996. The biostratigraphy and paleobiogeography of Maastrichtian inoceramids. *In* Ryder, G., Fastowsky, D., and Gartner, S. (Eds.), *The Cretaceous–Tertiary Event and Other Catastrophes in Earth History.* Spec. Publ.–Geol. Soc. Am., 307:361–373.

McDuff, R.E., 1985. The chemistry of interstitial waters, Deep Sea Drilling Project Leg 86. *In* Heath, G.R., Burckle, L.H., et al., *Init. Repts. DSDP,* 86: Washington (U.S. Govt. Printing Office), 675–687.

McNutt, M.K., Winterer, E.L., Sager, W.W., Natland, J.H., and Ito, G., 1990. The Darwin Rise: a Cretaceous superswell? *Geophys. Res. Lett.,* 17:1101–1104.

Miller, K.G., Fairbanks, R.G., and Thomas, E., 1987. Benthic foraminiferal carbon isotopic records and the development of abyssal circulation in the eastern North Atlantic. *In* Ruddiman, W.F., Kidd, R.B., and Thomas, E., et al., *Init. Repts. DSDP,* 94: Washington (U.S. Govt. Printing Office), 981–996.

Miller, K.G., and Thomas, E., 1985. Late Eocene to Oligocene benthic foraminiferal isotopic record, Site 574, equatorial Pacific. *In* Mayer, L., Theyer, F., Thomas, E., et al., *Init. Repts. DSDP,* 85: Washington (U.S. Govt. Printing Office), 771–777.

Miller, K.G., Wright, J.D., and Fairbanks, R.G., 1991. Unlocking the Ice House: Oligocene-Miocene oxygen isotopes, eustasy, and margin erosion. *J. Geophys. Res.,* 96:6829–6848.

Millero, F.J., and Sohn, M.L., 1992. *Chemical Oceanography.* Florida (CRC Press).

Monechi, S., Angori, E., and von Salis, K., 2000. Calcareous nannofossil turnover around the Paleocene/Eocene transition at Alamedilla (southern Spain). *Bull. Soc. Geol. Fr.,* 171:477–489.

Nakanishi, M., Tamaki, K., and Kobayashi, K., 1989. Mesozoic magnetic anomaly lineations and seafloor spreading history of the northwestern Pacific. *J. Geophys. Res.,* 94:15437–15462.

Norris, R.D., and Röhl, U., 1999. Carbon cycling and chronology of climate warming during the Palaeocene/Eocene transition. *Nature,* 401:775–778.

Nyong, E.E., and Olsson, R.K., 1984. A paleoslope model of Campanian to lower Maestrichtian foraminifera in the North American Basin and adjacent continental margin. *Mar. Micropaleontol.,* 8:437–477.

Okada, H., and Bukry, D., 1980. Supplementary modification and introduction of code numbers to the low-latitude coccolith biostratigraphic zonation (Bukry, 1973; 1975). *Mar. Micropaleontol.,* 5:321–325.

Pflum, C.E., Frerichs, W.E., and Sliter, W.V., 1976. *Gulf of Mexico Deep-water Foraminifers.* Spec. Publ.—Cushman Found. Foraminiferal Res., 14.

Rea, D.K., Basov, I.A., Krissek, L.A., and Leg 145 Scientific Party, 1995. Scientific results of drilling the North Pacific transect. *In* Rea, D.K., Basov, I.A., Sholl, D.W., and Allan, J.F. (Eds.), *Proc. ODP, Sci. Results,* 145: College Station, TX (Ocean Drilling Program), 577–596.

Rea, D.K., and Leinen, M., 1986. Crustal subsidence and calcite deposition in the South Pacific Ocean. *In* Leinen, M., Rea, D.K., et al., *Init. Repts. DSDP,* 92: Washington (U.S. Govt. Printing Office), 299–303.

Röhl, U., Bralower, T.J., Norris, R.D., Wefer, G., 2000. New chronology for the late Paleocene thermal maximum and its environmental implications. *Geology,* 28:927–930.

Schlanger, S.O., and Douglas, R.G., 1974. The pelagic ooze-chalk-limestone transition and its implication for marine stratigraphy. *In* Hsü, K.J., and Jenkyns, H.C. (Eds.),

Pelagic Sediments: On Land and Under the Sea. Spec. Publ.—Int. Assoc. Sedimentol., 1:117–148.

Sliter, W.V., and Brown, G.R., 1993. Shatsky Rise: seismic stratigraphy and sedimentary record of Pacific paleoceanography since the Early Cretaceous. *In* Natland, J.H., Storms, M.A., et al., *Proc. ODP, Sci. Results,* 132: College Station, TX (Ocean Drilling Program), 3–13.

Thierstein, H.R., 1981. Late Cretaceous nannoplankton and the change at the Cretaceous-Tertiary boundary. *In* Warme, J.E., Douglas, R.G., and Winterer, E.L. (Eds.), *The Deep Sea Drilling Project: A Decade of Progress*. Spec. Publ.—Soc. Econ. Paleontol. Mineral., 32:355–394.

Thomas, D.J., Bralower, T.J., and Zachos, J.C., 1999. New evidence for subtropical warming during the late Paleocene thermal maximum: Stable isotopes from Deep Sea Drilling Project Site 527, Walvis Ridge. *Paleoceanography,* 14:561–570.

Thomas, E., 1990. Late Cretaceous–early Eocene mass extinctions in the deep sea. *In* Sharpton, V.L., and Ward, P.D. (Eds.), *Global Catastrophes in Earth History: An Interdisciplinary Conference on Impacts, Volcanism, and Mass Mortality*. Spec. Pap.—Geol. Soc. Am., 247:481–495.

Thomas, E., and Shackleton, N., 1996. The Palaeocene-Eocene benthic foraminiferal extinction and stable isotope anomalies. *In* Knox, R.W.O'B., Corfield, R.M., and Dunay, R.E. (Eds.), *Correlation of the Early Paleogene in Northwest Europe*. Spec. Publ.—Geol. Soc. London, 101:401–441.

Tjalsma, R.C., and Lohmann, G.P., 1983. *Paleocene–Eocene Bathyal and Abyssal Benthic Foraminifera from the Atlantic Ocean*. Spec. Publ.—Micropaleontology, 4.

van Morkhoven, F.P.C.M., Berggren, W.A., and Edwards, A.S., 1986. Cenozoic cosmopolitan deep-water benthic foraminifera. *Bull. Cent. Rech. Explor.—Prod. Elf-Aquitaine,* 11.

Woodruff, F., 1985. Changes in Miocene deep-sea benthic foraminiferal distribution in the Pacific Ocean: relationship to paleoceanography. *In* Kennett, J.P. (Ed.), *The Miocene Ocean: Paleoceanography and Biogeography*. Mem.—Geol. Soc. Am., 163:131–175.

Wright, J.D., Miller, K.G., and Fairbanks, R.G., 1992. Early and middle Miocene stable isotopes: implications for deepwater circulation and climate. *Paleoceanography,* 7:357–389.

Zachos, J.C. and Arthur, M.A., 1986. Paleoceanography of the Cretaceous/Tertiary Boundary Event; inferences from stable isotopic and other data. *Paleoceanography,* 1:5–26.

Zachos, J.C., Arthur, M.A., and Dean, W.E., 1989. Geochemical evidence for suppression of pelagic marine productivity at the Cretaceous/Tertiary boundary. *Nature,* 337: 61–64.

Zachos, J.C., Breza, J.R., and Wise, S.W., 1992a. Early Oligocene ice-sheet expansion on Antarctica: stable isotope and sedimentological evidence from Kerguelen Plateau, southern Indian Ocean. *Geology,* 20:569–573.

Zachos, J.C., Lohmann, K.C., Walker, J.C.G., and Wise, S.W., Jr., 1993. Abrupt climate change and transient climates during the Paleogene: a marine perspective. *J. Geol.,* 101:191–213.

Zachos, J. C., Quinn, T.M., and Salamy, K., 1996. Earliest Oligocene climate transition: constraints from high resolution (10^4 yr) deep-sea foraminiferal $\delta^{18}O$ and $\delta^{13}C$ time-series. *Paleoceanography,* 21:251–266.

Zachos, J.C., Rea, D.K., Seto, K., Niitsuma, N., and Nomura, R., 1992b. Paleogene and early Neogene deep water history of the Indian Ocean: inferences from stable isotopic records. *In* Duncan, R.A., Rea, D.K., Kidd, R.B., von Rad, U., and Weissel, J.K. (Eds.), *Synthesis of Results from Scientific Drilling in the Indian Ocean*. Geophys. Monogr., Am. Geophys. Union, 70:351–386.

Figure F1. Interpretation of seismic reflection profile across Site 1209. Mustard = Miocene to Holocene, light brown = Paleogene, medium green = undifferentiated Cretaceous. For details on the borehole depth to traveltime conversion, see **"Depth-Traveltime Conversion,"** p. 26, in "Physical Properties" in the "Explanatory Notes" chapter. Major reflections are discussed in the text.

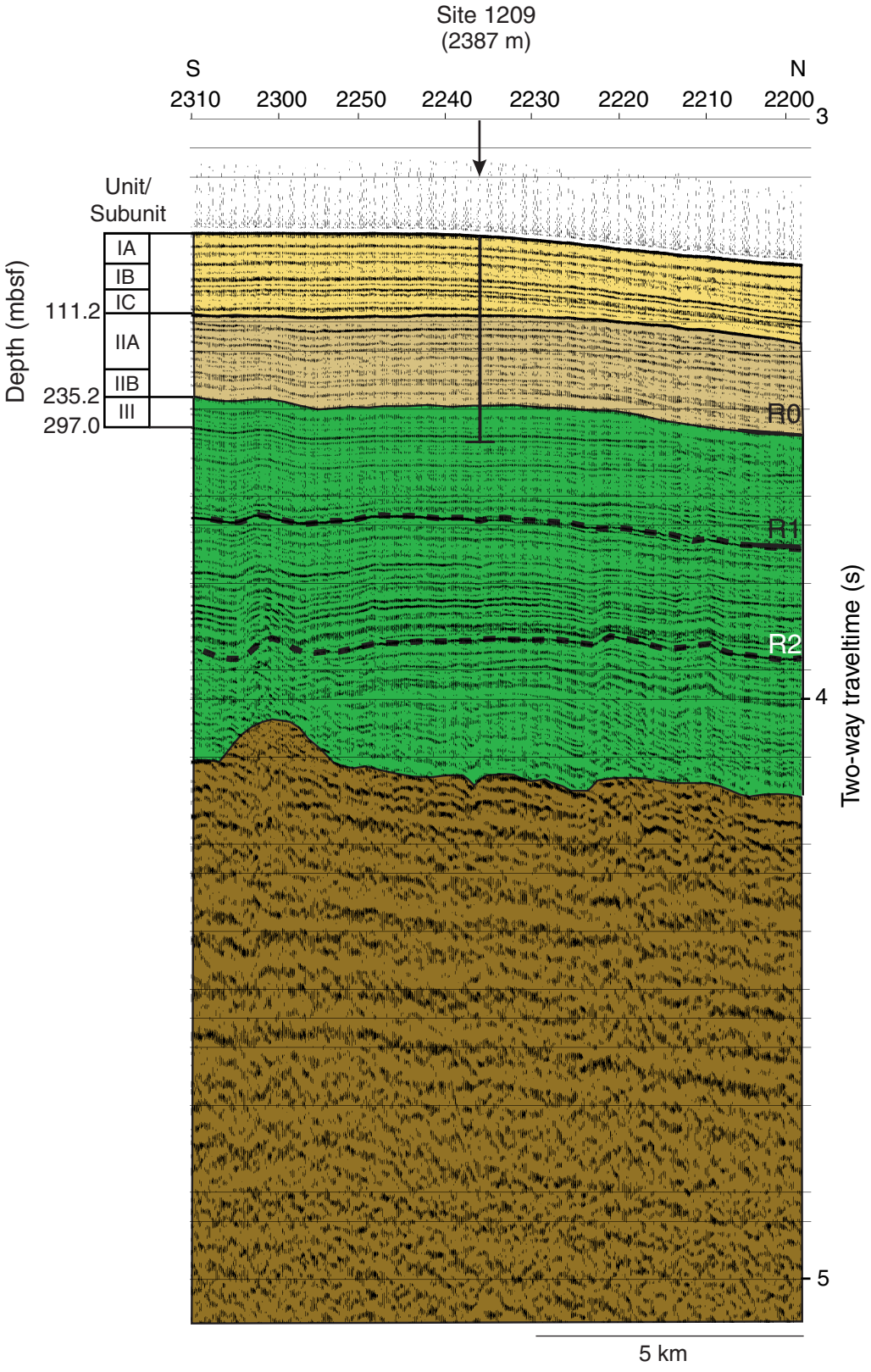

Figure F2. Summary diagram of coring results at Site 1209 plotted on the meters composite depth (mcd) scale. Maximum penetration measured with the drill pipe was 307.5 mbsf. Small gaps (typically 0.5–2.0 m) in core recovery, revealed by hole-to-hole correlation, occur even when nominal core recovery is 100% or more. The accurate correction factor for the raw instrument magnetic susceptibility values is 0.68×10^{-5}. For details about figure symbols and descriptions, see Figure **F12,** p. 101, in the "Leg 198 Summary" chapter.

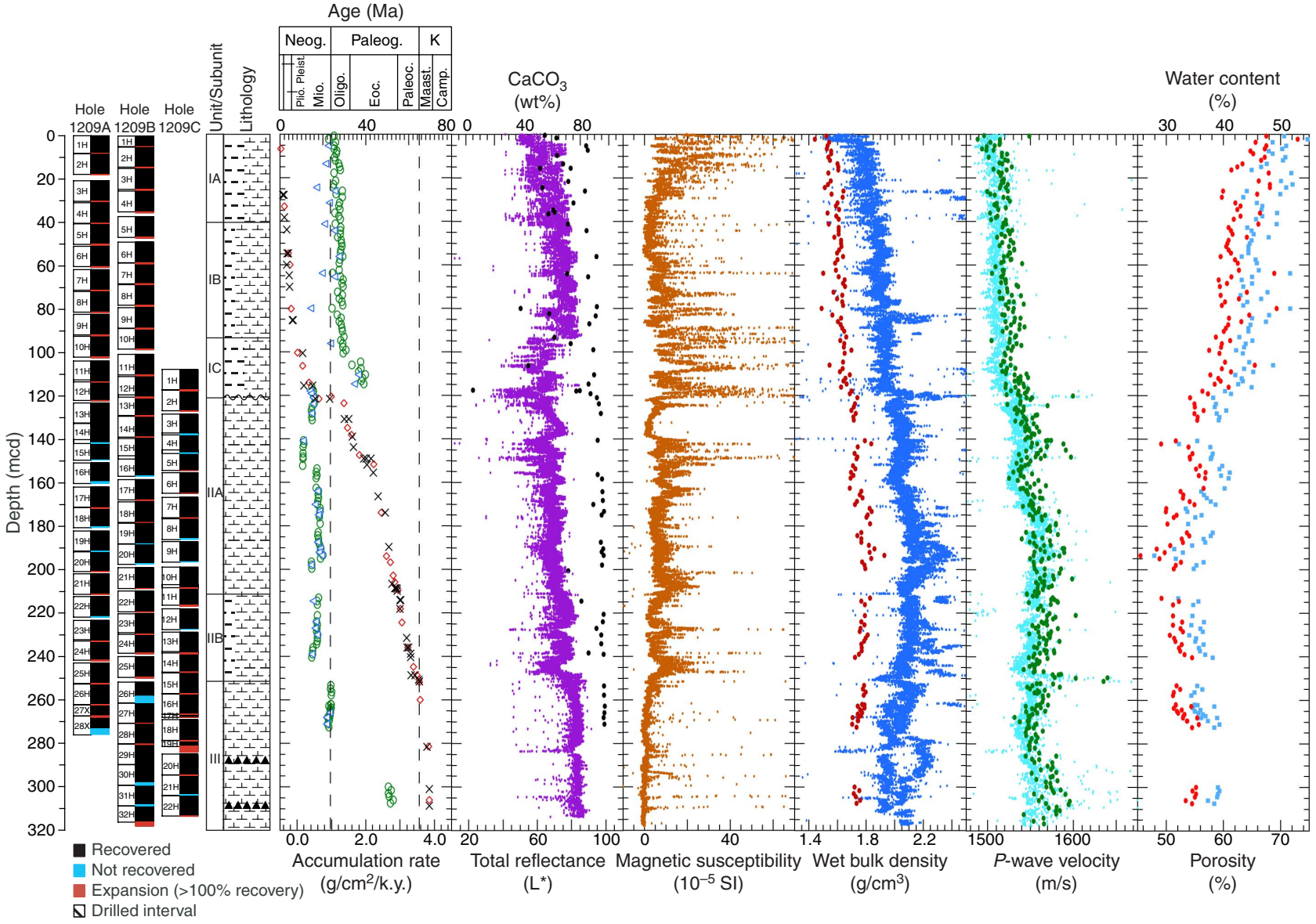

Figure F3. Paleontological summary of the PETM interval in Section 198-1209B-22H-1. The LO of *Morozovella velascoensis,* which defines the boundary between Zone P5 and Subzone P6a, lies between Samples 198-1209B-22H-1, 74–75 and 9–10 cm, probably close to the latter sample. Depths listed along the lithology column are in meters below seafloor (mbsf). FO = first occurrence.

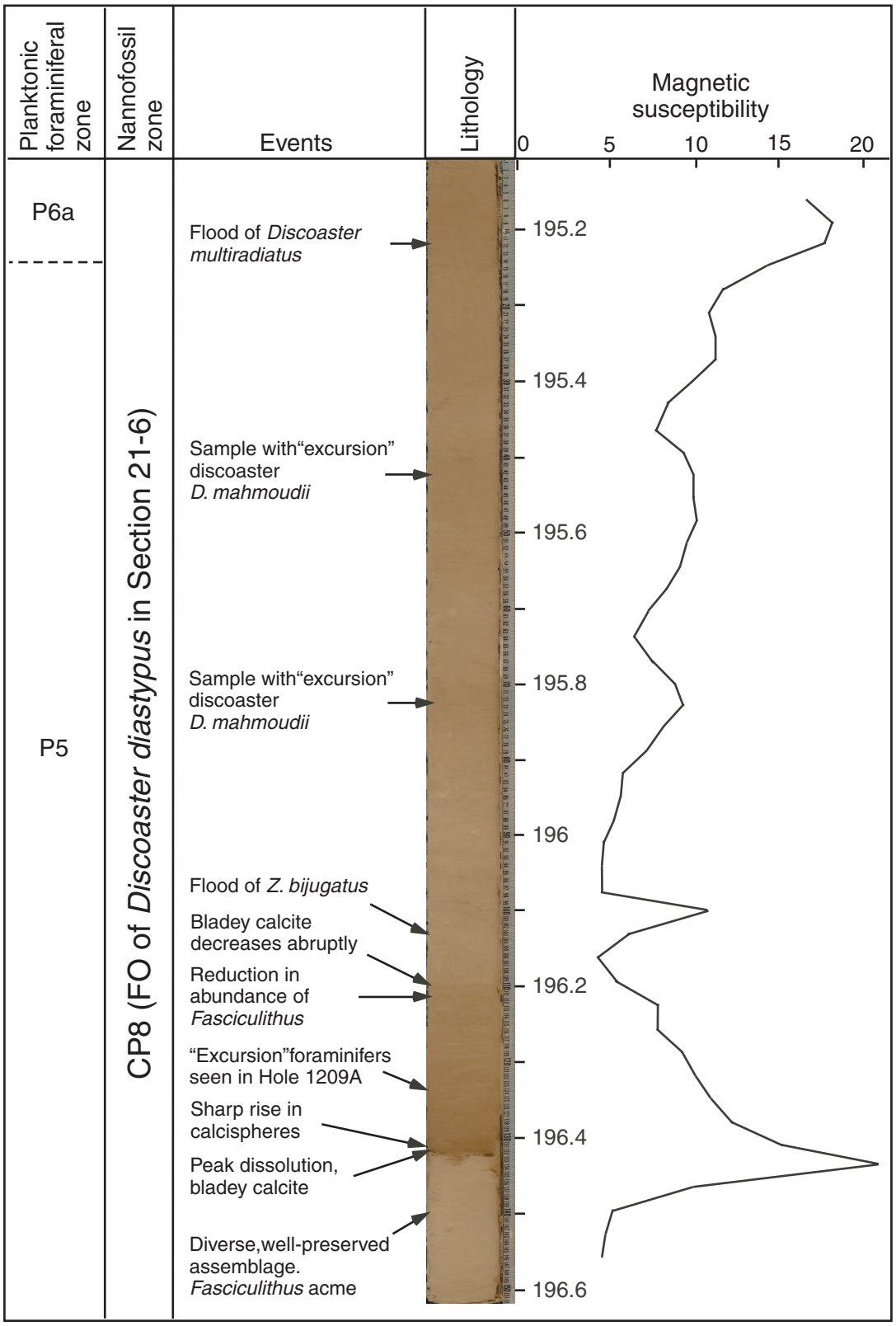

Figure F4. Paleontological summary of the Cretaceous/Tertiary boundary in Holes 1209A and 1209C. Samples described include planktonic foraminifers (F) and nannofossils (N).

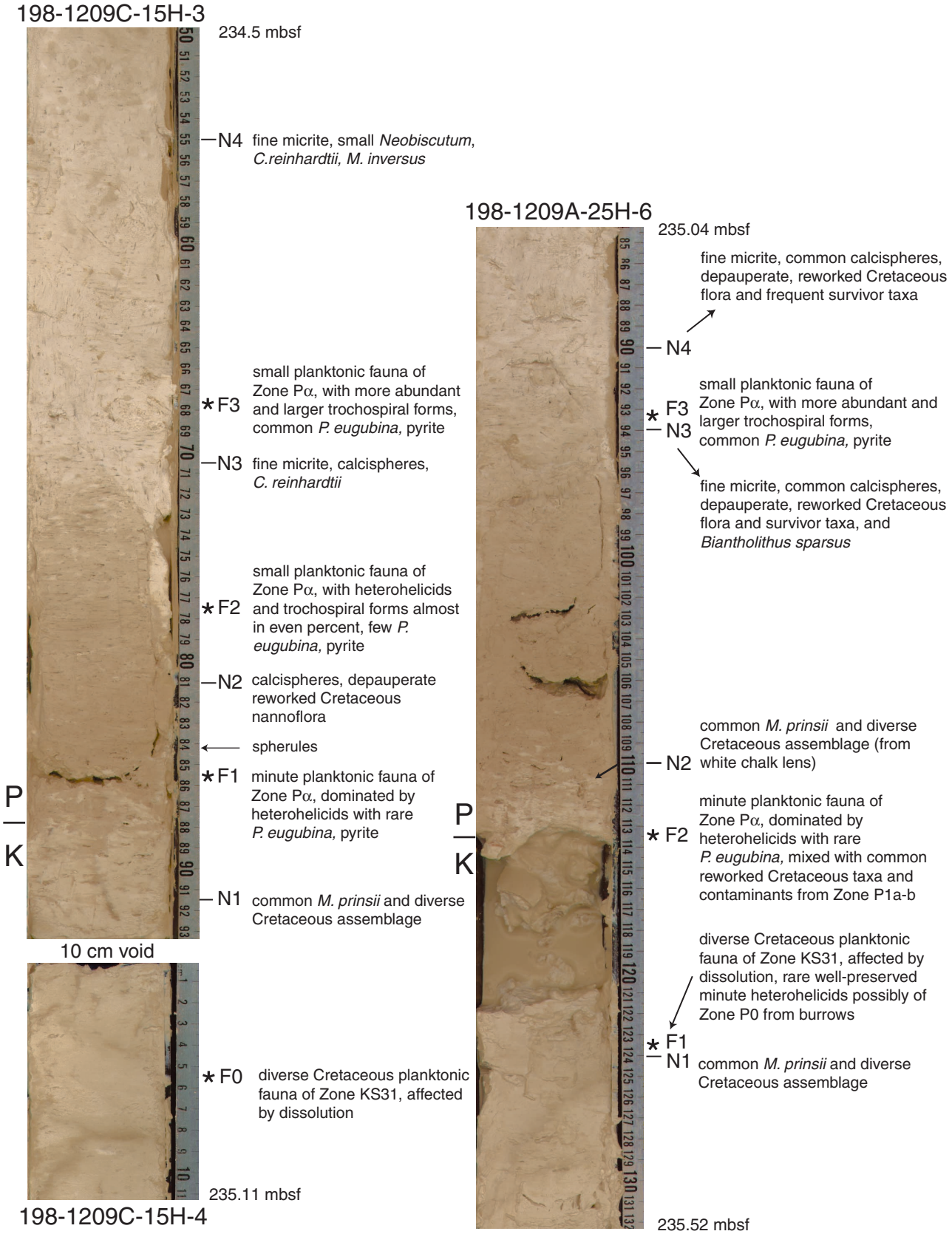

Figure F5. Photographs of (**A**) damaged bit and (**B**) locable float valve. Note the broken hinge pin and chert fragments inside the LFV housing.

A

B

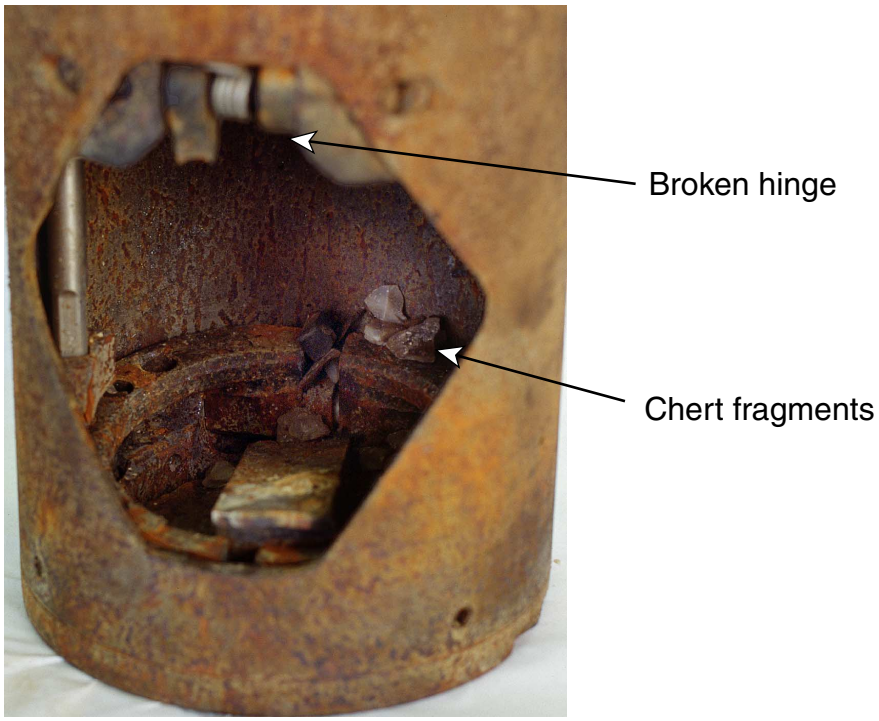

Figure F6. Core recovery, lithology, lithologic units, age with corresponding biostratigraphic zonations, color reflectance (at 550 nm), and percent carbonate for Site 1209. Foram zn. = foraminiferal zone, nanno. zn. = nannofossil zone.

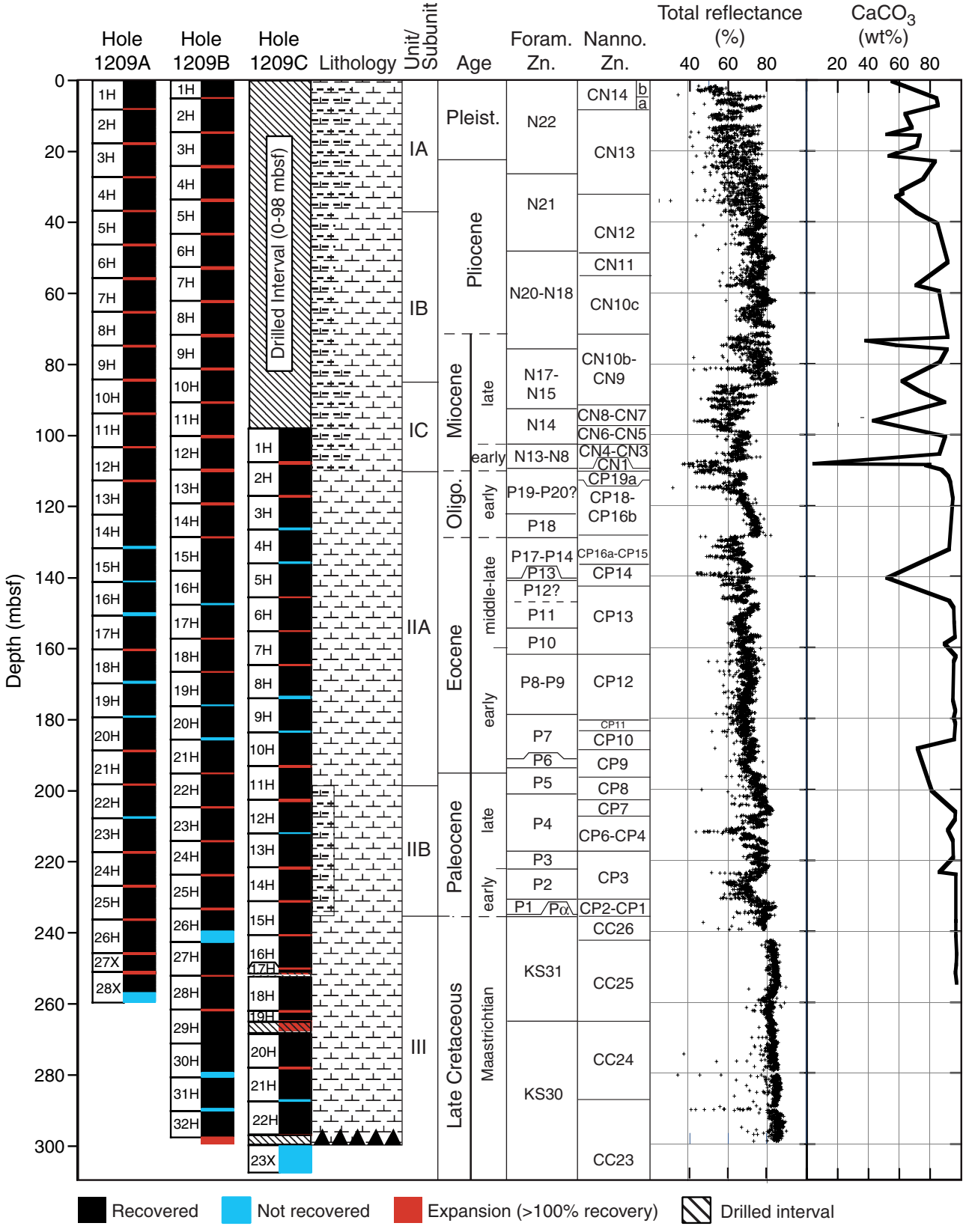

Figure F7. Magnetic susceptibility and color reflectance red/blue (680 nm/420 nm) ratio for Hole 1209B. The increase in red/blue ratios at 85 mbsf indicates a shift toward more oxic redox conditions associated with lower sedimentation rates and more oxygen-rich bottom waters. The accurate correction factor for the raw instrument magnetic susceptibility values is 0.68×10^{-5}.

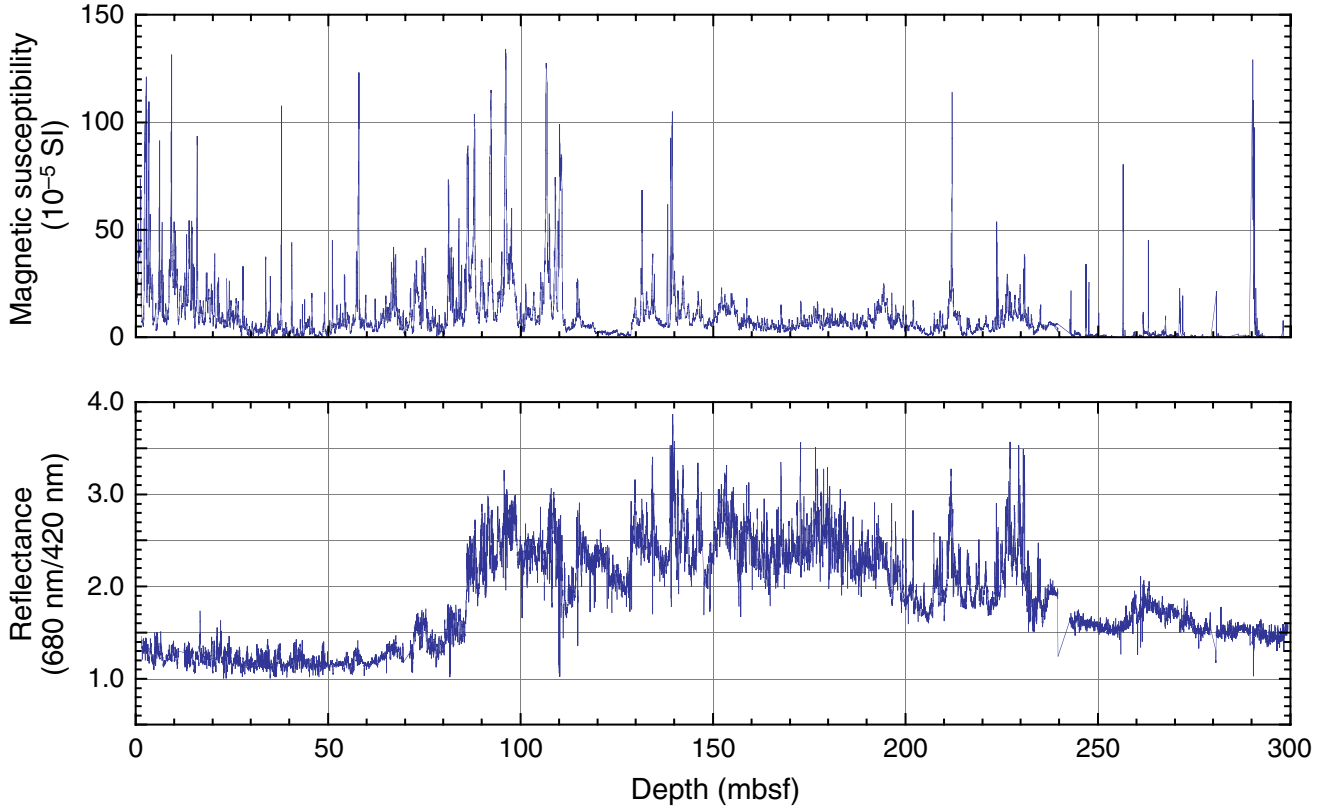

Figure F8. Estimates of biosiliceous material from Hole 1209A smear slides.

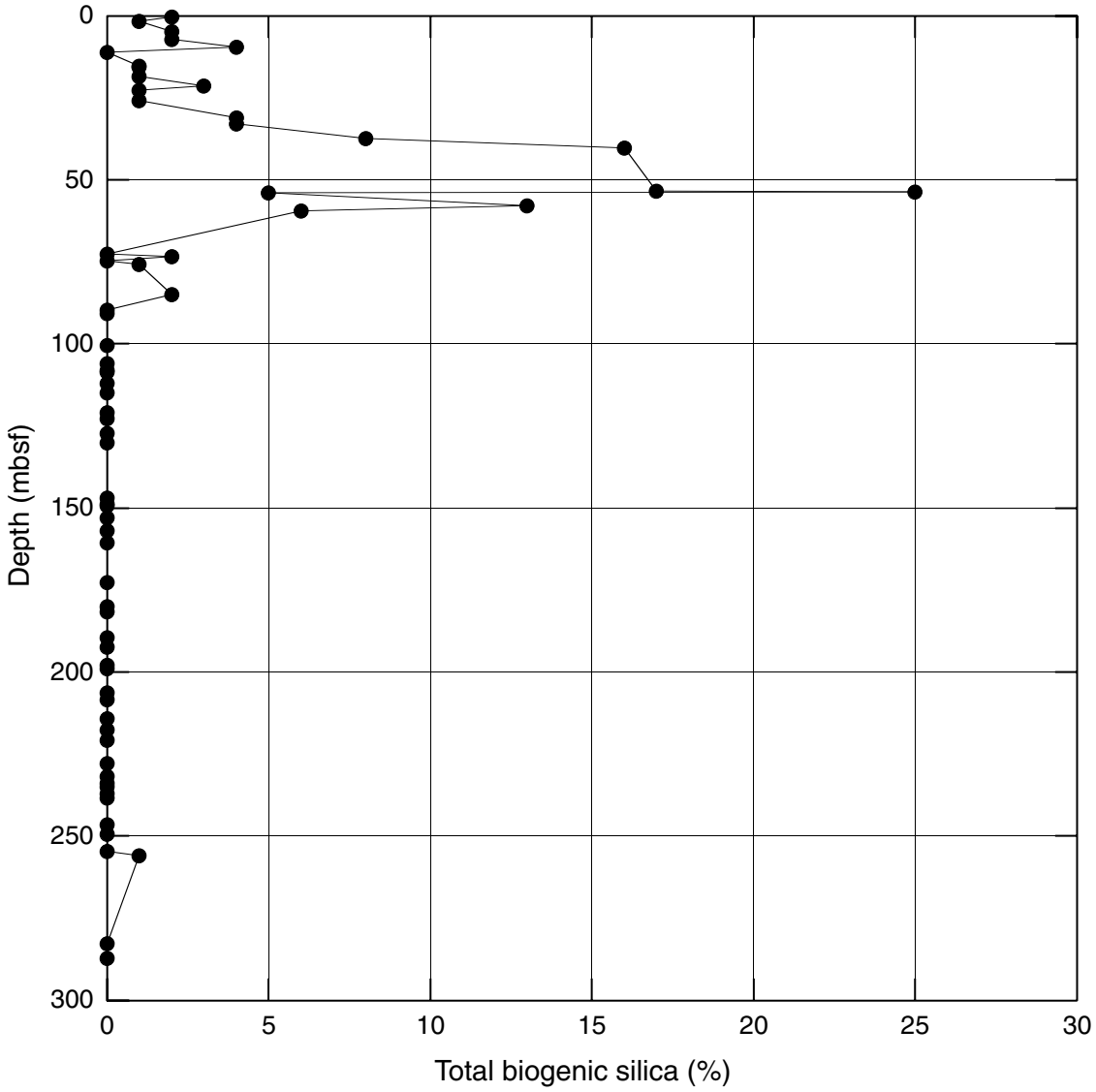

Figure F9. Composite digital photograph and color reflectance red/blue (680 nm/420 nm) ratio for Core 198-1209A-10H. The plot shows the rise in the red/blue ratio at the boundary between Subunits IA and IB. This core is late Miocene in age.

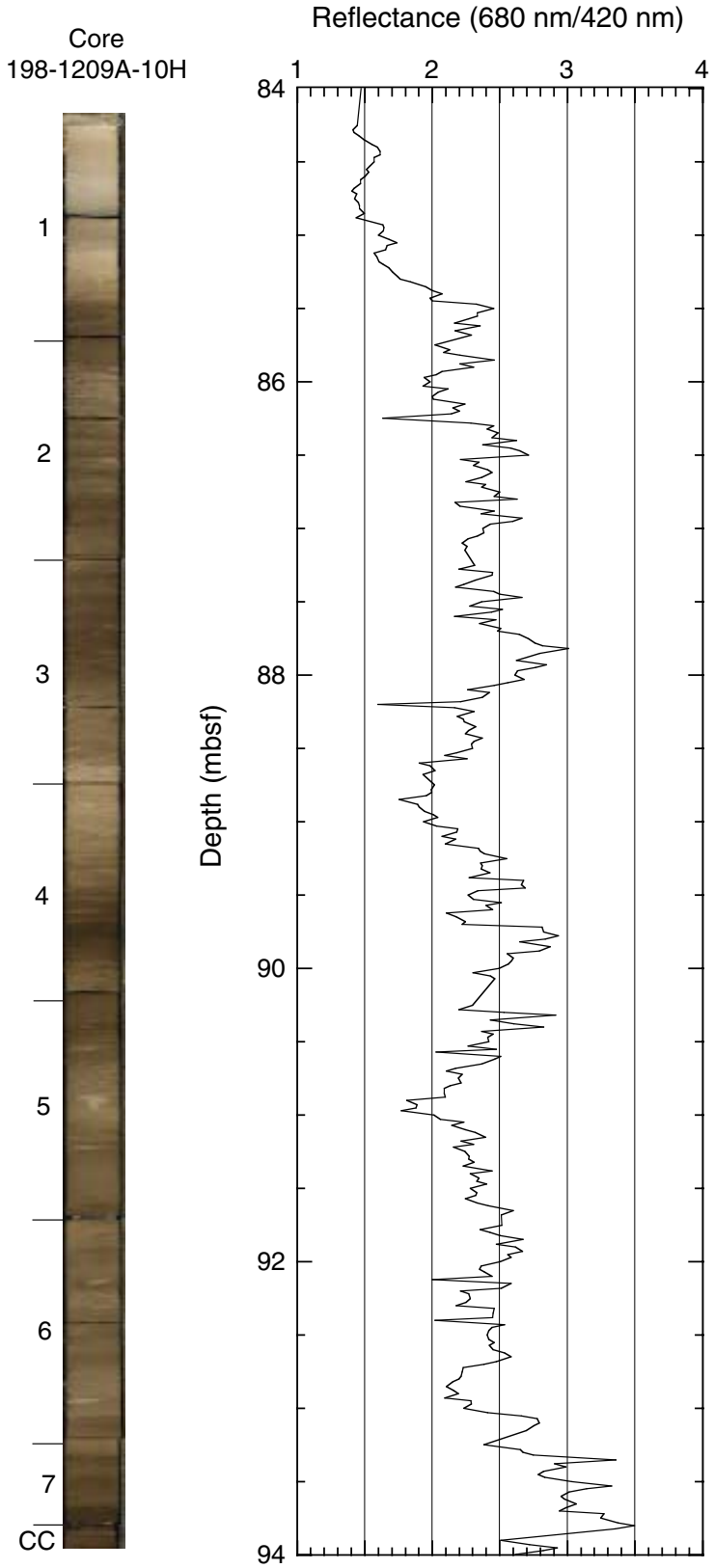

Figure F10. Composite digital photograph and color reflectance in the 550-nm channel for Core 198-1209A-14H. The Eocene/Oligocene boundary lies between 127 and 128 mbsf.

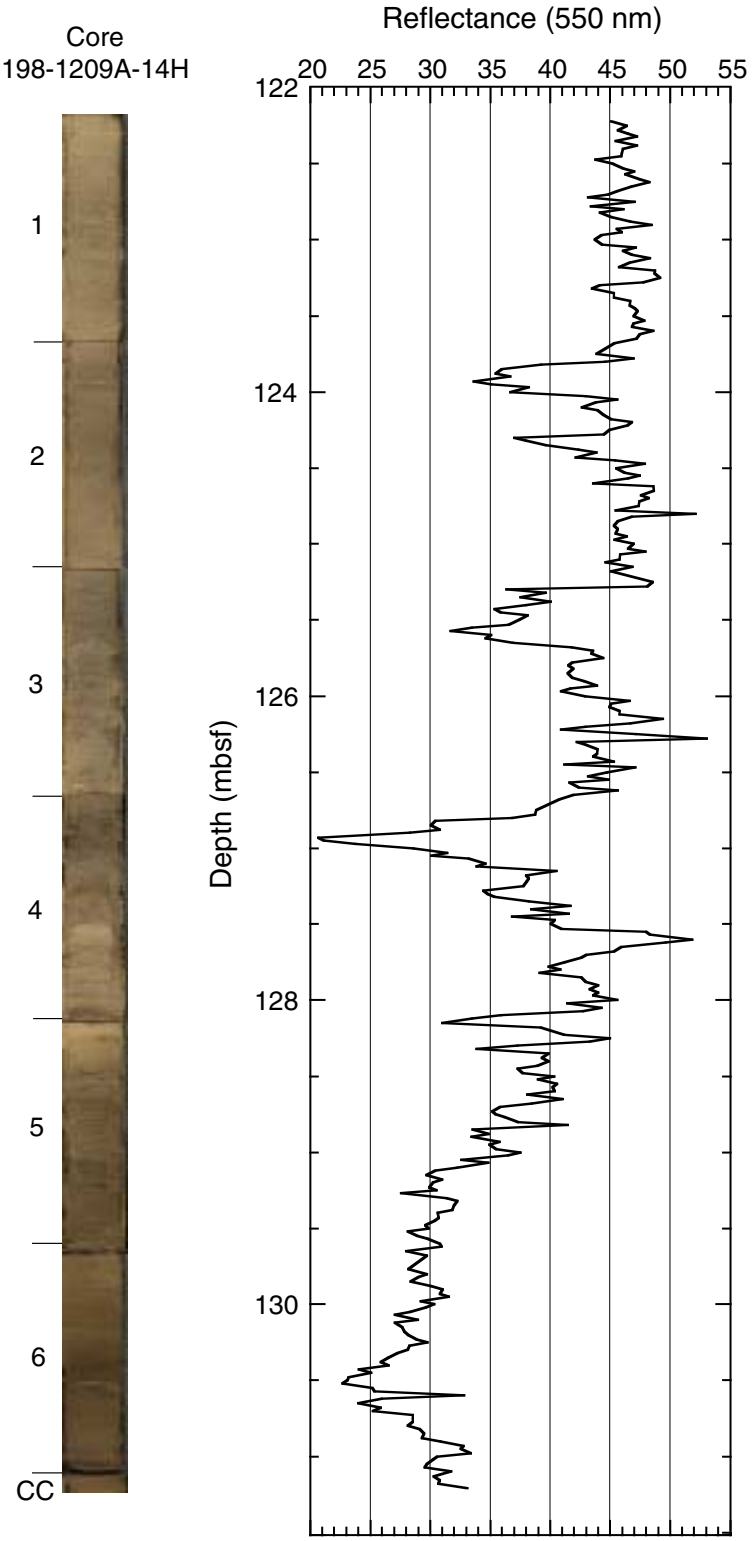

Figure F11. Composite digital photograph, color reflectance, and bulk density for Core 198-1209A-21H. The Paleocene/Eocene boundary lies at the base of the negative excursion in reflectance at 198 mbsf. PETM = Paleocene–Eocene Thermal Maximum.

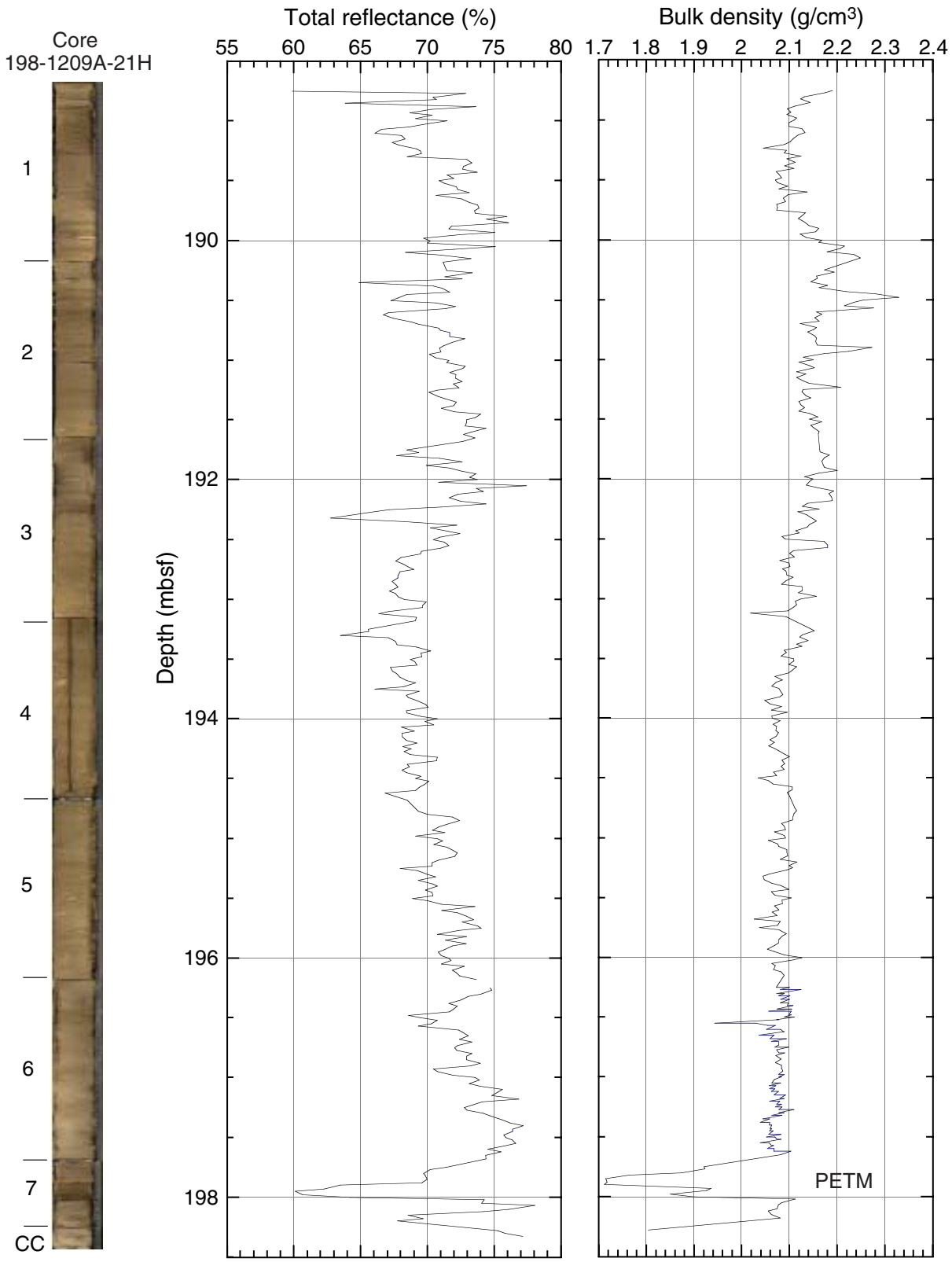

Figure F12. Close-up photograph of the contact between clay-poor and clay-rich sediment at the top of the Paleocene (interval 198-1209B-22H-1, 120–140 cm).

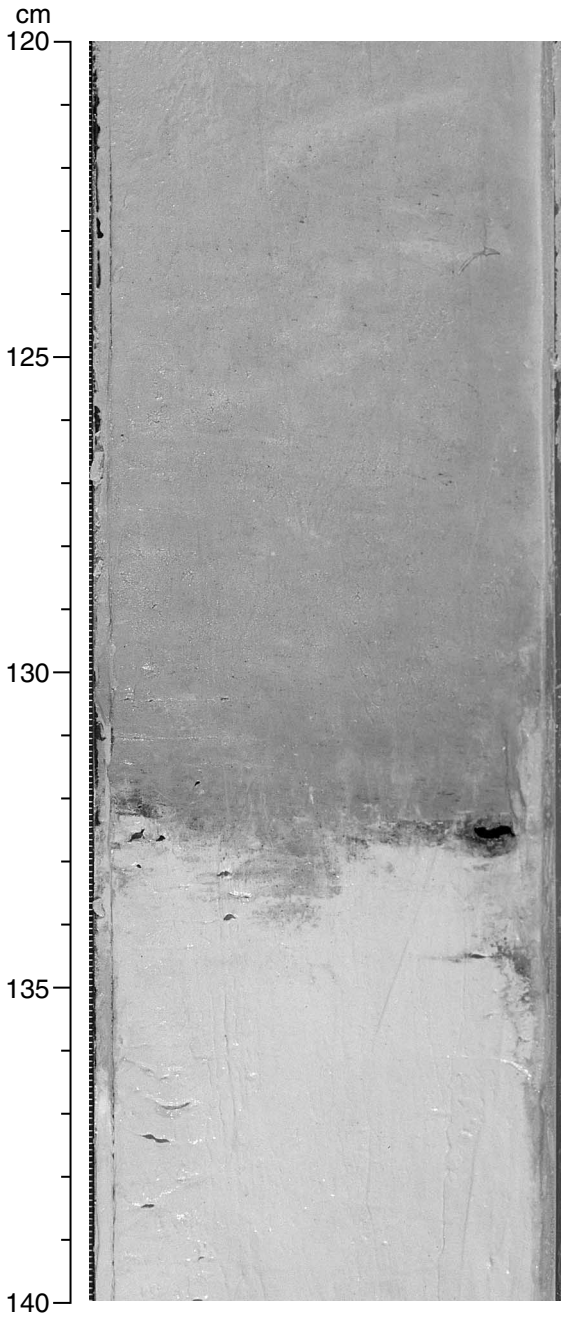

Figure F13. Smear slide photomicrograph showing needles of inorganic calcite dispersed within nannofossil ooze (Sample 198-1209A-21H-7, 25–26 cm). In this view, nicols are crossed.

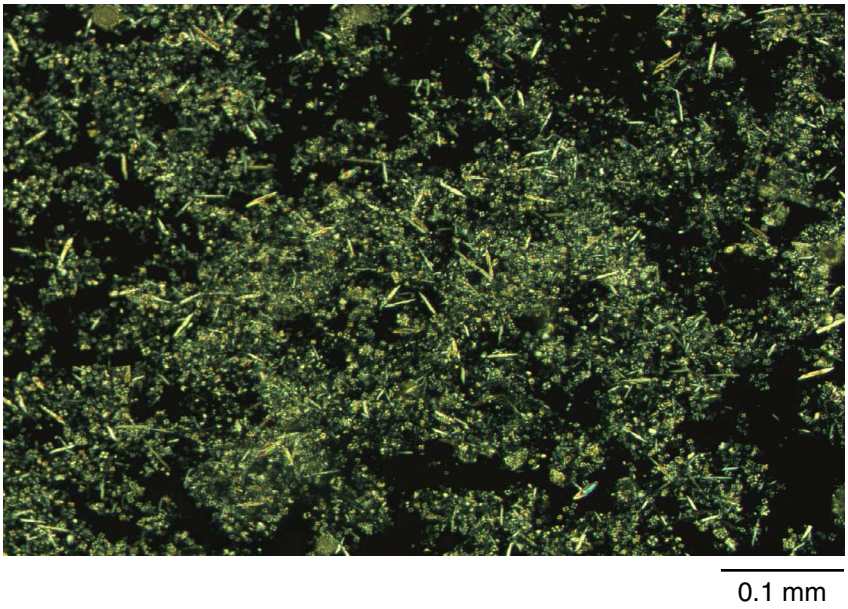

Figure F14. Composite digital photograph, color reflectance, and bulk density for Core 198-1209A-25H. The Cretaceous/Tertiary (K/T) boundary lies at the base of the negative excursion in reflectance at 235.2 mbsf.

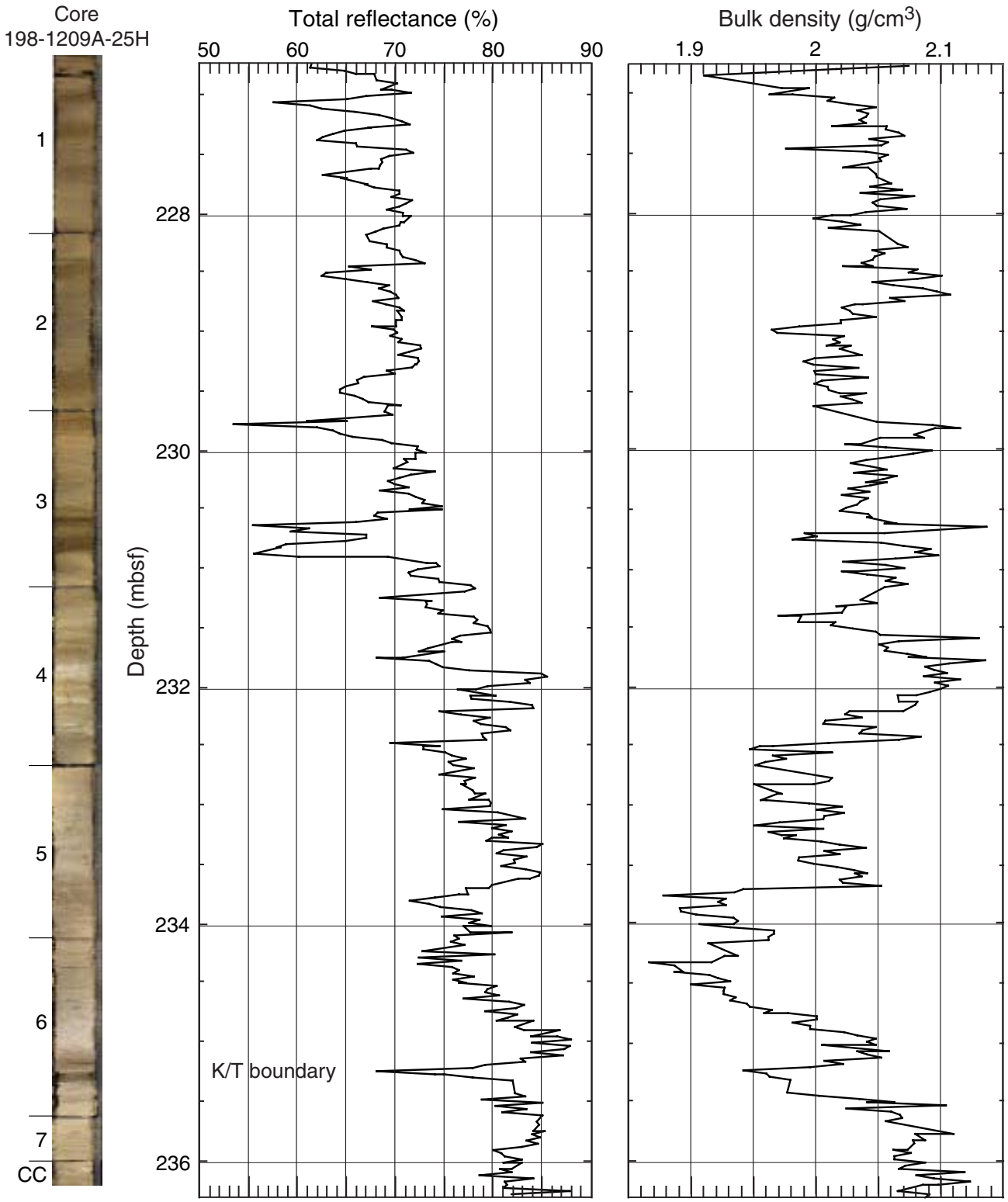

Figure F15. Total reflectance and magnetic susceptibility for the interval 175 to 185 mbsf (middle Eocene). With sedimentation rates averaging 5.2 m/m.y. through this interval, the mean cycle wavelength is roughly 50–60 cm and would correspond to a period of roughly 100 k.y. The accurate correction factor for the raw instrument magnetic susceptibility values is 0.68×10^{-5}.

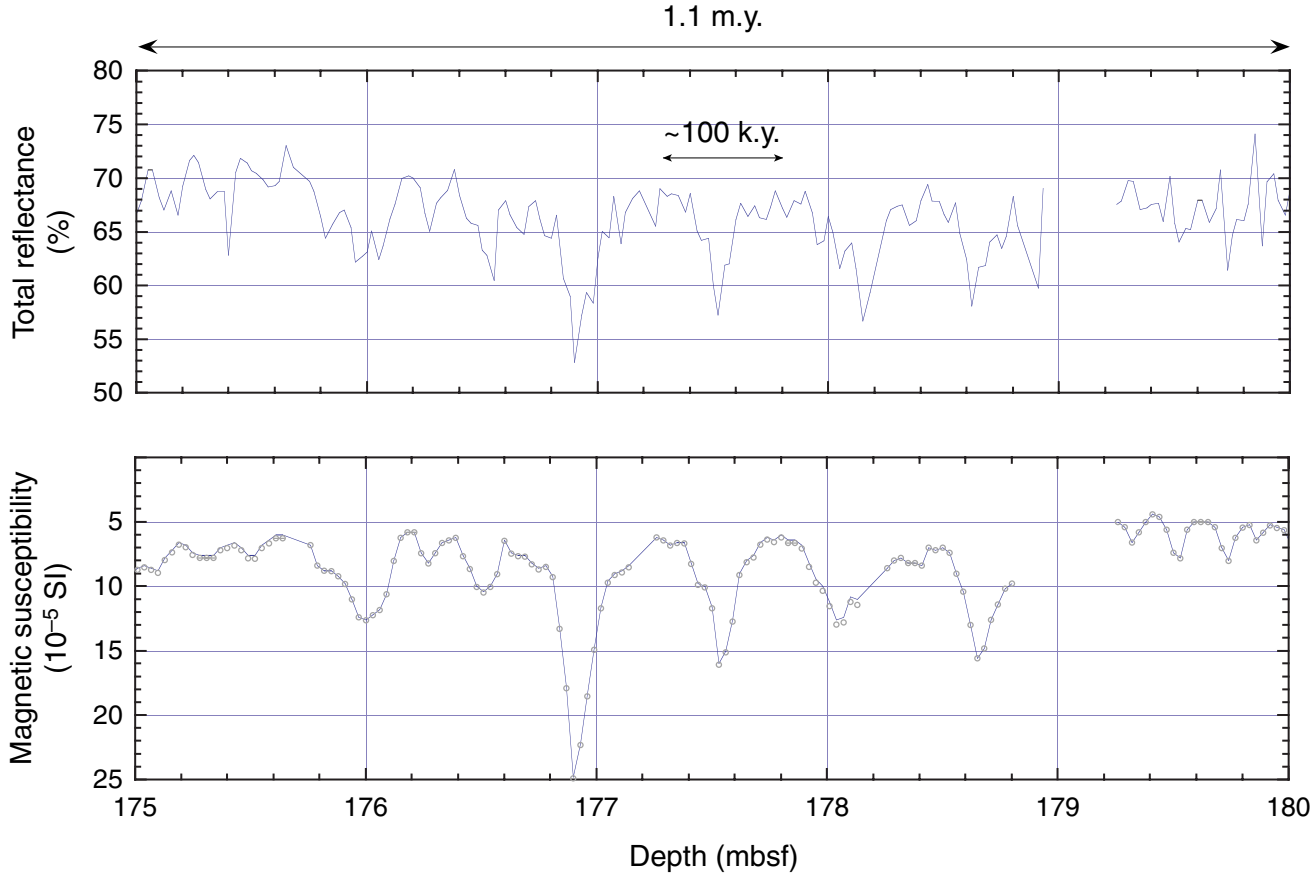

Figure F16. Hole 1209A archive-half magnetization intensities after AF demagnetization at peak fields of 20 mT as measured with the shipboard pass-through magnetometer plotted in meters composite depth (mcd). Solid blue triangles = measurements from Hole 1209A, solid green circles = measurements from Hole 1209B, open red circles = measurements from Hole 1209C.

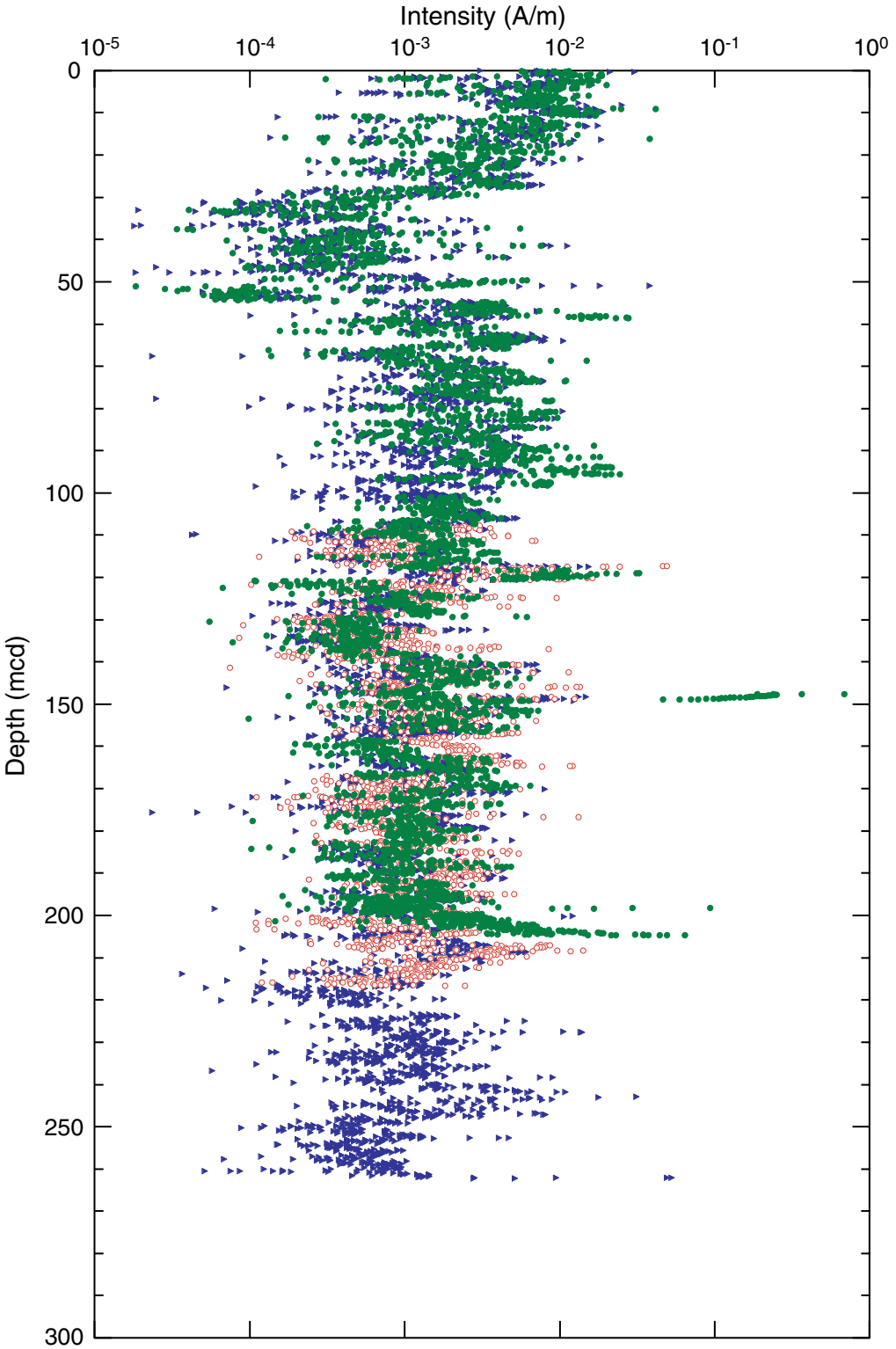

Figure F17. Inclination after AF demagnetization at peak fields of 20 mT as measured with the shipboard pass-through magnetometer for the upper 100 mcd at Holes 1209A and 1209B. The column at center shows interpreted zones of normal (black) and reversed (white) polarity. Gray intervals indicate zones in which polarity is uncertain.

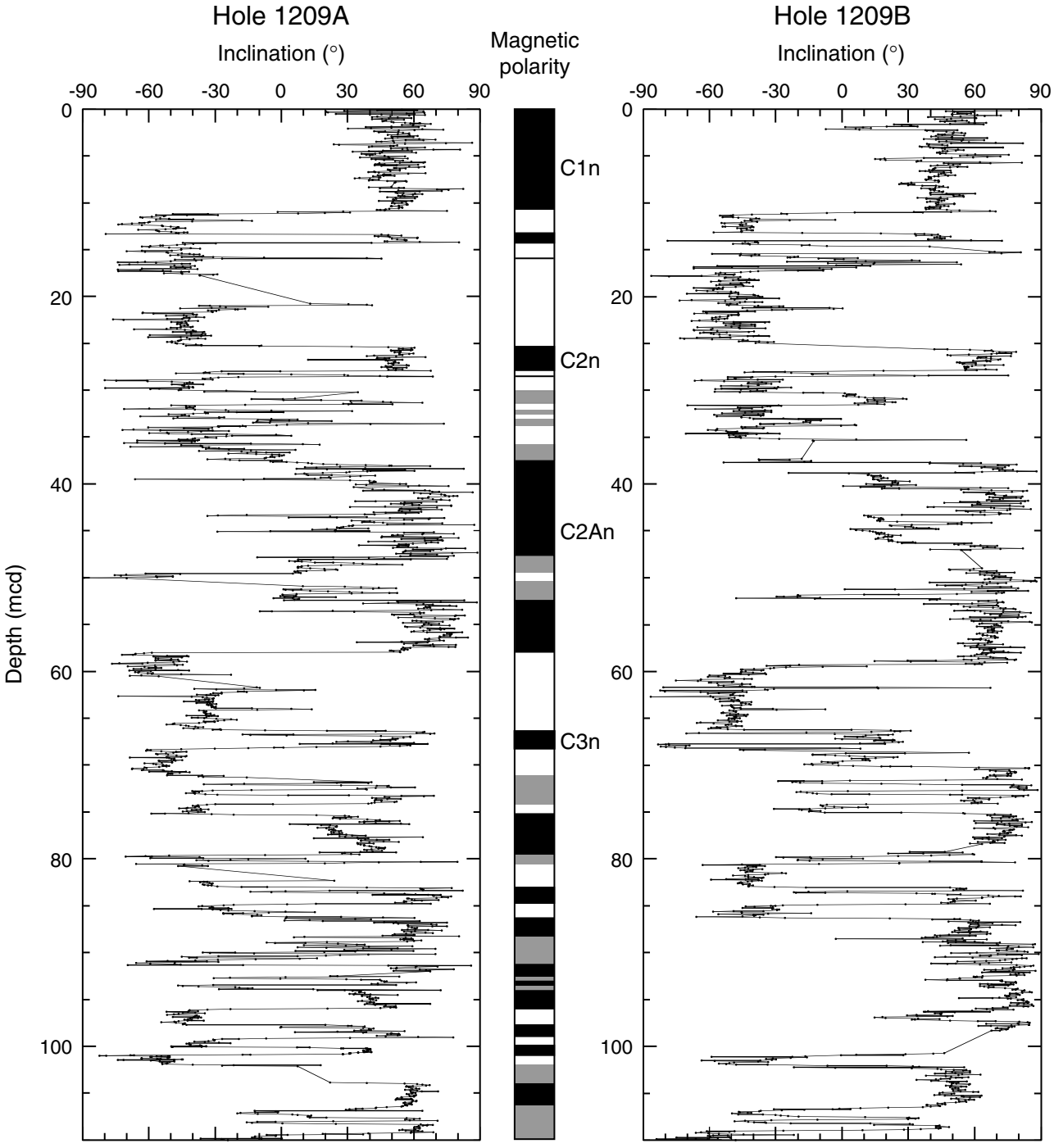

Figure F18. Age-depth curve for Site 1209 derived from the magnetic stratigraphy shown in Fig. F17, p. 53, using the geomagnetic polarity timescale of Cande and Kent (1995). The average sedimentation rate is also plotted.

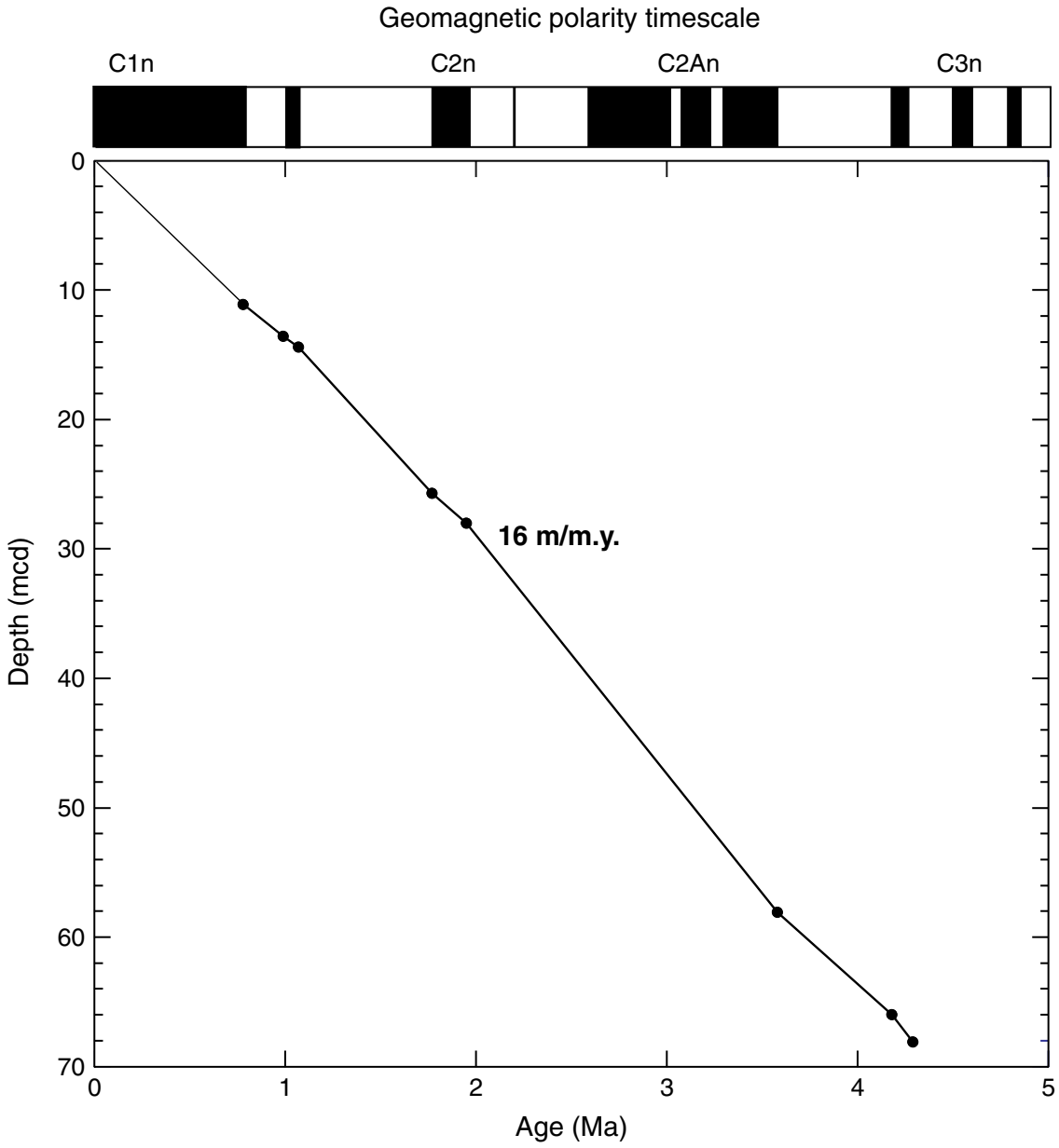

Figure F19. A. Magnetic susceptibility data for 0 to 260 mcd for Site 1209. Holes 1209B and 1209C are offset from Hole 1209A by a constant (40×10^{-6} and 80×10^{-6}, respectively). The accurate correction factor for these raw instrument values is 0.68×10^{-5}. **B.** GRA bulk density data for 0 to 260 mcd for Site 1209. Holes 1209B and 1209C are offset from Hole 1209A by a constant (0.3 and 0.6 g/cm^3, respectively).

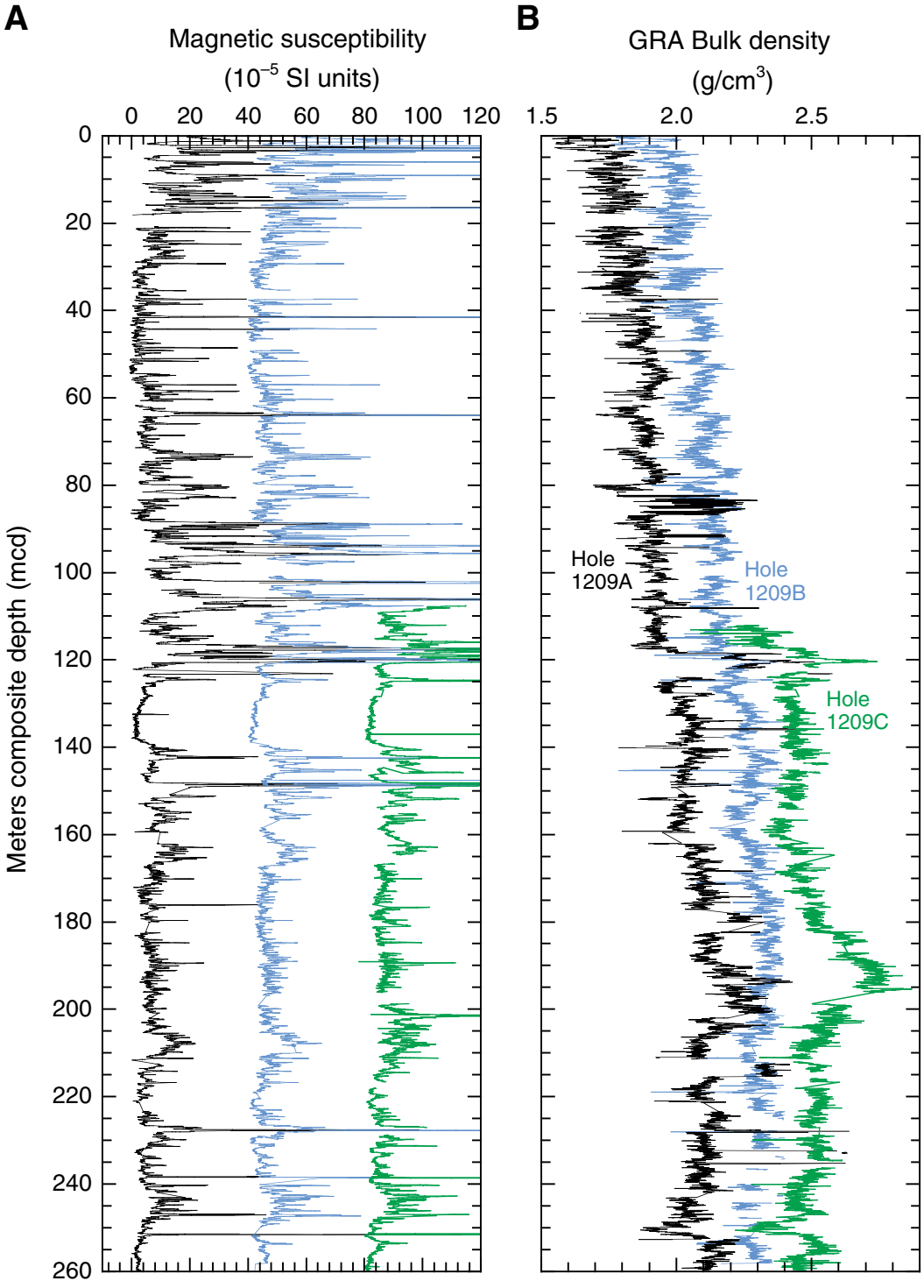

Figure F20. Magnetic susceptibility data for 135 to 157 mcd for Site 1209. This interval includes the middle Eocene and the Eocene/Oligocene (E/O) boundary interval.The accurate correction factor for these raw instrument values is 0.68×10^{-5}.

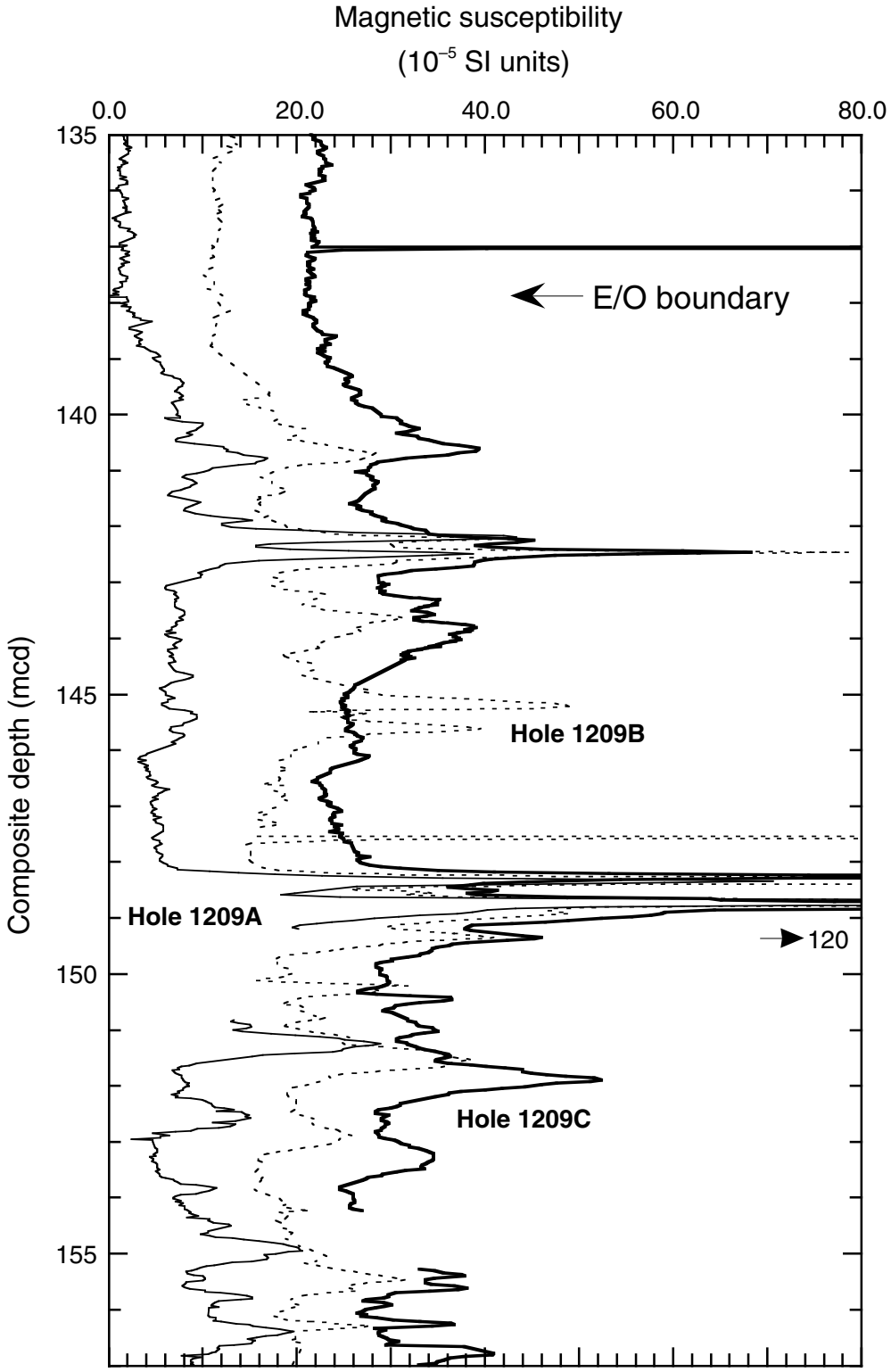

Figure F21. Magnetic susceptibility data for 202 to 217 mcd for Site 1209. This interval includes the Paleocene/Eocene boundary (Paleocene–Eocene Thermal Maximum [PETM]). The accurate correction factor for these raw instrument values is 0.68×10^{-5}.

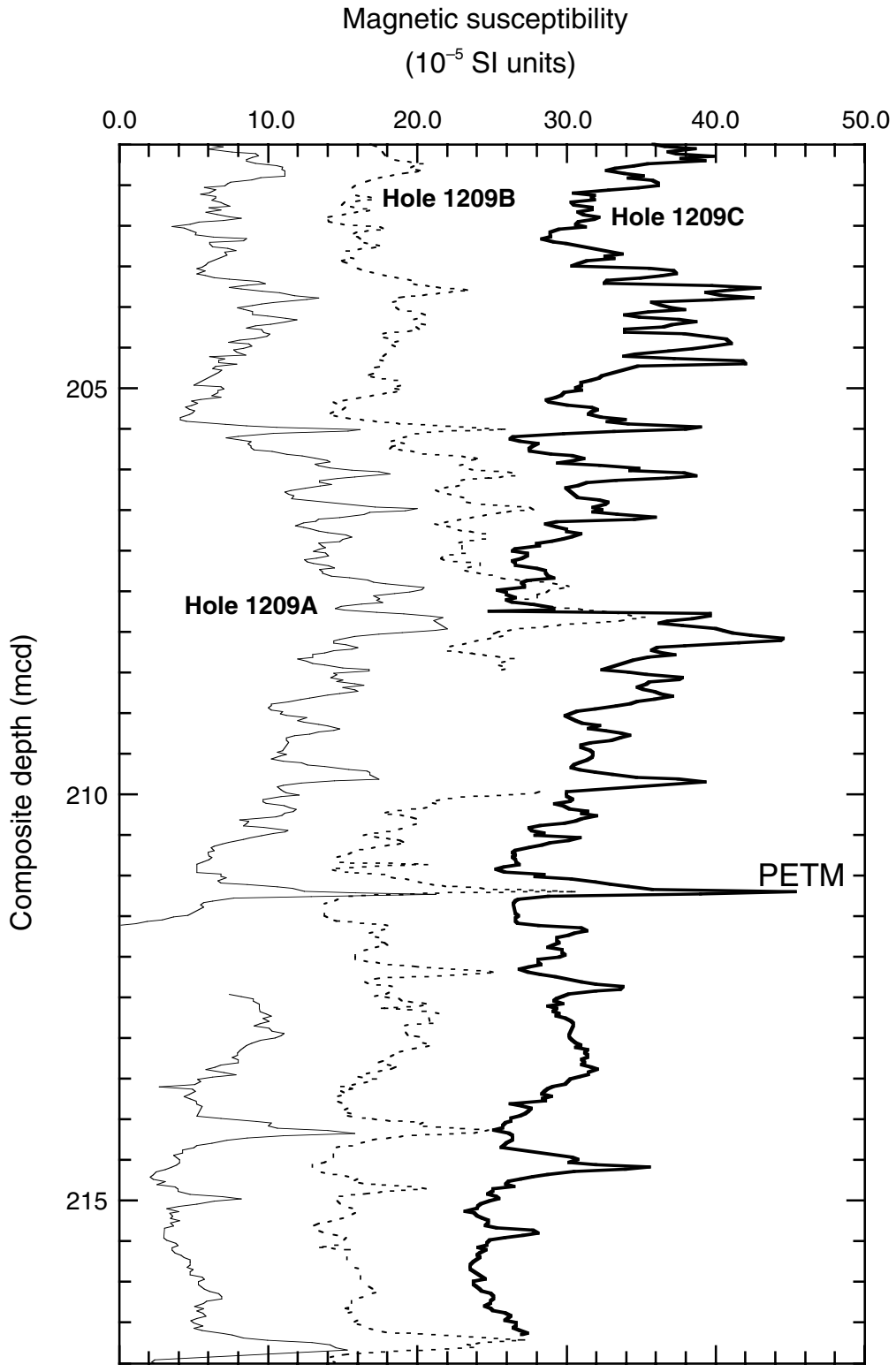

Figure F22. Age-depth plot of calcareous nannofossil (diamonds) and planktonic foraminiferal (crosses) datums at Site 1209. Datum ages and depths are presented in Tables T2, p. 83, and T3, p. 84.

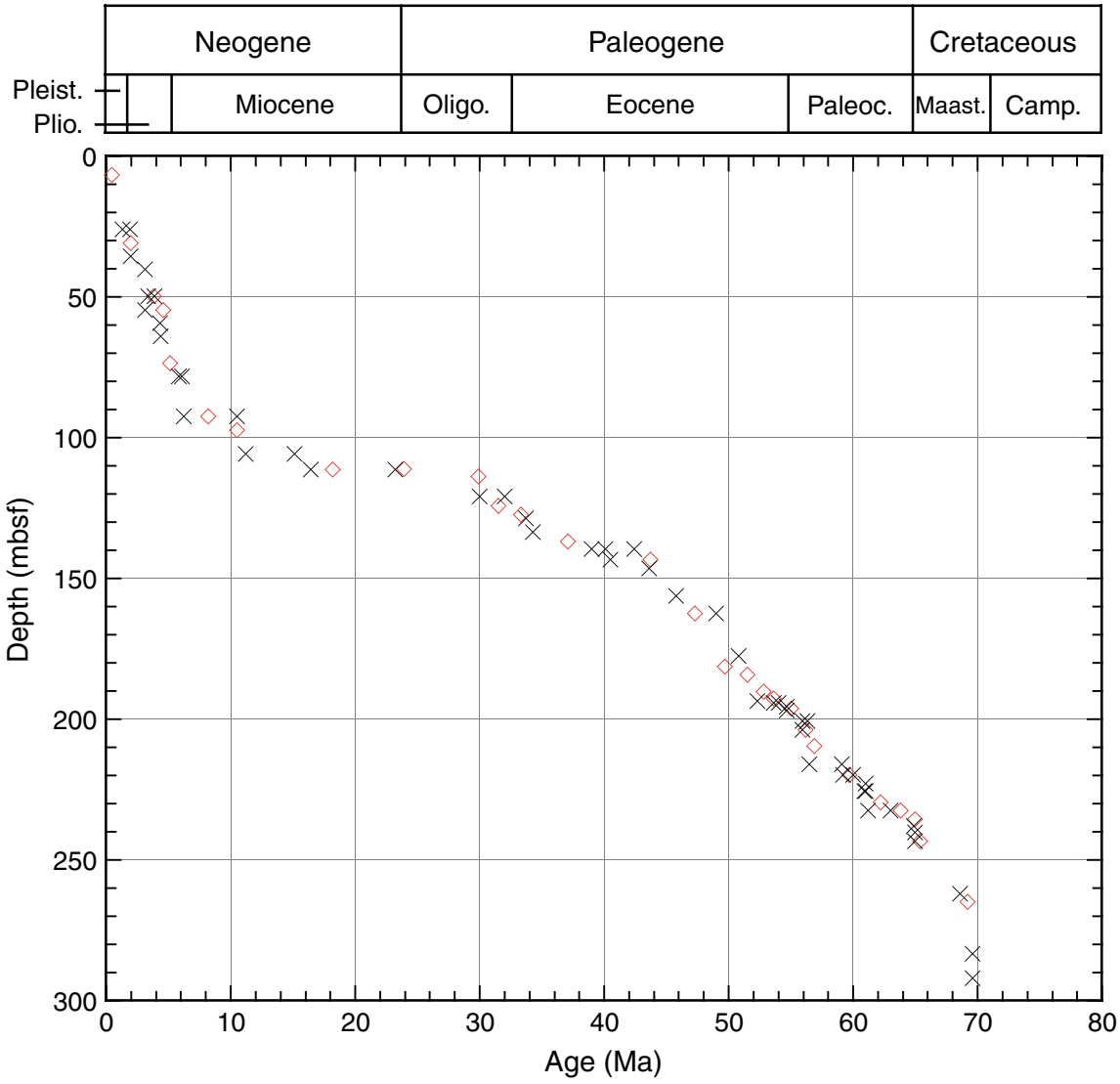

Figure F23. Age-depth plot of Neogene calcareous nannofossil (diamonds) and planktonic foraminiferal (crosses) datums at Site 1209. Alternative interpretations are presented: continuous sedimentation through the Miocene is indicated by calcareous nannofossil data, whereas planktonic foraminiferal data suggest discontinuous sedimentation. Datum ages and depths are presented in Tables T2, p. 83, and T3, p. 84. FO = first occurrence, LO = last occurrence.

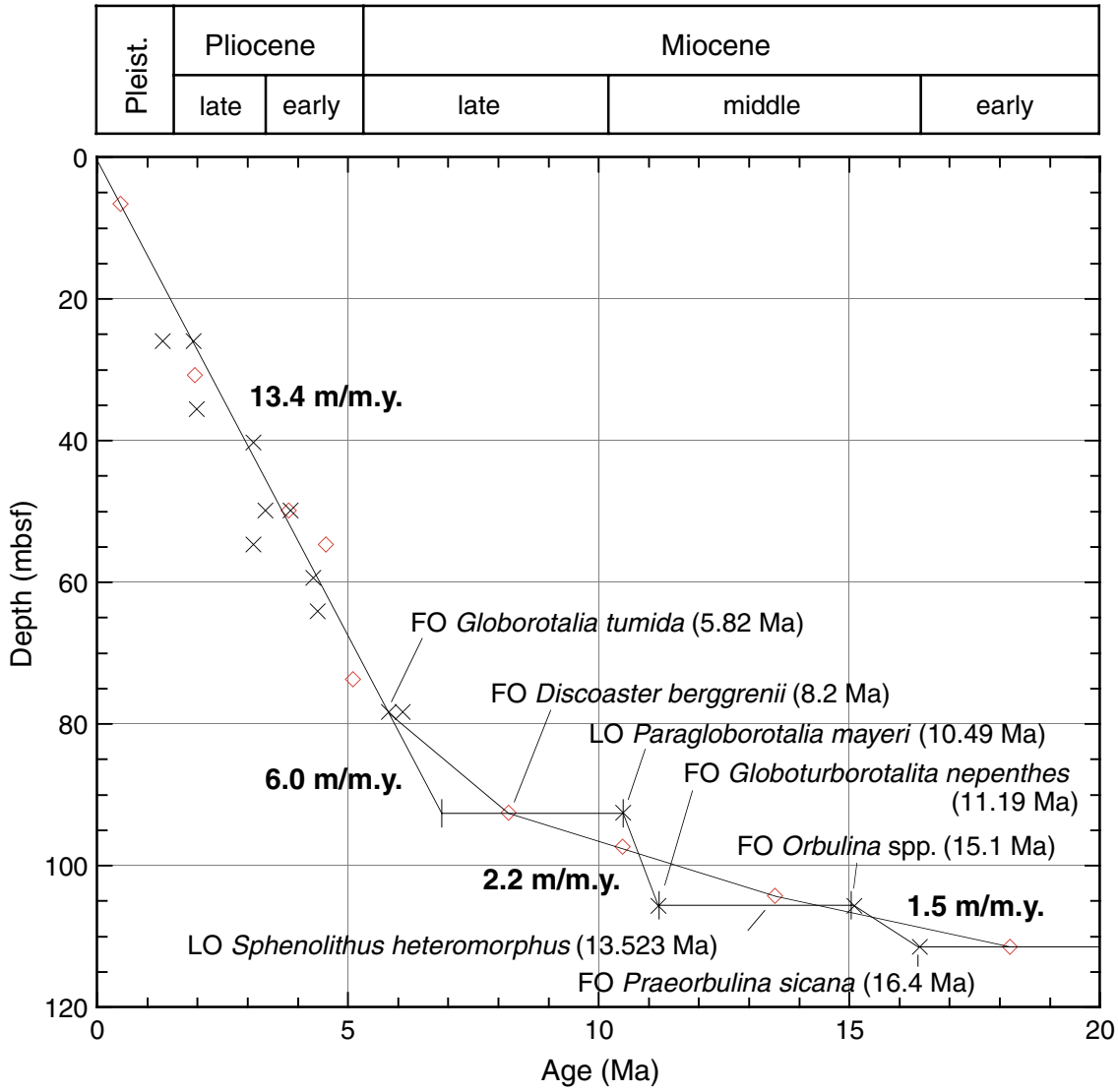

Figure F24. Age-depth plot of early Miocene–late Eocene calcareous nannofossil (diamonds) and planktonic foraminiferal (crosses) datums at Site 1209. Datum ages and depths are presented in Tables T2, p. 83, and T3, p. 84. FO = first occurrence, LO = last occurrence.

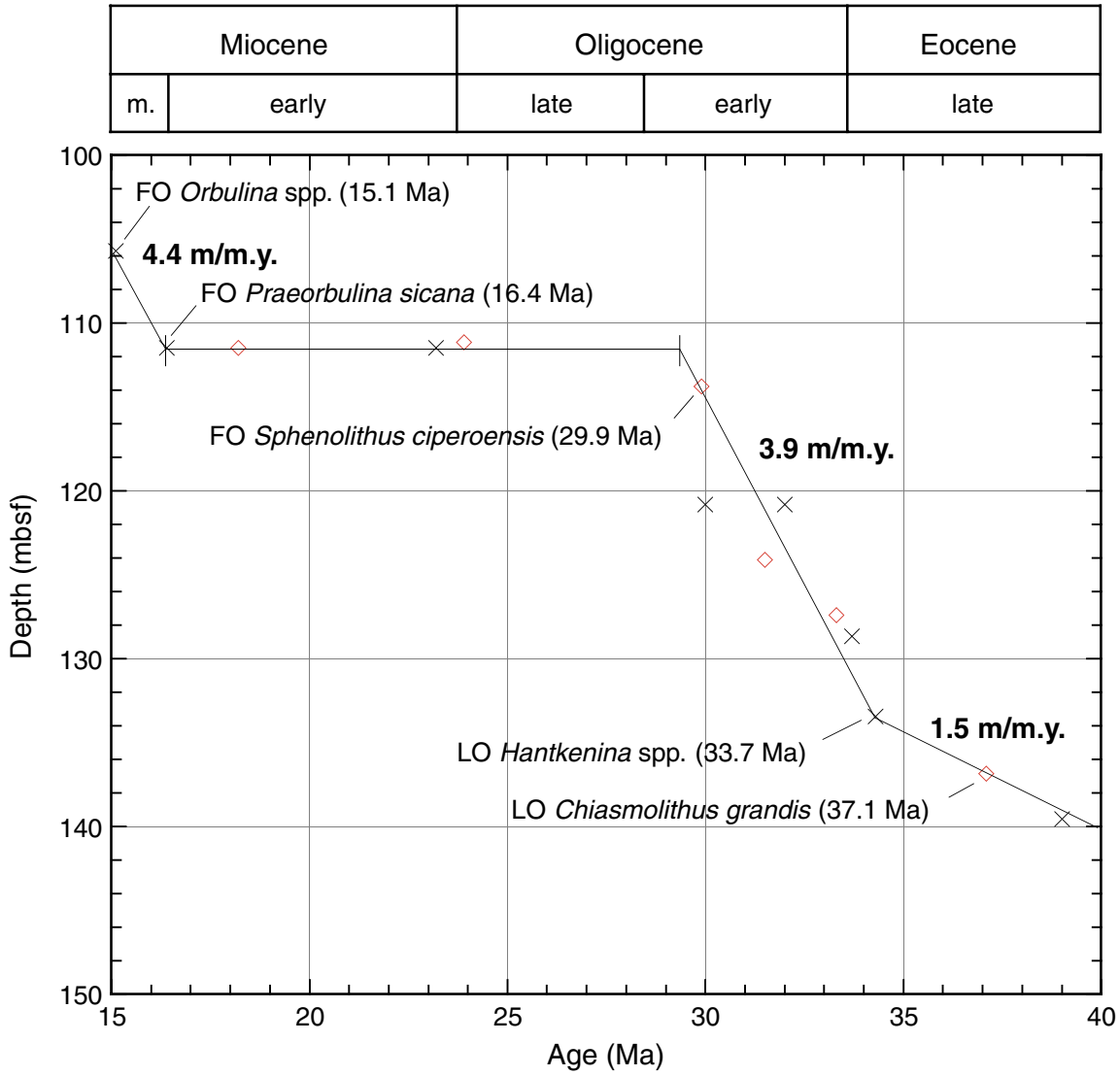

Figure F25. Age-depth plot of early Oligocene–late Paleocene calcareous nannofossil (diamonds) and planktonic foraminiferal (crosses) datums at Site 1209. Datum ages and depths are presented in Tables T2, p. 83, and T3, p. 84. FO = first occurrence, LO = last occurrence.

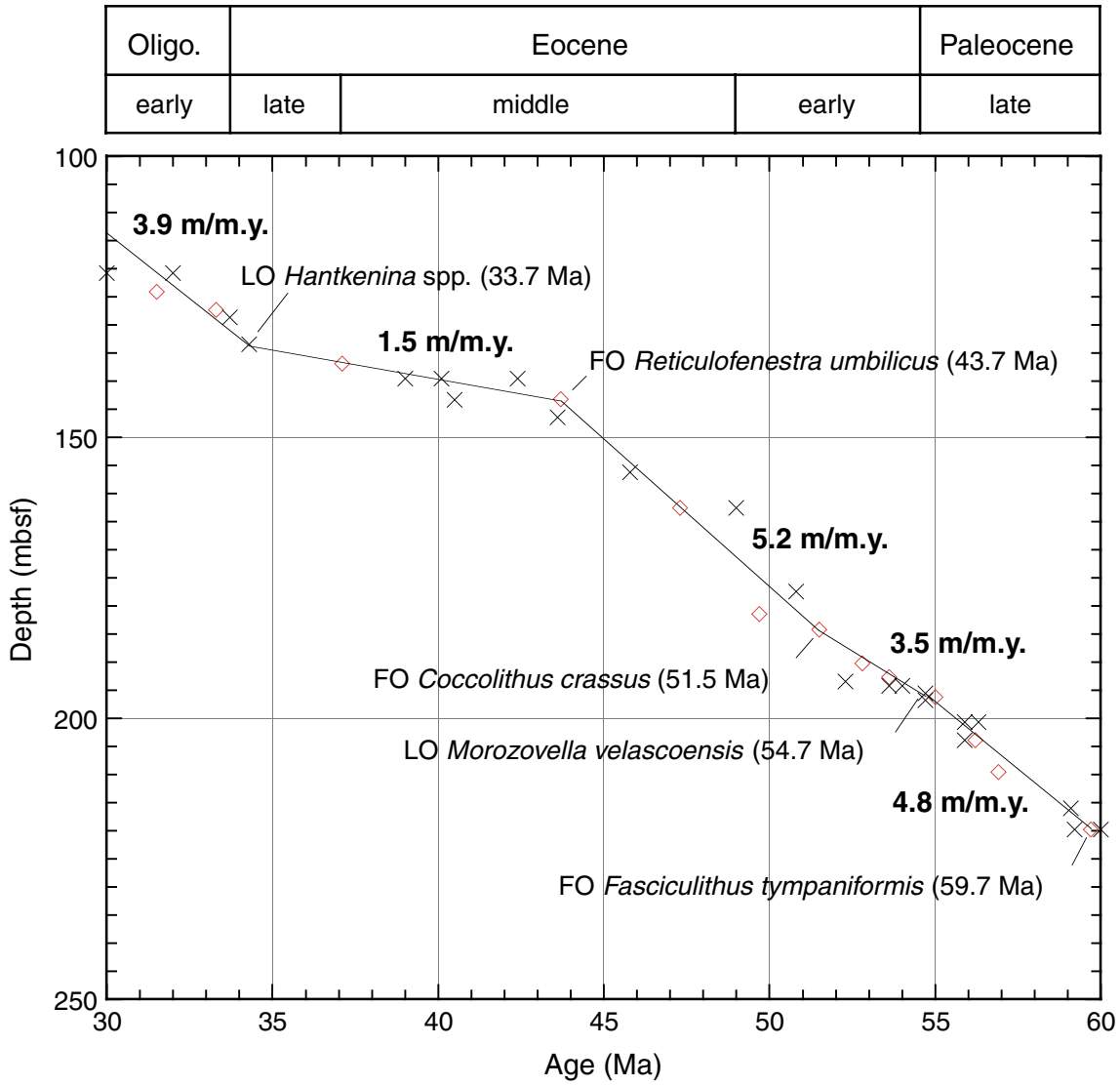

Figure F26. Age-depth plot of middle Eocene–Maastrichtian calcareous nannofossil (diamonds) and planktonic foraminiferal (crosses) datums at Site 1209. Datum ages and depths are presented in Tables T2, p. 83, and T3, p. 84. FO = first occurrence, LO = last occurrence.

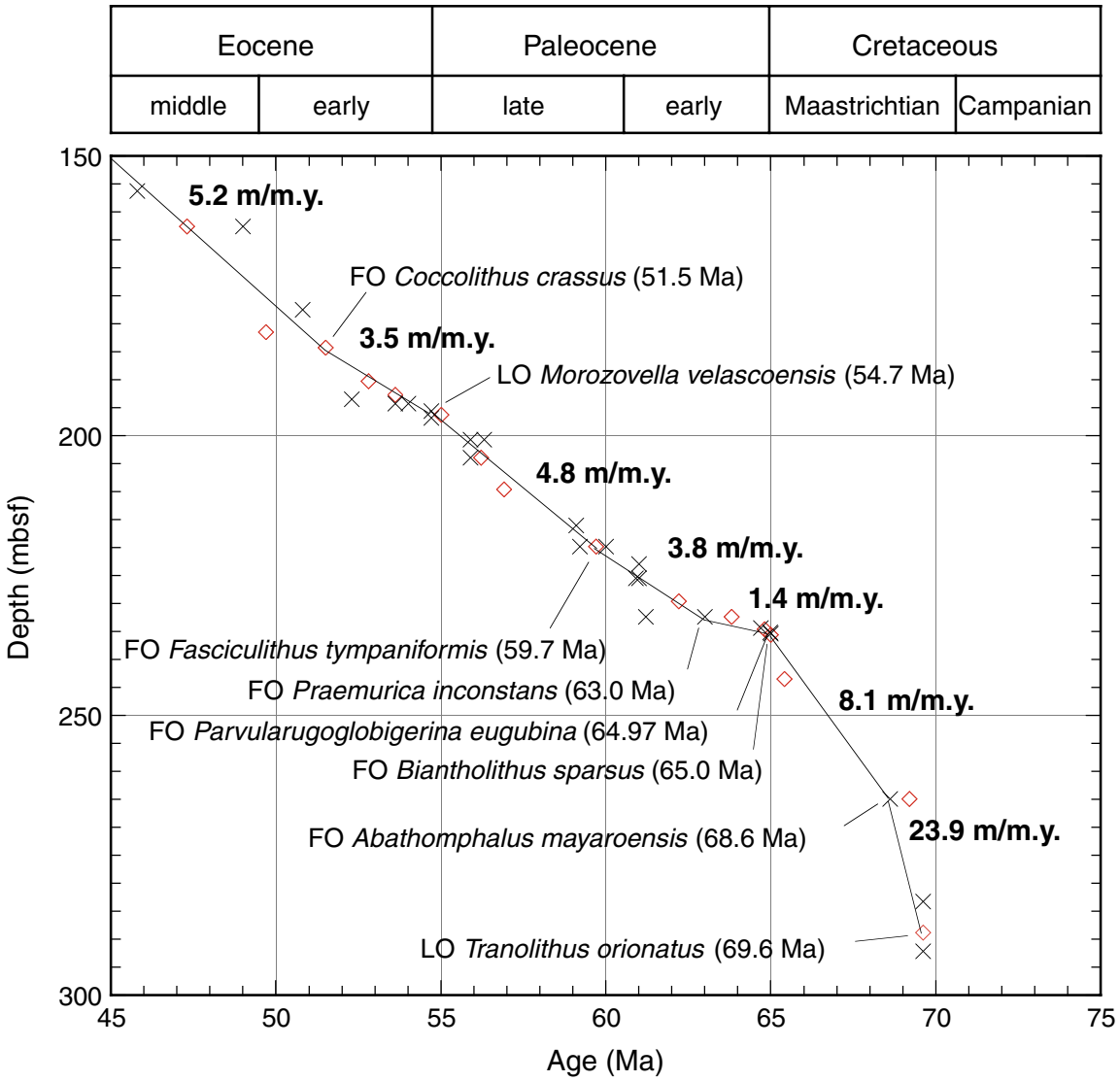

Figure F27. Mass accumulation rates for bulk sediment, carbonate fraction, and noncarbonate fraction vs. (A) depth and (B) age for the Maastrichtian–Pleistocene of Site 1209.

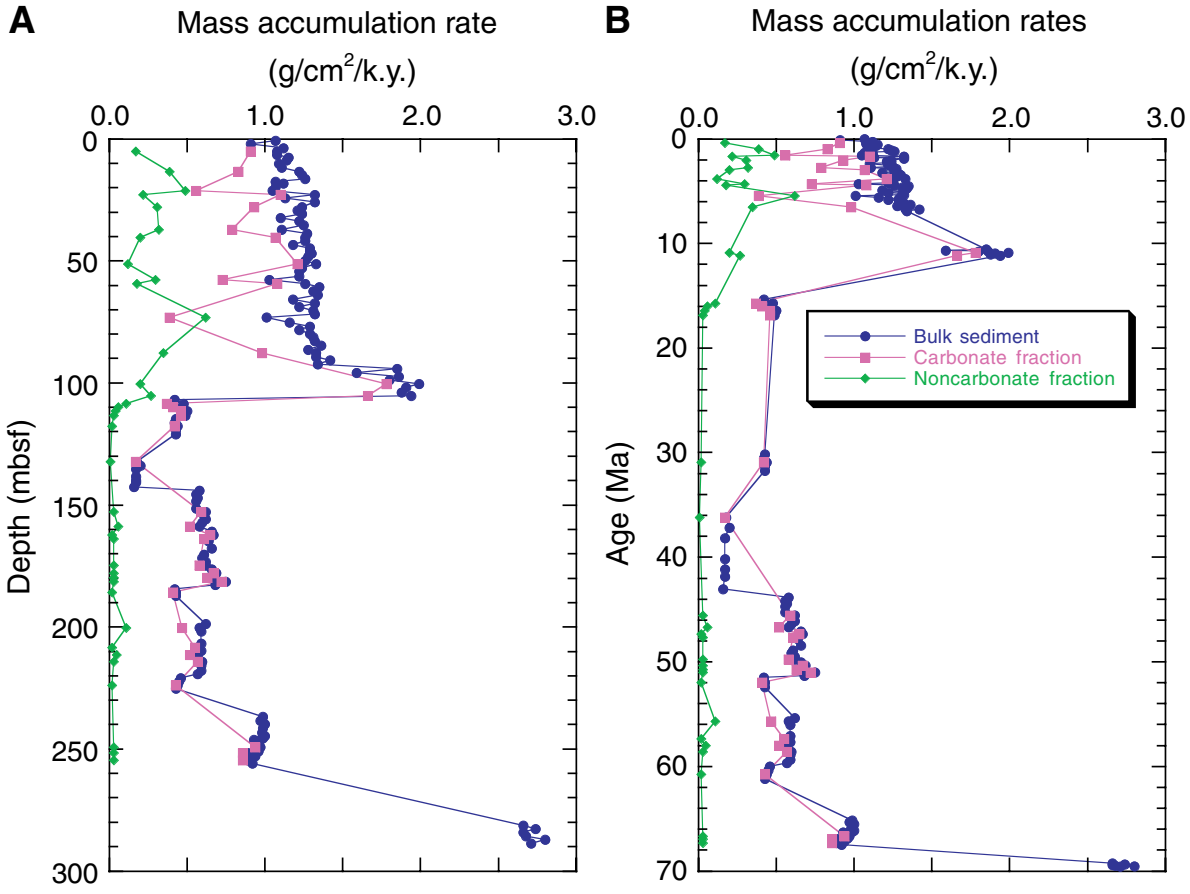

Figure F28. Downhole profiles of carbonate contents in Hole 1209A.

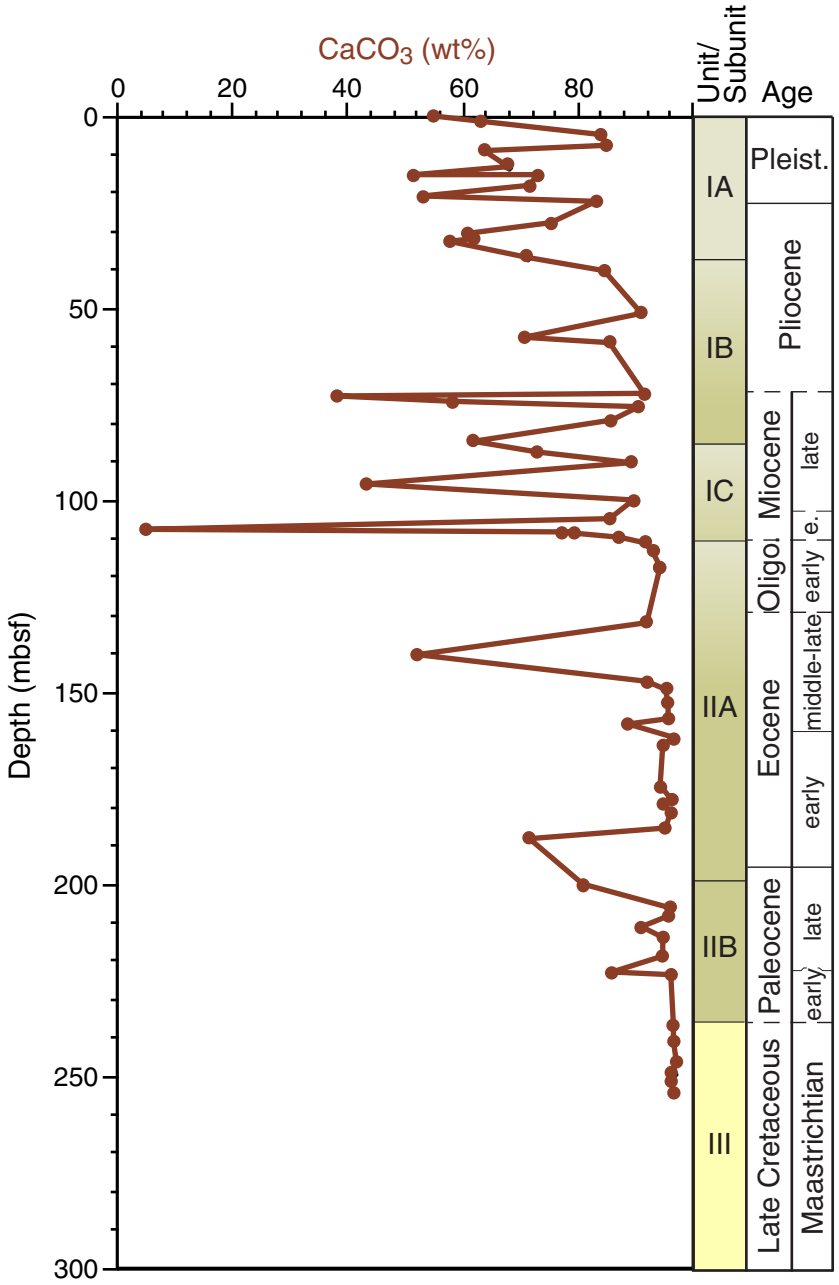

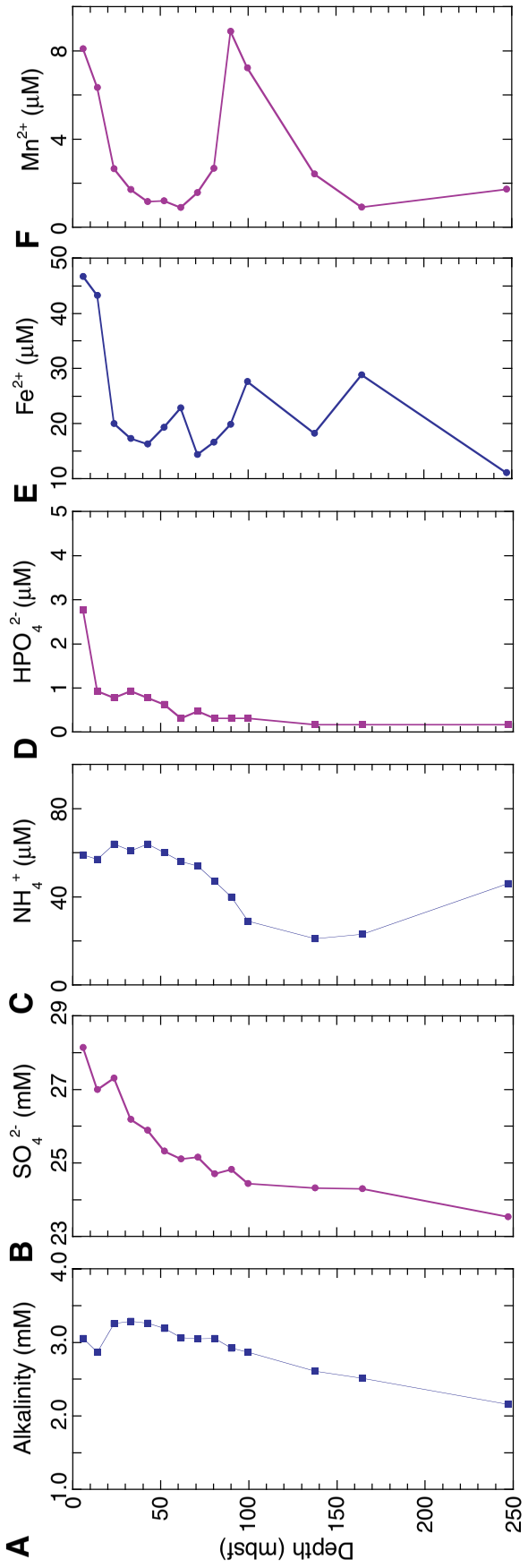

Figure F29. Interstitial water profiles for Site 1209. **A.** Alkalinity. **B.** Sulfate. **C.** Ammonium. **D.** Phosphate. **E.** Iron. **F.** Manganese.

Figure F30. Interstitial water profiles for Site 1209. **A.** Potassium. **B.** Calcium. **C.** Magnesium. **D.** Lithium. **E.** Sr and Sr/Ca.

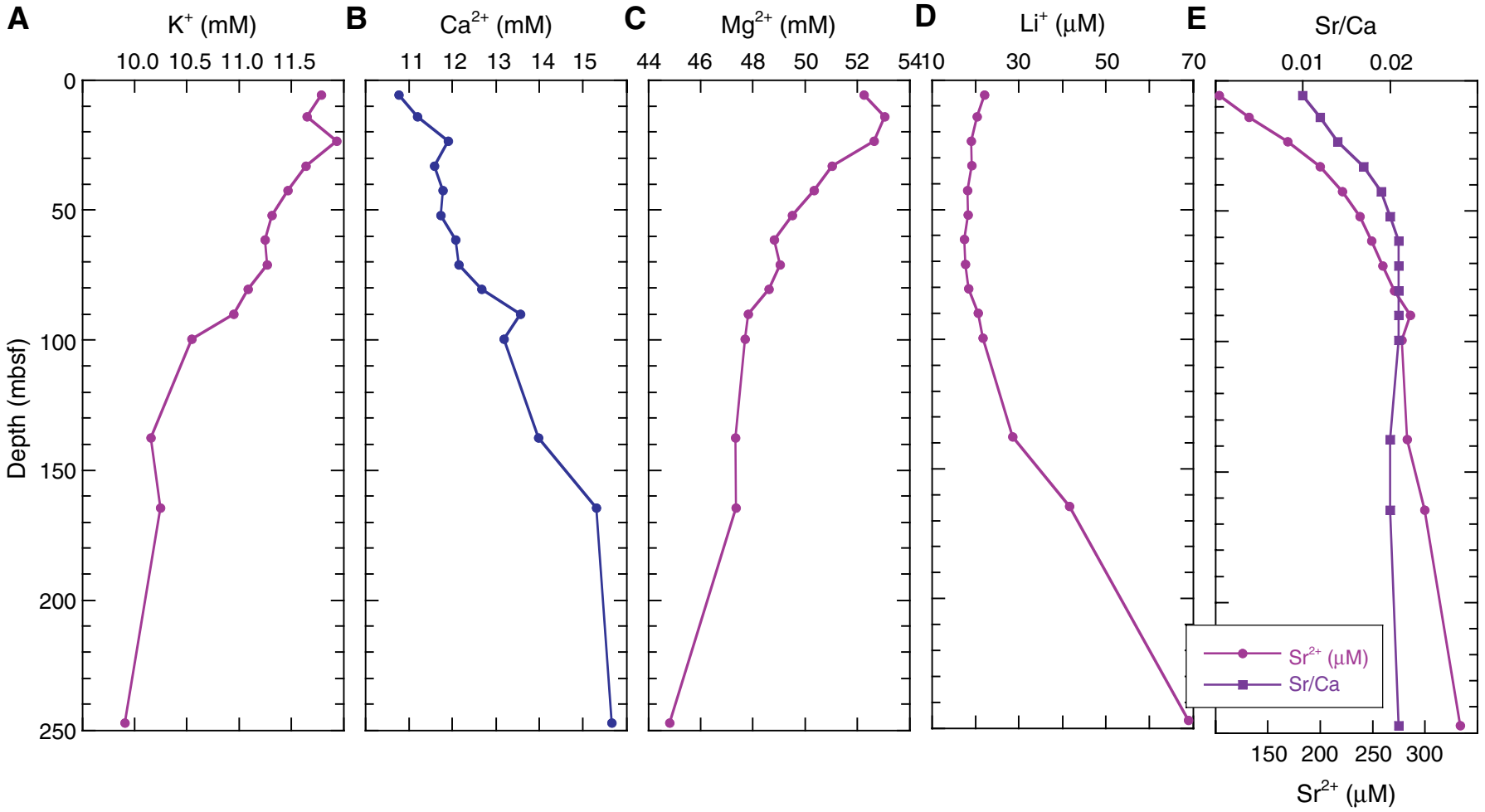

Figure F31. Silica profile for Hole 1209A.

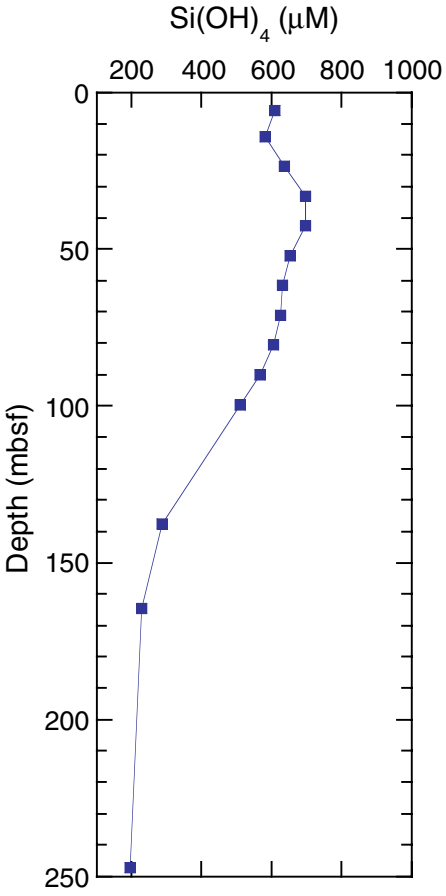

Figure F32. MST magnetic susceptibility measured in whole cores from Holes 1209A, 1209B, and 1209C plotted vs. depth. The accurate correction factor for these raw instrument values is 0.68×10^{-5}.

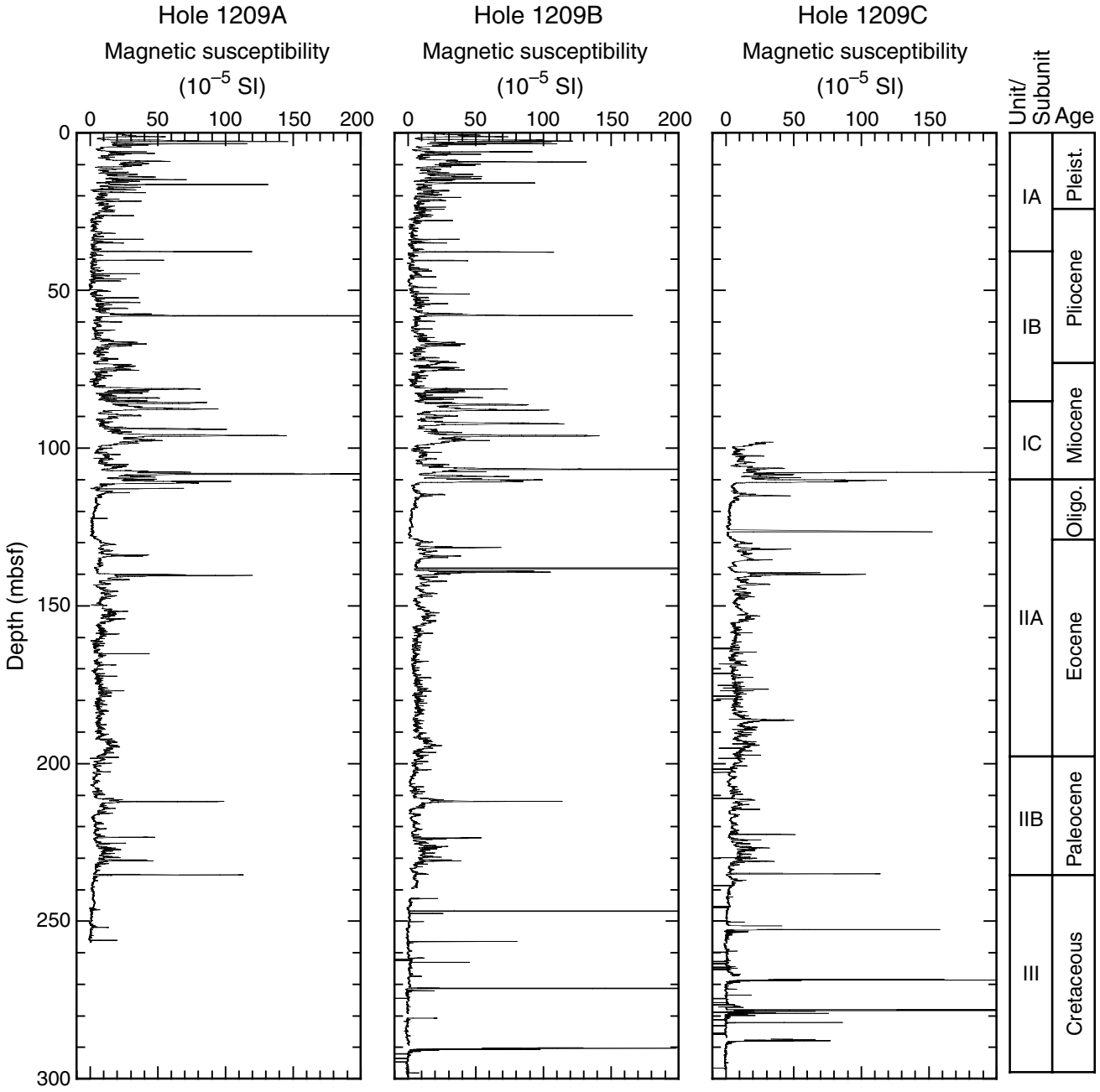

Figure F33. MST GRA bulk density (lines) measured in whole cores from Holes 1209A, 1209B, and 1209C plotted vs. depth. Discrete measurements of wet bulk density (see Table **T12,** p. 95) from Hole 1209A (solid circles) are plotted for comparison.

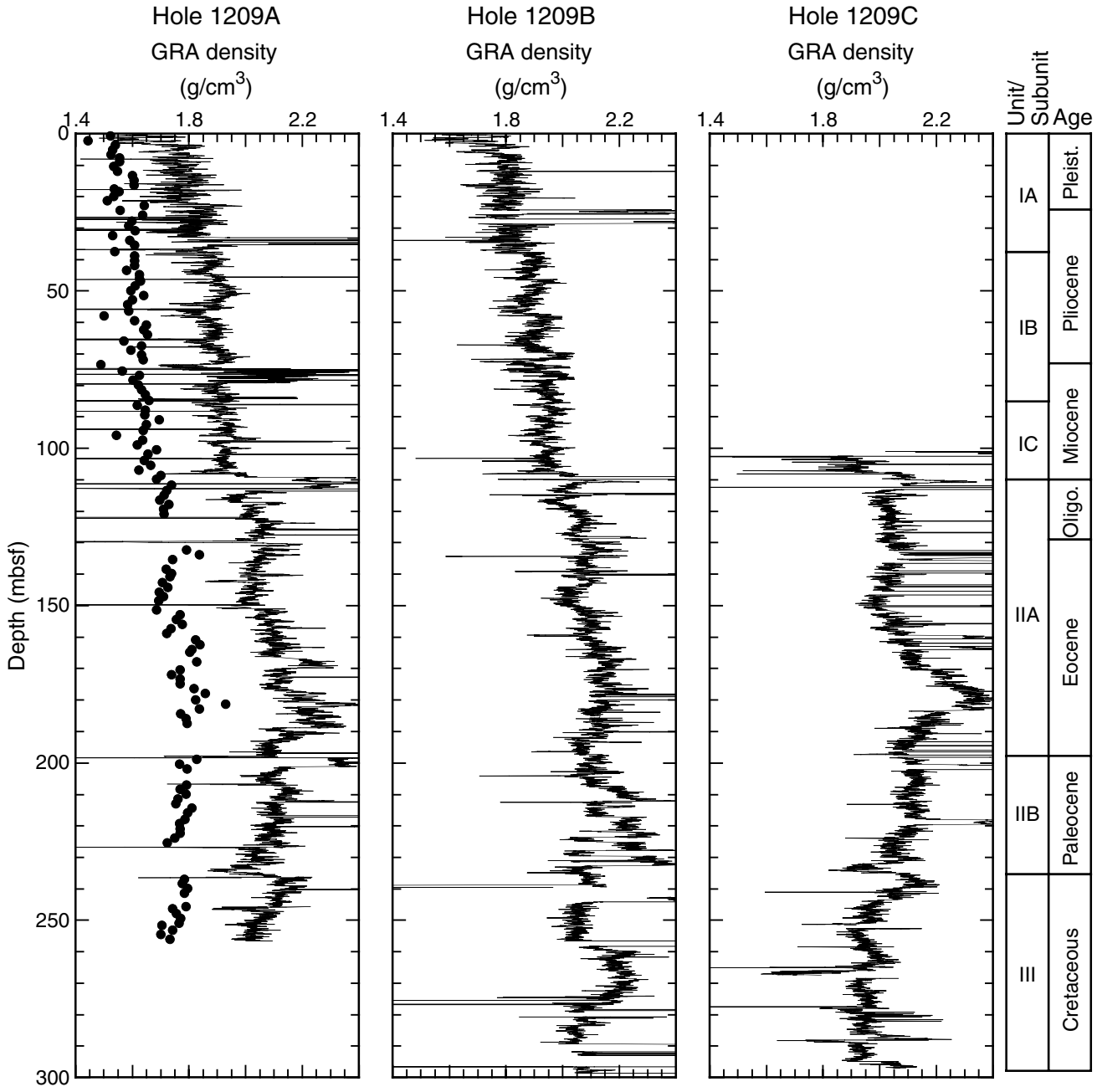

Figure F34. MST *P*-wave velocity (solid dots) measured in Holes 1209A, 1209B, and 1209C whole cores, plotted vs. depth. For comparison, discrete *P*-wave velocity data (open circles) are also shown.

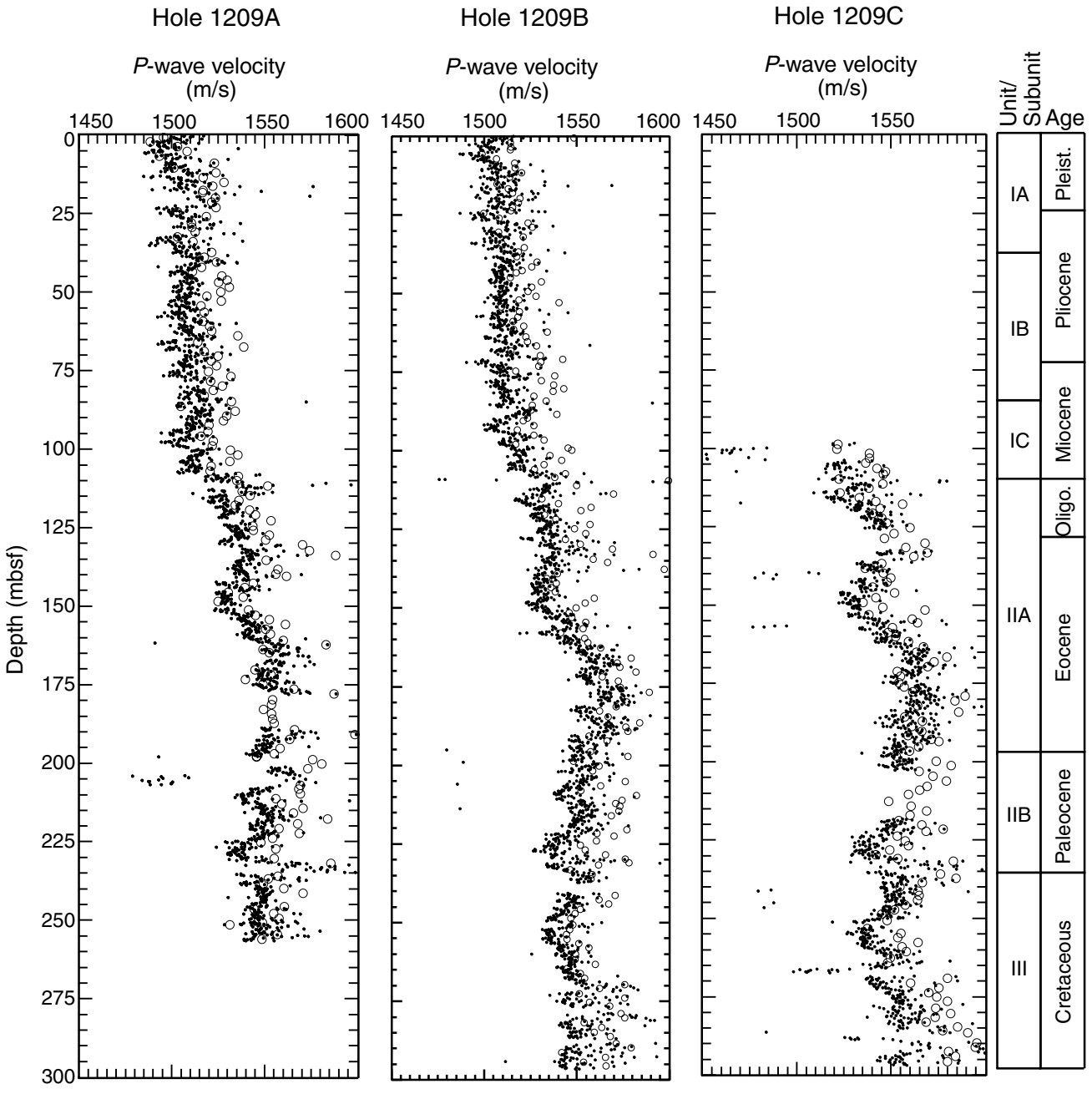

Figure F35. MST natural gamma radiation data for Holes 1209A and 1209B plotted vs. depth.

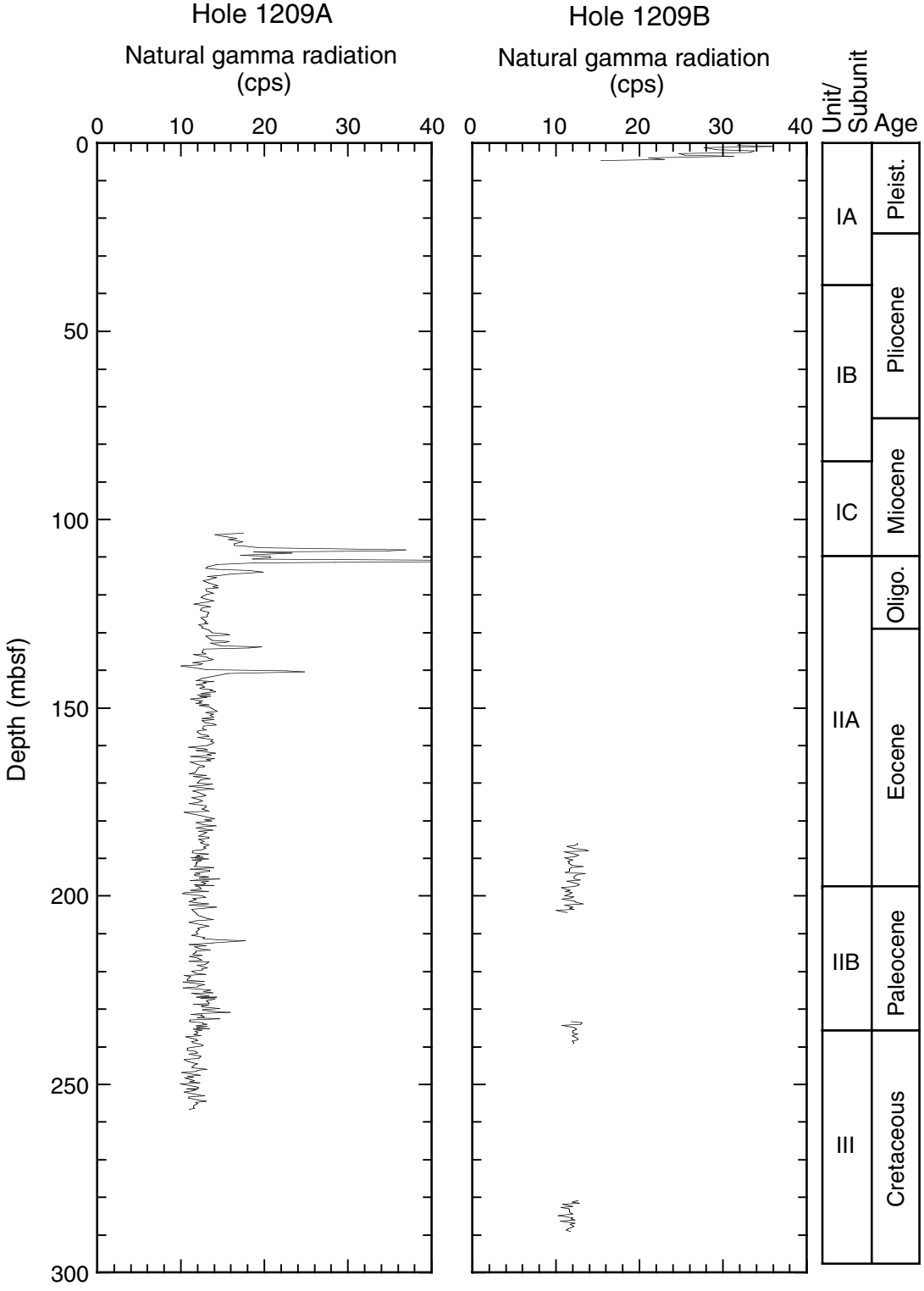

Figure F36. *P*-wave velocities for discrete samples from Holes 1209A, 1209B, and 1209C (see Table **T13,** p. 98, for data).

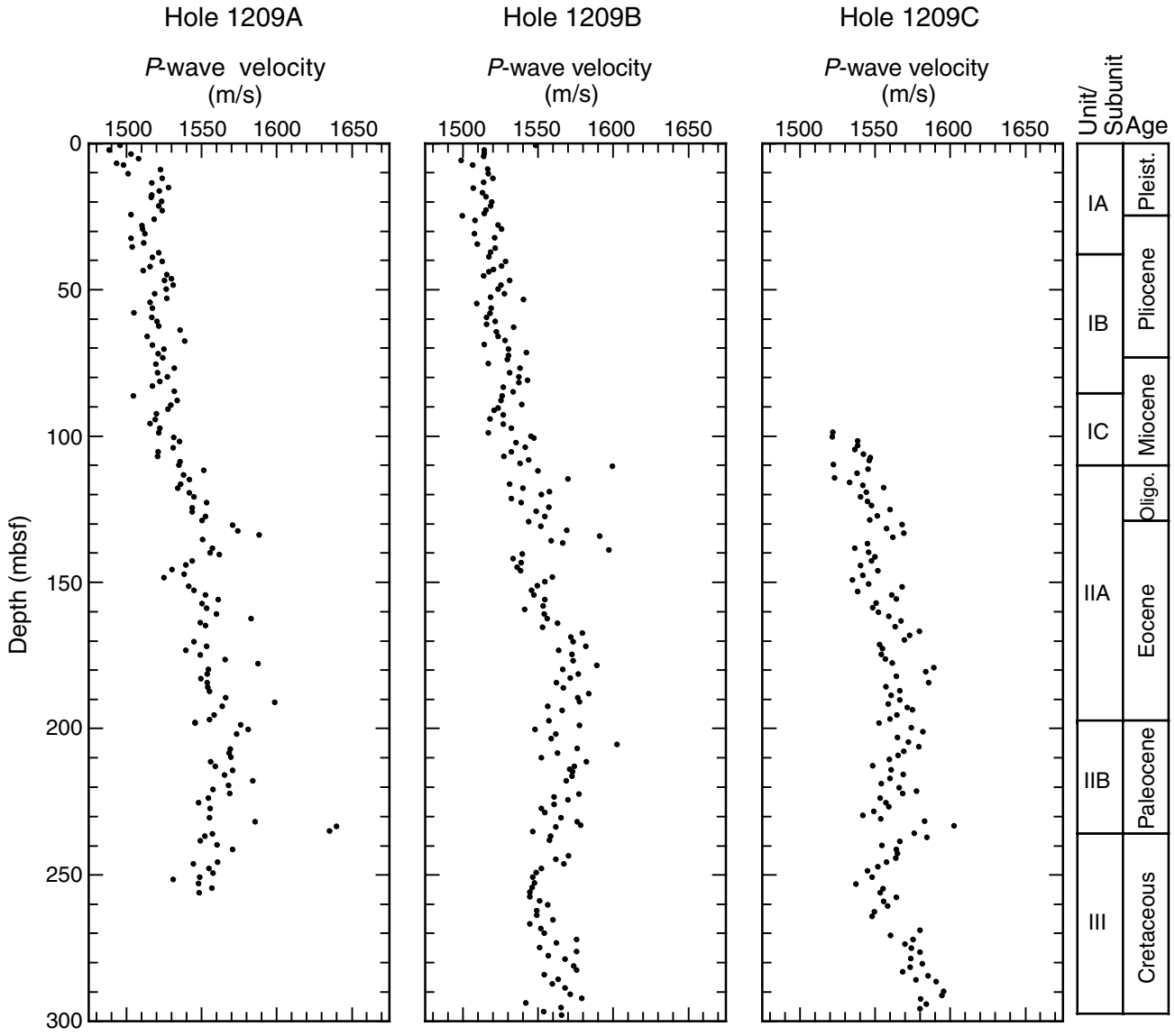

Figure F37. Water content (A) calculated relative to bulk sediment (circles) and solid phase (triangles), (B) porosity, and (C) void ratio determined for discrete samples from Hole 1209A (solid circles and triangles) and Hole 1209B (open circles and triangles) plotted vs. depth.

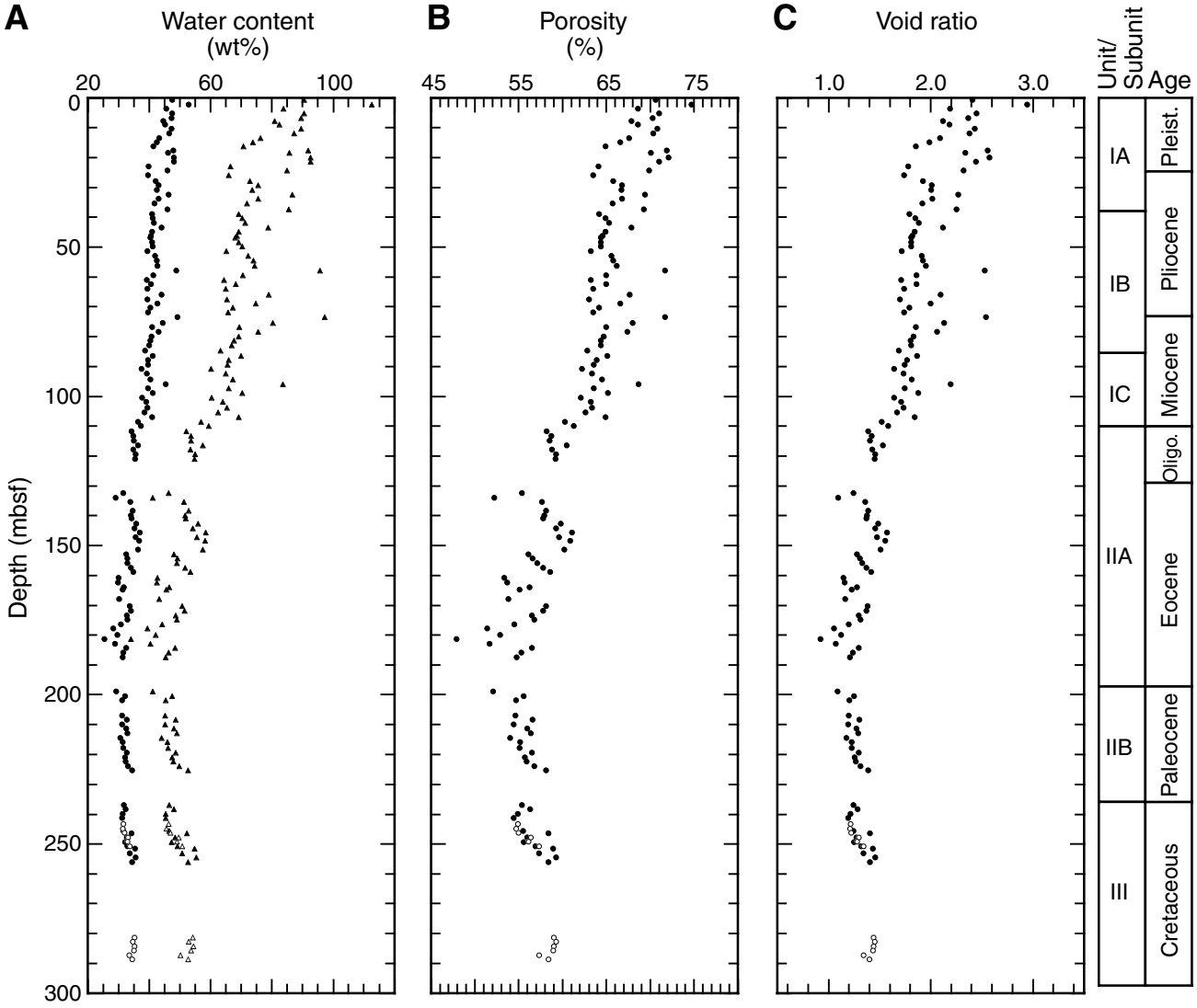

Figure F38. Discrete measurements of Hole 1209A *P*-wave velocities plotted vs. discrete wet bulk density measurements at comparable stratigraphic horizons.

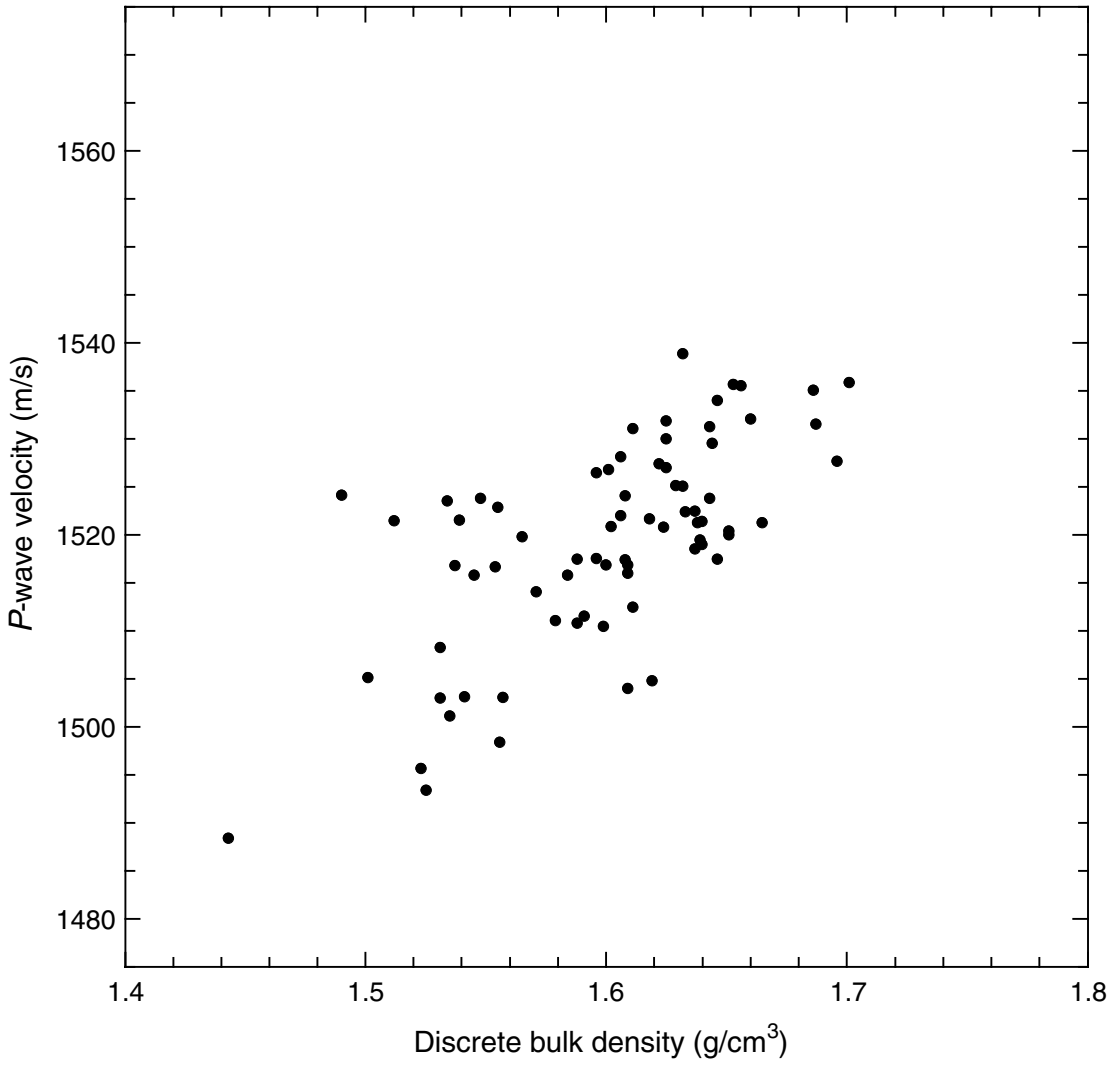

Figure F39. Thermal conductivity measured on Hole 1209A (solid circles) and Hole 1209B (open circles) whole cores plotted vs. depth. See Table T14, p. 101, for these data.

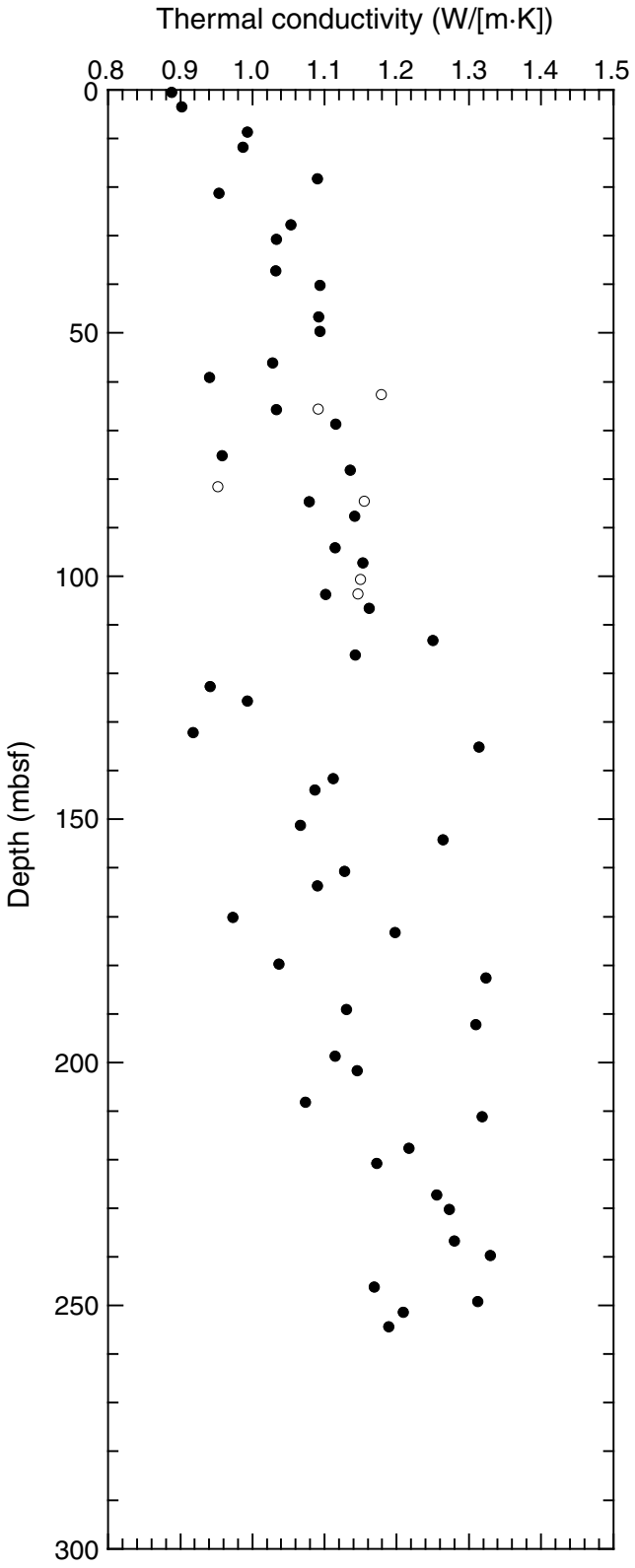

Figure F40. Hole 1209A whole-core thermal conductivity plotted vs. discrete measurements of porosity.

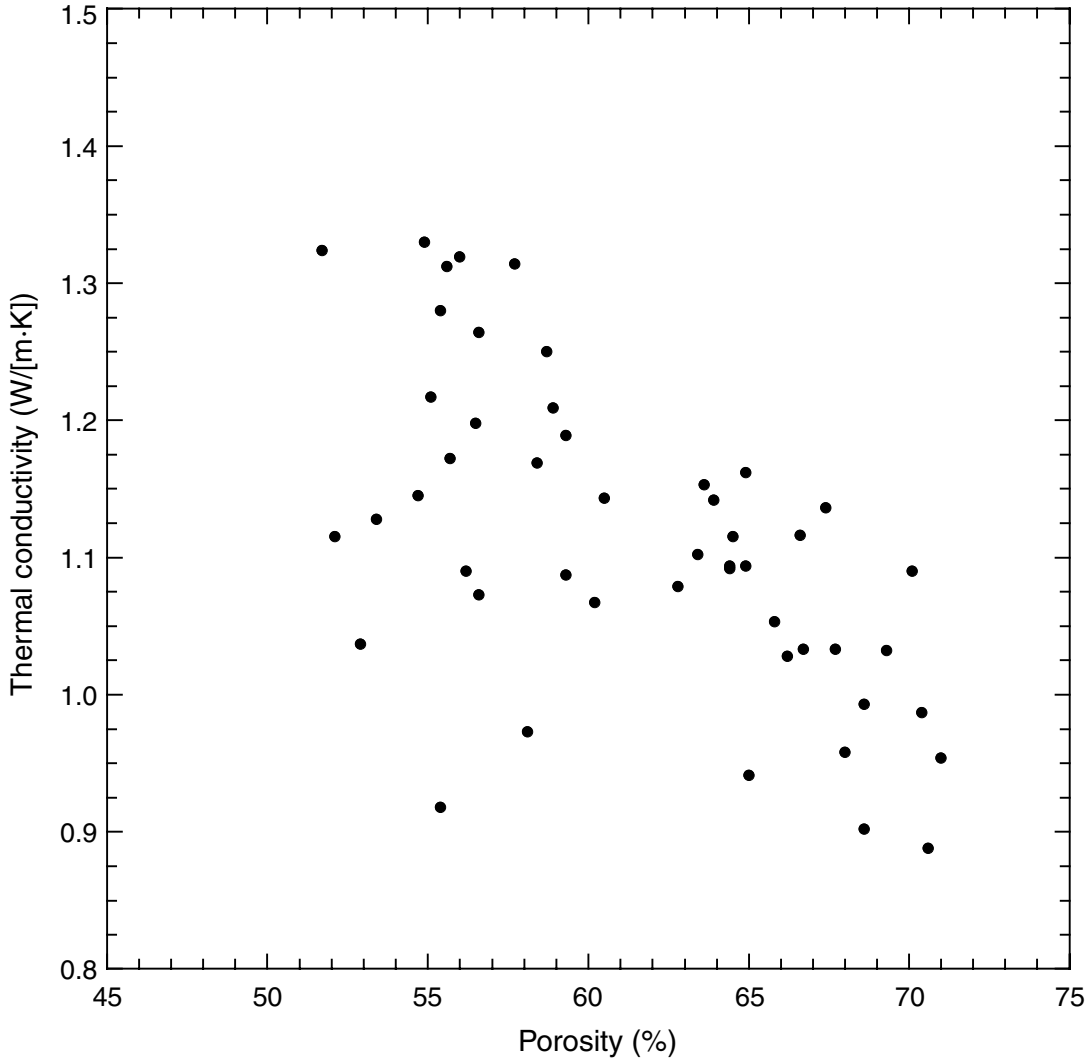

Figure F41. Example temperature data profile collected during deployment of the Adara in situ temperature tool (see data in Table T15, p. 102). APC = advanced piston corer.

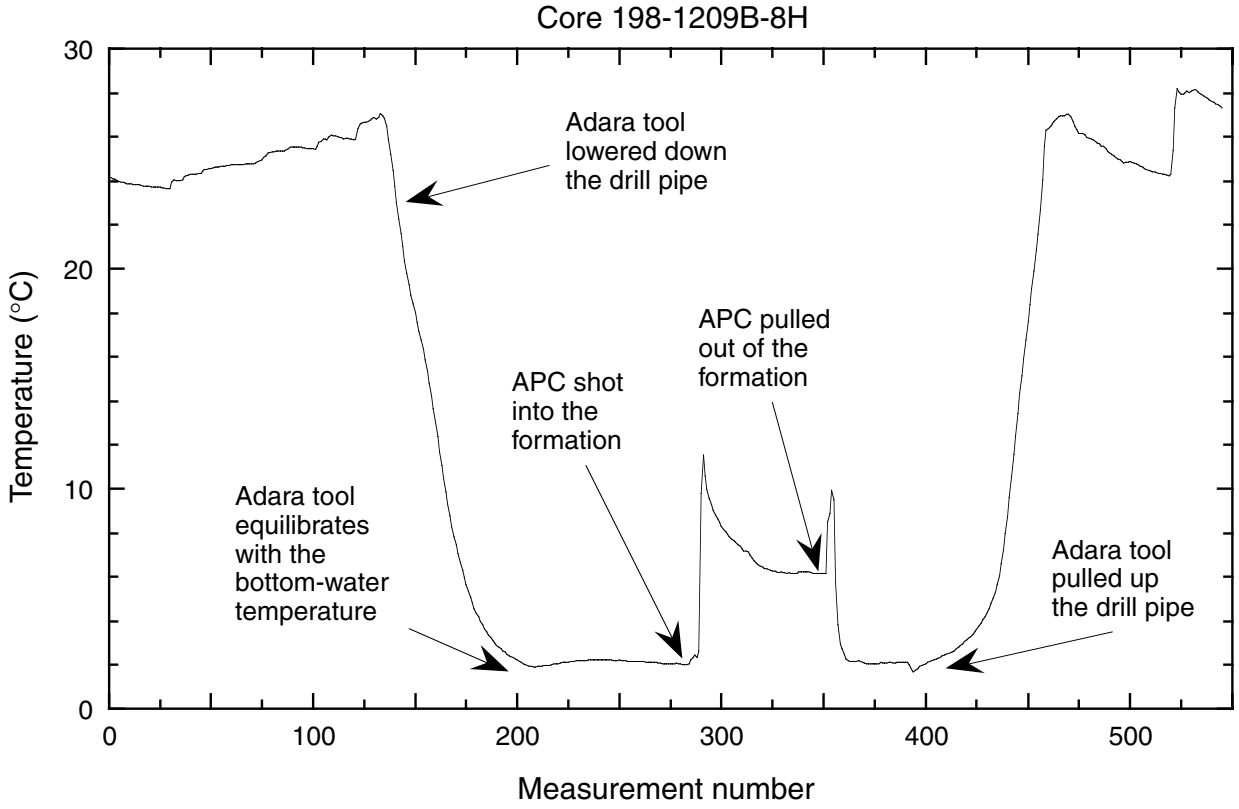

Figure F42. In situ Adara temperature measurements from Hole 1209B plotted vs. depth. Error bars represent ± 0.1°C.

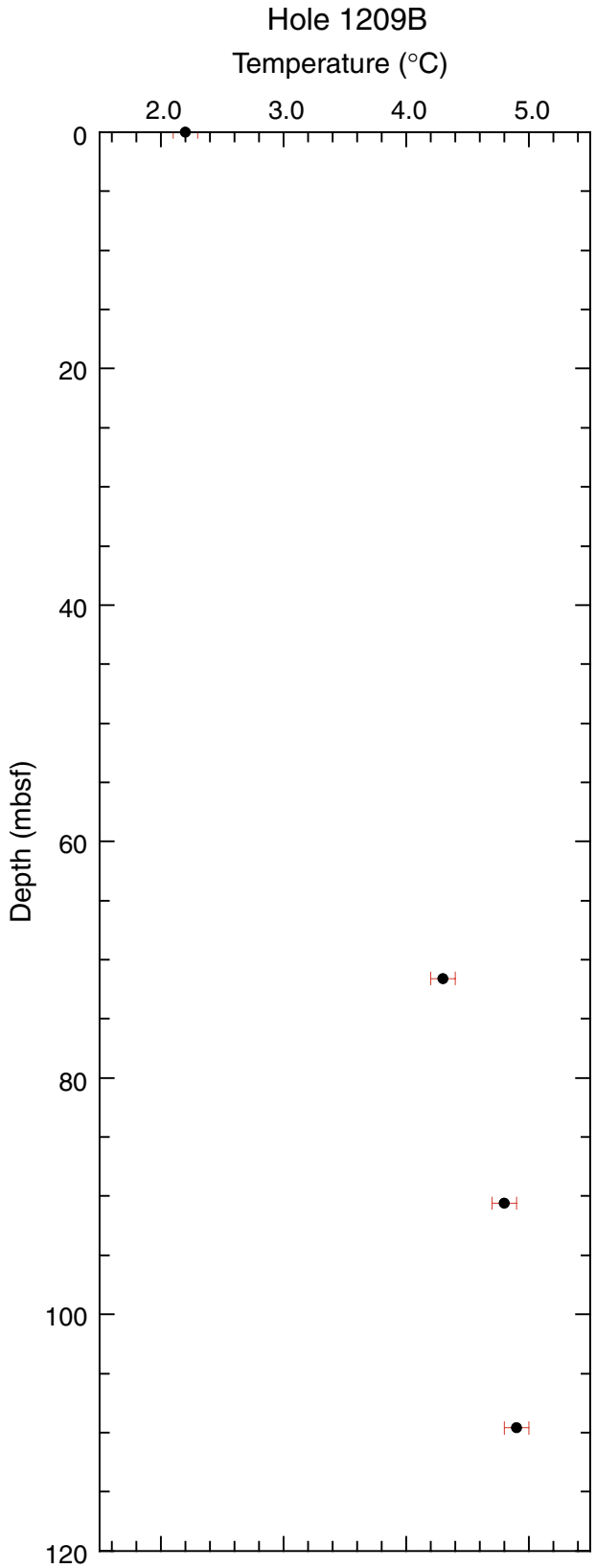

Figure F43. (A) Wet bulk density, (B) dry density, and (C) grain density determined for discrete samples from Hole 1209A (solid circles) and Hole 1209B (open circles), plotted vs. depth.

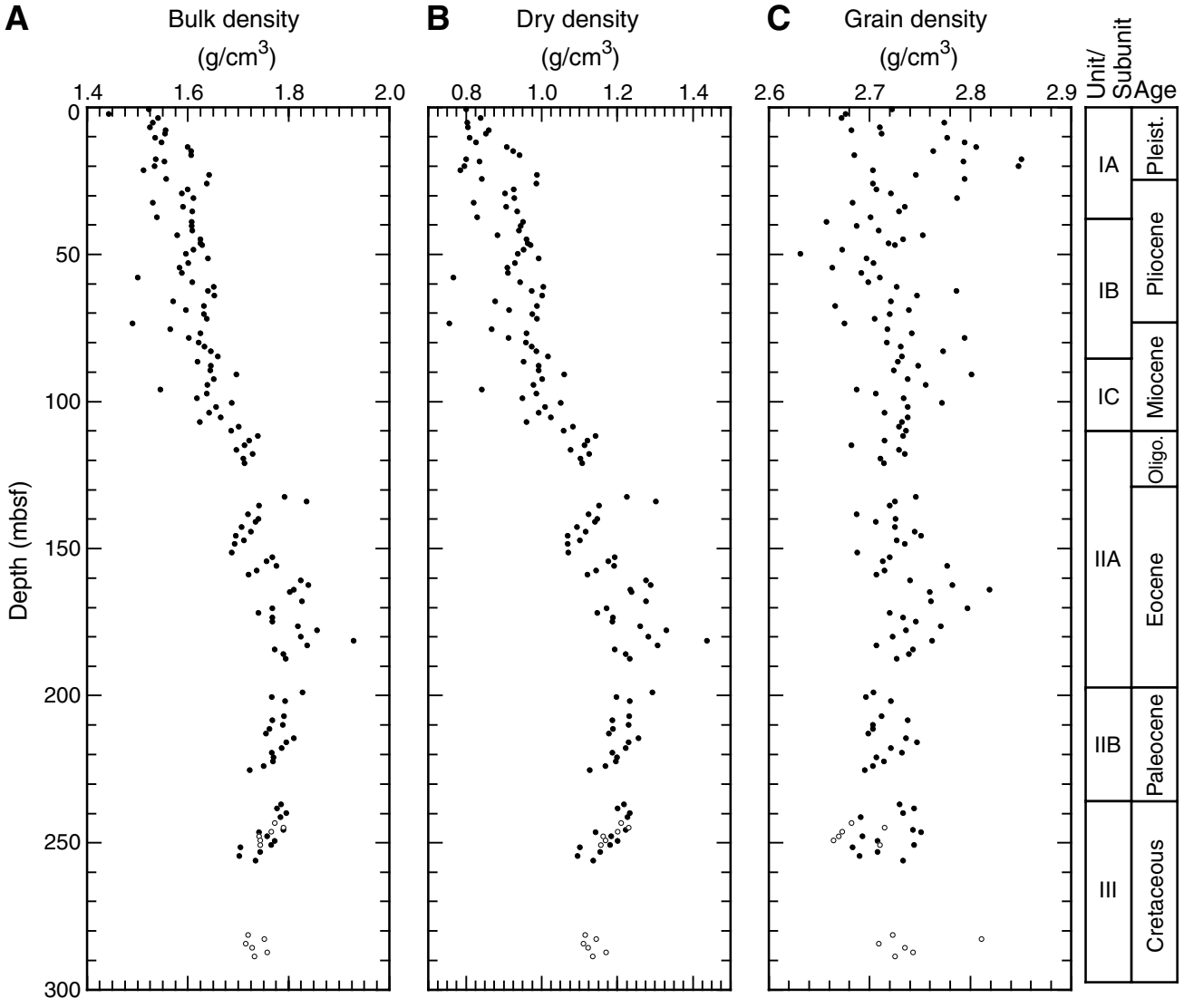

Table T1. Coring summary, Site 1209. (Continued on next two pages.)

Hole 1209A
Latitude: 32°39.1001′N
Longitude: 158°30.3560′E
Time on site (hr): 116.5 (0800 hr, 18 Sep–0430 hr, 23 Sep 2001)
Time on hole (hr): 29.5 (0800 hr, 18 Sep–1330 hr, 19 Sep 2001)
Seafloor (drill pipe measurement from rig floor, mbrf): 2398.3
Distance between rig floor and sea level (m): 11.1
Water depth (drill pipe measurement from sea level, m): 2387.2
Total depth (drill pipe measurement from rig floor, mbrf): 2657.9
Total penetration (mbsf): 259.6
Total length of cored section (m): 259.6
Total core recovered (m): 262.27
Core recovery (%): 101.03
Total number of cores: 28
Total number of drilled intervals: 0

Hole 1209B
Latitude: 32°39.1081′N
Longitude: 158°30.3564′E
Time on hole (hr): 41.75 (1330 hr, 19 Sep–0715 hr, 21 Sep 2001)
Seafloor (drill pipe measurement from rig floor, mbrf): 2398.4
Distance between rig floor and sea level (m): 11.0
Water depth (drill pipe measurement from sea level, m): 2387.4
Total depth (drill pipe measurement from rig floor, mbrf): 2696.4
Total penetration (mbsf): 298.0
Total length of cored section (m): 297.6
Total core recovered (m): 303.17
Core recovery (%): 101.9
Total number of cores: 32
Total number of drilled intervals: 1

Hole 1209C
Latitude: 32°39.0995′N
Longitude: 158°30.3653′E
Time on hole (hr): 45.25 (0715 hr, 21 Sep–0430 hr, 23 Sep 2001)
Seafloor (drill pipe measurement from rig floor, mbrf): 2398.4
Distance between rig floor and sea level (m): 11.1
Water depth (drill pipe measurement from sea level, m): 2387.3
Total depth (from rig floor, mbrf): 2705.9
Total penetration (mbsf): 307.5
Total length of cored section (m): 202.2
Total core recovered (m): 200.60
Core recovery (%): 99.2
Total number of cores: 23
Total number of drilled intervals: 4

Core	Date (Sep 2001)	Local time (hr)	Depth (mbsf) Top	Depth (mbsf) Bottom	Length (m) Cored	Length (m) Recovered	Recovery (%)
198-1209A-							
1H	18	1430	0.0	8.2	8.2	8.21	100.1
2H	18	1514	8.2	17.7	9.5	9.87	103.9
3H	18	1555	17.7	27.2	9.5	9.76	102.7
4H	18	1640	27.2	36.7	9.5	9.76	102.7
5H	18	1714	36.7	46.2	9.5	9.91	104.3
6H	18	1800	46.2	55.7	9.5	9.94	104.6
7H	18	1845	55.7	65.2	9.5	9.88	104.0
8H	18	1930	65.2	74.7	9.5	9.93	104.5
9H	18	2015	74.7	84.2	9.5	10.01	105.4
10H	18	2100	84.2	93.7	9.5	9.91	104.3
11H	18	2140	93.7	103.2	9.5	9.72	102.3
12H	18	2226	103.2	112.7	9.5	9.74	102.5
13H	18	2305	112.7	122.2	9.5	9.52	100.2
14H	18	2345	122.2	131.7	9.5	9.12	96.0
15H	19	0030	131.7	141.2	9.5	9.44	99.4
16H	19	0115	141.2	150.7	9.5	8.77	92.3
17H	19	0200	150.7	160.2	9.5	9.87	103.9
18H	19	0245	160.2	169.7	9.5	9.16	96.4
19H	19	0330	169.7	179.2	9.5	9.35	98.4
20H	19	0425	179.2	188.7	9.5	9.87	103.9
21H	19	0510	188.7	198.2	9.5	9.76	102.7

Table T1 (continued).

Core	Date (Sep 2001)	Local time (hr)	Depth (mbsf) Top	Depth (mbsf) Bottom	Length (m) Cored	Length (m) Recovered	Recovery (%)
22H	19	0600	198.2	207.7	9.5	9.22	97.1
23H	19	0645	207.7	217.2	9.5	9.90	104.2
24H	19	0730	217.2	226.7	9.5	9.94	104.6
25H	19	0815	226.7	236.2	9.5	9.83	103.5
26H	19	0900	236.2	245.7	9.5	9.88	104.0
27X	19	1015	245.7	250.9	5.2	5.94	114.2
28X	19	1150	250.9	259.6	8.7	6.06	69.7
				Cored totals:	259.6	262.27	101.0
198-1209B-							
1H	19	1510	0.0	5.1	5.1	5.16	101.2
2H	19	1605	5.1	14.6	9.5	9.80	103.2
3H	19	1645	14.6	24.1	9.5	10.02	105.5
4H	19	1720	24.1	33.6	9.5	10.07	106.0
5H	19	1805	33.6	43.1	9.5	9.99	105.2
6H	19	1900	43.1	52.6	9.5	10.13	106.6
7H	19	2005	52.6	62.1	9.5	10.06	105.9
8H	19	2100	62.1	71.6	9.5	10.14	106.7
9H	19	2200	71.6	81.1	9.5	9.99	105.2
10H	19	2310	81.1	90.6	9.5	9.88	104.0
11H	20	0010	90.6	100.1	9.5	10.05	105.8
12H	20	0125	100.1	109.6	9.5	10.07	106.0
13H	20	0225	109.6	119.1	9.5	9.94	104.6
14H	20	0310	119.1	128.6	9.5	9.73	102.4
15H	20	0355	128.6	138.1	9.5	9.53	100.3
16H	20	0440	138.1	147.6	9.5	9.39	98.8
17H	20	0535	147.6	157.1	9.5	9.78	102.9
18H	20	0700	157.1	166.6	9.5	9.70	102.1
19H	20	0745	166.6	176.1	9.5	9.46	99.6
20H	20	0840	176.1	185.6	9.5	9.18	96.6
21H	20	0925	185.6	195.1	9.5	9.63	101.4
22H	20	1010	195.1	204.6	9.5	9.75	102.6
23H	20	1050	204.6	214.1	9.5	9.76	102.7
24H	20	1145	214.1	223.6	9.5	9.88	104.0
25H	20	1225	223.6	233.1	9.5	9.90	104.2
26H	20	1315	233.1	242.6	9.5	6.51	68.5
27H	20	1400	242.6	252.1	9.5	9.69	102.0
28H	20	1445	252.1	261.6	9.5	9.82	103.4
29H	20	1600	261.6	271.1	9.5	9.55	100.5
30H	20	1705	271.1	280.6	9.5	8.32	87.6
31H	20	1745	280.6	290.1	9.5	8.98	94.5
32H	20	1930	290.1	297.6	7.5	9.31	124.1
		*****Drilled from 297.6 to 298.0 mbsf*****					
				Cored totals:	297.6	303.17	101.9
				Drilled total:	0.4		
				Total:	298.0		
198-1209C-							
		*****Drilled from 0.0 to 98.0 mbsf*****					
1H	21	1540	98.0	107.5	9.5	10.07	106.0
2H	21	1630	107.5	117.0	9.5	9.87	103.9
3H	21	1707	117.0	126.5	9.5	9.11	95.9
4H	21	1750	126.5	136.0	9.5	9.28	97.7
5H	21	1835	136.0	145.5	9.5	9.63	101.4
6H	21	1920	145.5	155.0	9.5	9.66	101.7
7H	21	2010	155.0	164.5	9.5	9.71	102.2
8H	21	2045	164.5	174.0	9.5	9.09	95.7
9H	21	2130	174.0	183.5	9.5	9.37	98.6
10H	21	2215	183.5	193.0	9.5	9.91	104.3
11H	22	0040	193.0	202.5	9.5	10.09	106.2
12H	22	0135	202.5	212.0	9.5	9.40	98.9
13H	22	0230	212.0	221.5	9.5	10.00	105.3
14H	22	0320	221.5	231.0	9.5	9.83	103.5
15H	22	0415	231.0	240.5	9.5	9.89	104.1
16H	22	0520	240.5	250.0	9.5	9.79	103.1
17H	22	0625	250.0	251.5	1.5	1.60	106.7
		*****Drilled from 251.5 to 252.5 mbsf*****					
18H	22	0810	252.5	262.0	9.5	9.81	103.3
19H	22	0905	262.0	264.9	2.9	5.56	191.7
		*****Drilled from 264.9 to 268.4 mbsf*****					

Table T1 (continued).

Core	Date (Sep 2001)	Local time (hr)	Depth (mbsf) Top	Depth (mbsf) Bottom	Length (m) Cored	Length (m) Recovered	Recovery (%)
20H	22	1200	268.4	277.9	9.5	9.89	104.1
21H	22	1305	277.9	287.4	9.5	9.28	97.7
22H	22	1450	287.4	296.9	9.5	9.76	102.7
		*****Drilled from 296.9 to 299.7 mbsf*****					
23X	22	2000	299.7	307.5	7.8	0.00	0.0
				Cored totals:	202.2	200.60	99.2
				Drilled total:	105.3		
				Total:	307.5		

Table T2. Calcareous nannofossil datums, ages, and depths, Site 1209.

Datum	Zone/ Subzone (base)	Core, section, interval (cm)	Depth (mbsf)	Core, section, interval (cm)	Depth (mbsf)	Core, section, interval (cm)	Depth (mbsf)	Age (Ma)
		198-1209A-		198-1209B-		198-1209C-		
LO *Pseudoemiliania lacunosa*	CN14b	1H-CC	8.13	1H-CC	5.11			0.46
LO *Discoaster brouweri*	CN13	3H-CC	27.41	4H-CC	34.12			1.95
LO *Reticulofenestra pseudoumbilicus*	CN12	5H-CC	46.56	6H-CC	53.18			3.82
LO *Amaurolithus* spp.	CN11	6H-CC	56.09					4.56
FO *Ceratolithus rugosus*	CN10c	7H-CC	65.53	8H-CC	72.19			5.1
FO *Discoaster berggrenii*	CN9	9H-CC	84.66	10H-CC	90.93			8.2
LO *Discoaster hamatus*	CN7	10H-CC	94.06	11H-CC	100.55			10.476
FO *Sphenolithus heteromorphus*	CN3	12H-4, 90	108.60	12H-CC	110.07	1H-CC	108.02	18.2
LO *Reticulofenestra bisectus*	CN1	12H-6, 52	111.22					23.9
FO *Sphenolithus ciperoensis*	CP19a	12H-CC	112.89					29.9
FO *Sphenolithus distentus*	CP18	13H-CC	122.17	13H-CC	119.44	2H-CC	117.27	31.5
TA *Ericsonia subdisticha*	CP16b			14H-CC	128.78	3H-CC	126.01	33.3
LO *Chiasmolithus grandis*	CP15	14H-5, 80	129.00	15H-CC	138.03	4H-CC	135.68	37.1
FO *Reticulofenestra umbilicus*	CP14	15H-CC	141.04					43.7
FO *Nannotetrina fulgens*	CP13	17H-CC	160.47	17H-CC	157.28	6H-CC	155.06	47.3
FO *Discoaster sublodoensis*	CP12	19H-CC	178.95	18H-CC	166.70	8H-CC	173.54	49.7
FO *Coccolithus crassus*	CP11					9H-CC	183.32	51.5
FO *Discoaster lodoensis*	CP10	20H-CC	188.97	20H-CC	185.18			52.8
FO *Tribrachiatus orthostylus*	CP9b	21H-3, 130	193.00	21H-4, 100	191.1			53.6
FO *Discoaster diastypus*	CP9a	21H-5, 130	196.00	21H-5, 100	192.6			55.0
FO *Tribrachiatus bramlettei*	CP9a	21H-5, 130	196.00			10H-CC	193.36	55.0
FO *Discoaster multiradiatus*	CP8	21H-CC	198.36	22H-1, 147	196.57	11H-CC	202.99	56.2
FO *Discoaster nobilis*	CP7	22H-CC	207.37	22H-CC	204.75			56.9
FO *Fasciculithus tympaniformis*	CP4	23H-CC	217.55	23H-CC	214.31	12H-CC	211.80	59.7
FO *Ellipsolithus macellus*	CP3	24H-CC	227.09			13H-CC	221.9	62.2
FO *Chiasmolithus danicus*	CP2					14H-CC	231.23	63.8
LO Cretaceous taxa	CP1a	25H-CC	236.48					65.0
FO *Micula prinsii*	CC26	25H-CC	236.48	26H-CC	239.51	15H-CC	240.79	65.4
LO *Reinhardtites levis*	CC25			28H-CC	261.87	19H-CC	267.51	69.2

Notes: FO = first occurrence, LO = last occurrence. TA = top of acme.

Table T3. Planktonic foraminifer datums, ages, and depths, Site 1209.

Datum	Zone/ Subzone (base)	Core, section, interval (cm)	Depth (mbsf)	Core, section, interval (cm)	Depth (mbsf)	Core, section, interval (cm)	Depth (mbsf)	Age (Ma)
		198-1209A-		198-1209B-		198-1209C-		
LO *Globigerinoides obliquus*		3H-CC	27.41	4H-CC	34.12			1.3
FO *Truncorotalia truncatulinoides*	N22	2H-CC	18.02	3H-CC	24.57			1.92
LO *Globigerinoides extremus*		4H-CC	36.91	7H-CC	62.61			1.98
FO *Truncorotalia tosaensis*	N21	5H-CC	46.56	4H-CC	34.12			3.35
LO *Dentoglobigerina altispira*		6H-CC	56.09	9H-CC	81.54			3.11
LO *Sphaeroidinellopsis seminulina*		6H-CC	56.09	5H-CC	43.54			3.11
LO *Globorotalia margaritae*		8H-CC	75.08	6H-CC	53.18			3.85
FO *Truncorotalia crassaformis*		6H-CC	56.09	5H-CC	43.54			4.31
LO *Globoturborotalita nepenthes*		6H-CC	56.09	8H-CC	72.19			4.39
FO *Globorotalia tumida*	N18	8H-CC	75.08	7H-CC	62.61			5.82
FO *Globorotalia margaritae*		8H-CC	75.08	6H-CC	53.18			6.09
LO *Paragloborotalia mayeri*	N15	10H-CC	94.06					10.49
FO *Globoturborotalita nepenthes*	N14	11H-CC	103.37	11H-CC	100.55			11.19
FO *Orbulina universa*	N9	11H-CC	103.37	11H-CC	100.55			15.1
FO *Praeorbulina sicana*	N8			12H-CC	110.07			16.4
FO *Globoquadrina dehiscens*	M1b	10H-CC	94.06	12H-CC	110.07			23.2
LO *Subbotina angiporoides*		12H-CC	112.89			2H-CC	117.27	30.0
LO *Pseudohastigerina* spp.	P19	13H-CC	122.17					32.0
LO *Hantkenina* spp.		14H-5, 36–37	128.56	14H-CC	128.78			33.7
LO *Globigerinatheka index*		14H-CC	131.22	15H-CC	138.03	4H-CC	135.68	34.3
LO *Acarinina primitiva*		15H-CC	141.04			6H-CC	155.06	39.0
LO "*Orbulinoides" beckmanni*	P14	15H-CC	141.04					40.1
FO "*Orbulinoides" beckmanni*	P13	15H-CC	141.04					40.5
LO *Acarinina bullbrooki*		15H-CC	141.04	16H-CC	147.39	8H-CC	173.54	40.5
FO *Turborotalia pomeroli*				15H-CC	138.03			
LO *Morozovella aragonensis*	P12	17H-CC	160.47	16H-CC	147.39	9H-CC	183.32	43.6
FO *Globigerinatheka kugleri*	P11					6H-CC	155.06	45.8
FO *Hantkenina* spp.	P10	17H-CC	160.47	16H-CC	147.39			49.0
LO *Morozovella formosa*	P8	19H-CC	178.95					50.8
FO *Acarinina pentacamerata*		18H-CC	169.26	19H-CC	175.96			50.8
FO *Morozovella aragonensis*	P7	21H-3, 68–69	192.38	19H-CC	175.96			52.3
LO *Morozovella aequa*		21H-3, 50–51	192.20	21H-CC	195.13			53.6
FO *Morozovella formosa*	P6b	21H-3, 68–69	192.38			10H-CC	193.36	54.0
LO *Morozovella velascoensis*	P6a	21H-5, 129–130	195.99	22H-CC	204.75			54.7
FO *Morozovella gracilis*		21H-5, 49–50	195.19					54.7
FO *Morozovella subbotinae*		21H-CC	198.36	21H-CC	195.13	11H-CC	202.99	55.9
LO *Globanomalina pseudomenardii*	P5	21H-CC	198.36			11H-CC	202.99	55.9
LO *Acarinina mckannai*		21H-CC	198.36	22H-CC	204.75	11H-CC	202.99	56.3
FO *Acarinina mckannai*		22H-CC	207.37	22H-CC	204.75	12H-CC	211.80	59.1
FO *Globanomalina pseudomenardii*	P4a	23H-CC	217.55			12H-CC	211.80	59.2
FO *Morozovella velascoensis*		23H-CC	217.55	23H-CC	214.31	12H-CC	211.80	60.0
FO *Morozovella angulata*						13H-CC	221.90	61.0
FO *Igorina pusilla*		23H-CC	217.55	24H-CC	223.88	12H-CC	211.80	61.0
FO *Praemurica uncinata*	P2	24H-CC	227.09	24H-CC	223.88	14H-CC	231.23	61.2
FO *Praemurica inconstans*		24H-CC	227.09	24H-CC	223.88	14H-CC	231.23	63.0
LO *Parvularugoglobigerina eugubina*	P1a	25H-6, 93–94	235.13	26H-CC	239.51			64.7
FO *Parvularugoglobigerina eugubina*	P1a	25H-6, 93–94	235.13					64.97
LO *Abathomphalus mayaroensis*		25H-6, 93–94	235.13	27H-CC	252.24	15H-CC	240.79	65.0
FO *Abathomphalus mayaroensis*	KS31	28X-CC	256.91	28H-CC	261.87	18H-CC	262.26	68.6
FO *Racemiguembelina fructicosa*		28X-CC	256.91	30H-CC	279.37	20H-CC	278.19	69.6
FO *Contusotruncana contusa*		28X-CC	256.91	30H-CC	279.37	20H-CC	278.19	69.6

Note: FO = first occurrence, LO = last occurrence.

Table T4. Distribution of Cenozoic and Cretaceous benthic foraminifers, Hole 1209A. (Continued on next page.)

| Core, section | Depth (mbsf) | Nannofossil zone/ subzone | Size fraction (µm) | Preservation | Benthic abundance | Trochospiral and planispiral | | | | | | | | | | | | | | | | | | | | | | | | | | | | Other forms | | | | | | | | | | | | | | | | | | |

Table T4 (continued).

Core, section	Depth (mbsf)	Nannofossil zone/ subzone	Size fraction (µm)	Preservation	Benthic abundance	Buliminids									*Stilostomella*				*Uvigerina*				Agglutinated									
						Buliminella grata	*Bulimina* spp.	*Bulimina velascoensis*	*Bulimina impendens*	*Bulimina trinitatensis*	*Quadratobuliminella pyramidalis*	*Bulimina semicostata*	*Bulimina jarvisi*		*Stilostomella* spp.	*Stilostomella gracillima*	*Stilostomella subspinosa*	*Stilostomella abyssorum*	*Uvigerina havanensis*	*Uvigerina* spp.	*Uvigerina hispida*	*Uvigerina hispidocostata*	*Pseudoclavulina rugolosa*	*Marssonella trochoides*	*Tritaxia* spp.	*Gaudryina pyramidata*	*Spiroplectammina jarvisi*	*Bathysiphon* spp.	*Karreriella bradyi*	*Vulvulina mexicana*	*Vulvulina spinosa*	*Martinottiella* sp.	*Eggerella bradyi*
198-1209A-																																
1H-CC	8.13	CN14a	>250	G	R															T		R										
3H-CC	27.41	CN13a	>250	G	F															T	R	R										F
5H-CC	46.56	CN12b	>250	G	F												F				F	R									T	
7H-CC	65.53	CN10c	>250	G	F											T	T											R				R
9H-CC	84.66	u. CN9	>250	G	C											T	F			R	R	F						R			F	R
11H-CC	103.37	CN3–4	>250	M	F										R	T	C	R		T												
12H-CC	112.89	CP19a	>250	G	C				F						R	F	F												T	R		
13H-CC	122.17	CP18	>250	G	F				F				F		F	T	R		R	T									R	F		
14H-CC	131.22	CP14b	>125	P	C	T			R	R					T													T				
15H-CC	141.04	CP14a	>250	M	F				F			C	R		R	F	R										T	R				
17H-CC	160.47	CP13	>125	G	R	R			R			F	R		T	R																
19H-CC	178.95	CP12	>125	M	R								R		R																	
20H-CC	188.97	CP9b–10	>125	M	T	T					R	R	F		T	R																
21H-CC	198.36	CP8	>125	G	R										R								C		R	T	F	R				
23H-CC	217.55	CP4	>250	G	F	C		R	R	T					T										T							
24H-CC	227.09	CP3	>250	G	R	T		C	R															C								
25H-CC	236.48	CC26	>125	G	A		R																C									
27X-CC	251.54	u. CC25	>125	M	R	R									T																	

Table T5. Distribution of Cenozoic and Cretaceous benthic foraminifers, Hole 1209C. (Continued on next page.)

| Core, section | Depth (mbsf) | Nannofossil zone/ subzone | Size fraction (µm) | Preservation | Benthic abundance | Trochospiral and planispiral | | | | | | | | | | | | | | | | | | | | | | | | | | | | Other forms | | | | | | | | | | | | | | | | | | | | | | Buliminids | | | | | |
|---|---|---

Table T5 (continued).

Core, section	Depth (mbsf)	Nannofossil zone/ subzone	Size fraction (µm)	Preservation	Benthic abundance	*Stilostomella*				Agglutinated									
						Stilostomella subspinosa	*Stilostomella* spp.	*Stilostomella abyssorum*	*Stilostomella gracillima*	*Pseudoclavulina globulifera*	*Gaudryina* spp.	*Tritaxia* spp.	*Gaudryina pyramidata*	*Spiroplectammina jarvisi*	*Marssonella trochoides*	*Pseudoclavulina rugolosa*	*Bathysiphon* spp.	*Vulvulina spinosa*	*Martinottiella* sp.	*Eggerella bradyi*
198-1209C-																				
1H-CC	108.02	CN3–4	>250	G	F														R	R
3H-CC	126.01	CP16b	>250	M	C	C	T	T	R									T		
5H-CC	145.53	CP13b	>125	M	R	F	R	T	R								R			
7H-CC	164.66	CP12	>125	G	R		R										T			
9H-CC	183.32	CP11	>125	M	R	R	R		F								T			
10H-CC	193.36	CP9?a	>125	M	R	R	R													
11H-CC	202.99	CP8	>125	G	R		R								T		T			
12H-CC	211.80	CP4	>125	G	C	R	R							T	T					
13H-CC	221.90	CP3	>125	G	F	T	T							R	R	F				
15H-CC	240.79	CC26	>125	G	A	T	R					T	F	R	R	T				
16H-CC	250.19	u.CC25	>125	G	F	T					F		F	F	R					
19H-CC	267.51	CC24/25	>125	M	R							R	R	T	R					
22H-CC	297.11	CC24/25	>125	M	R					T	R	R	T							

Table T6. Composite depth section, Site 1209.

Core	Depth (mbsf)	Offset (m)	Depth (mcd)
198-1209A-			
1H	0.0	0.00	0.00
2H	8.2	0.08	8.28
3H	17.7	3.06	20.76
4H	27.2	3.67	30.87
5H	36.7	3.86	40.56
6H	46.2	4.71	50.91
7H	55.7	6.01	61.71
8H	65.2	6.59	71.79
9H	74.7	7.62	82.32
10H	84.2	8.29	92.49
11H	93.7	10.18	103.88
12H	103.2	9.36	112.55
13H	112.7	10.42	123.11
14H	122.2	10.19	132.38
15H	131.7	8.31	140.01
16H	141.2	9.57	150.77
17H	150.7	11.24	161.94
18H	160.2	10.98	171.18
19H	169.7	12.53	182.23
20H	179.2	12.15	191.35
21H	188.7	13.21	201.90
22H	198.2	14.20	212.40
23H	207.7	15.65	223.35
24H	217.2	15.03	232.23
25H	226.7	16.28	242.97
26H	236.2	16.45	252.65
27X	245.7	16.45	262.15
28X	250.9	16.45	267.35
198-1209B-			
1H	0.0	0.12	0.12
2H	5.1	–0.06	5.04
3H	14.6	0.61	15.21
4H	24.1	1.49	25.59
5H	33.6	3.72	37.32
6H	43.1	5.92	49.02
7H	52.6	6.11	58.71
8H	62.1	6.57	68.67
9H	71.6	7.63	79.23
10H	81.1	7.73	88.83
11H	90.6	10.13	100.73
12H	100.1	10.86	110.96
13H	109.6	9.86	119.46
14H	119.1	10.26	129.36
15H	128.6	10.96	139.56
16H	138.1	9.39	147.49
17H	147.6	10.83	158.43
18H	157.1	11.62	168.72
19H	166.6	12.06	178.66
20H	176.1	11.95	188.05
21H	185.6	13.52	199.12
22H	195.1	14.81	209.91
23H	204.6	15.66	220.26
24H	214.1	14.89	228.99
25H	223.6	16.47	240.07
26H	233.1	18.74	251.84
27H	242.6	18.74	261.34
28H	252.1	18.74	270.84
29H	261.6	18.74	280.34
30H	271.1	18.74	289.84
31H	280.6	18.74	299.34
32H	290.1	18.74	308.84
33H	297.6	18.74	316.34
198-1209C-			
1H	98.0	9.66	107.66
2H	107.5	9.81	117.31
3H	117.0	11.34	128.34
4H	126.5	10.45	136.95
5H	136.0	8.76	144.76
6H	145.5	9.73	155.23
7H	155.0	11.62	166.62
8H	164.5	12.12	176.62
9H	174.0	13.06	187.06
10H	183.5	15.29	198.79
11H	193.0	13.91	206.91
12H	202.5	15.57	218.07
13H	212.0	16.84	228.84
14H	221.5	16.16	267.66
15H	231.0	16.63	214.37
16H	240.5	16.63	257.13
17H	250.0	16.63	266.63
18H	252.5	16.63	269.13
19H	262.0	16.63	278.63
20H	268.4	16.63	285.03
21H	277.9	16.63	294.53
22H	287.4	16.63	287.40
23X	299.7	16.63	316.33

Table T7. Splice tie points, Site 1209.

Core, section, interval (cm)	Depth (mbsf)	Depth (mcd)		Core, section, interval (cm)	Depth (mbsf)	Depth (mcd)
198-				198-		
1209B-1H-2, 144	2.94	3.06	Tie to	1209A-1H-3, 6	3.06	3.06
1209A-1H-6, 6	7.06	7.06	Tie to	1209B-2H-2, 51	7.12	7.06
1209B-2H-7, 45	14.55	14.49	Tie to	1209A-2H-5, 21	14.41	14.49
1209A-2H-6, 75	16.45	16.53	Tie to	1209B-3H-1, 132	15.92	16.53
1209B-3H-7, 6	23.66	24.27	Tie to	1209A-3H-3, 51	21.21	24.27
1209A-3H-6, 108	26.28	29.34	Tie to	1209B-4H-3, 75	27.85	29.34
1209B-4H-6, 87	32.47	33.96	Tie to	1209A-4H-3, 9	30.29	33.96
1209A-4H-6, 24	34.94	38.61	Tie to	1209B-5H-1, 129	34.89	38.61
1209B-5H-5, 96	40.56	44.28	Tie to	1209A-5H-3, 72	40.42	44.28
1209A-5H-6, 117	45.37	49.23	Tie to	1209B-6H-1, 21	43.31	49.23
1209B-6H-6, 60	51.20	57.12	Tie to	1209A-6H-5, 21	52.41	57.12
1209A-6H-7, 42	55.62	60.33	Tie to	1209B-7H-2, 12	54.22	60.33
1209B-7H-5, 114	59.74	65.85	Tie to	1209A-7H-3, 114	59.84	65.85
1209A-7H-6, 105	64.25	70.26	Tie to	1209B-8H-2, 9	63.69	70.26
1209B-8H-7, 48	71.58	78.15	Tie to	1209A-8H-5, 36	71.56	78.15
1209A-8H-6, 141	74.11	80.70	Tie to	1209B-9H-1, 147	73.07	80.70
1209B-9H-7, 27	80.87	88.50	Tie to	1209A-9H-5, 18	80.88	88.50
1209A-9H-7, 36	84.06	91.68	Tie to	1209B-10H-2, 135	83.95	91.68
1209B-10H-6, 111	89.71	97.44	Tie to	1209A-10H-4, 45	89.15	97.44
1209A-10H-7, 60	93.80	102.09	Tie to	1209B-11H-1, 135	91.96	102.09
1209B-11H-5, 48	97.08	107.21	Tie to	1209A-11H-3, 33	97.03	107.21
1209A-11H-6, 90	102.10	112.28	Tie to	1209B-12H-1, 132	101.42	112.28
1209B-12H-5, 135	107.45	118.31	Tie to	1209C-2H-1, 99	108.50	118.31
1209C-2H-6, 6	115.06	124.87	Tie to	1209A-13H-2, 25	114.45	124.87
1209A-13H-5, 30	119.00	129.42	Tie to	1209C-3H-1, 108	118.08	129.42
1209C-3H-6, 114	125.64	136.98	Tie to	1209A-14H-4, 8.5	126.79	136.98
1209A-14H-6, 42	130.12	140.31	Tie to	1209C-4H-3, 36	129.86	140.31
1209C-4H-3, 69	130.19	140.64	Tie to	1209B-15H-1, 108	129.68	140.64
1209B-15H-6, 30	136.40	147.36	Tie to	1209A-15H-5, 135	139.05	147.36
1209A-15H-6, 75	139.95	148.26	Tie to	1209B-16H-1, 76.5	138.87	148.26
1209B-16H-3, 72	141.82	151.21	Tie to	1209A-16H-1, 43.5	141.64	151.21
1209A-16H-7, 55	149.54	159.11	Tie to	1209C-6H-3, 87	149.38	159.11
1209C-6H-6, 87	153.17	162.90	Tie to	1209A-17H-1, 96	151.66	162.90
1209A-17H-6, 72	158.92	170.16	Tie to	1209B-18H-1, 144	158.54	170.16
1209B-18H-5, 15	163.25	174.87	Tie to	1209A-18H-3, 69	163.89	174.87
1209A-18H-7, 27	168.76	179.74	Tie to	1209B-19H-1, 108	167.68	179.74
1209B-19H-5, 18	172.78	184.84	Tie to	1209A-19H-2, 111	172.31	184.84
1209A-19H-6, 84	178.04	190.57	Tie to	1209B-20H-2, 102	178.62	190.57
1209B-20H-5, 123	183.33	195.28	Tie to	1209A-20H-3, 93	183.13	195.28
1209A-20H-6, 102	187.72	199.87	Tie to	1209C-10H-1, 108	184.58	199.87
1209C-10H-7, 27	192.77	208.06	Tie to	1209C-11H-1, 114	194.15	208.06
1209C-11H-6, 93	201.43	215.34	Tie to	1209A-22H-2, 144	201.14	215.34
1209A-22H-5, 144	205.64	219.84	Tie to	1209C-12H-2, 27	204.27	219.84
1209C-12H-7, 39	211.39	226.96	Tie to	1209A-23H-3, 60	211.31	226.96
1209A-23H-6, 54	215.74	231.39	Tie to	1209C-13H-2, 105	214.55	231.39
1209C-13H-7, 27	221.27	238.11	Tie to	1209A-24H-4, 138	223.08	238.11
1209A-24H-7, 57	226.77	241.80	Tie to	1209C-14H-3, 114	225.64	241.80
1209C-14H-7, 33	230.83	246.99	Tie to	1209A-25H-3, 99.5	230.71	246.99
1209A-25H-6, 100	235.20	251.48	Tie to	1209C-15H-3, 84	234.85	251.48
1209C-15H-7, 117	240.67	257.30				

Table T8. Linear sedimentation rate segments used to calculate mass accumulation rates and average accumulation rates.

	Depth (mbsf)		Age (Ma)			Average accumulation rate (g/cm^2/k.y.)		
Segment	Top	Bottom	Top	Bottom	Age	Bulk sediment	Carbonate	Noncarbonate
1	0.00	78.31	0.0	5.8	late Miocene–Pleistocene	1.2	0.9	0.3
2	92.50	105.70	10.5	11.2	middle Miocene	1.9	1.7	0.2
3	105.70	111.48	15.1	16.4	middle Miocene	0.5	0.4	0.1
4	113.77	128.67	29.9	33.7	late Eocene–early Oligocene	0.4	0.4	0.0
5	128.67	143.27	33.7	43.7	middle Eocene–late Eocene	0.2	0.2	0.0
6	143.27	184.25	43.7	51.5	early Eocene–middle Eocene	0.6	0.6	0.0
7	184.25	195.59	51.5	54.7	late Paleocene–early Eocene	0.4	0.4	0.0
8	195.59	219.73	54.7	59.7	late Paleocene	0.6	0.5	0.1
9	219.73	232.34	59.7	63.0	early Paleocene–late Paleocene	0.4	0.4	0.0
10	232.34	235.59	63.0	65.0	early Paleocene	NA	NA	NA
11	235.59	264.89	65.0	68.6	late Maastrichtian	1.0	0.9	0.0
12	264.89	288.82	68.6	69.6	early Maastrichtian–late Maastrichtian	2.7	NA	NA

Note: NA = no dry bulk density or carbonate concentration data available.

Table T9. Concentrations of CH_4 in headspace gas, Hole 1209A.

Core, section, interval (cm)	Depth (mbsf)	CH_4 (ppmv)
198-1209A-		
1H-5, 0–5	6.00	1.9
2H-5, 0–5	14.20	2.3
3H-5, 0–5	23.70	2.1
4H-5, 0–5	33.20	2.2
5H-5, 0–5	42.70	2.0
6H-5, 0–5	52.20	1.9
7H-5, 0–5	61.70	2.3
8H-5, 0–5	71.20	1.9
9H-5, 0–5	80.70	2.2
10H-5, 0–5	90.20	1.9
11H-5, 0–5	99.70	1.9
12H-5, 0–5	109.20	1.9
13H-5, 0–5	118.70	1.9
14H-5, 0–5	128.20	1.9
15H-5, 0–5	137.70	1.9
17H-5, 0–5	156.70	1.9
18H-4, 0–5	164.70	1.8
21H-2, 0–5	190.20	1.7
24H-5, 0–5	223.20	1.7
25H-5, 0–5	232.70	1.7
27X-2, 0–5	247.20	1.8

Table T10. Carbonate content, Hole 1209A.

Core, section, interval (cm)	Depth (mbsf)	Total carbon (wt%)	$CaCO_3$ (wt%)
198-1209A-			
1H-1, 37–38	0.37	6.6	55.3
1H-2, 21–22	1.71	7.6	63.2
1H-4, 68–69	5.18	10.1	84.1
1H-6, 21–22	7.21	10.2	85.2
2H-1, 139–140	9.59	7.7	63.9
2H-4, 72–73	13.42	8.2	68.1
2H-5, 119–120	15.39	6.2	52.0
2H-5, 137–138	15.57	8.8	73.3
3H-1, 87–88	18.57	8.6	71.6
3H-3, 72–73	21.42	6.4	53.5
3H-4, 71–72	22.91	10.0	83.2
4H-1, 71–72	27.91	9.0	75.3
4H-3, 96–97	31.16	7.3	61.2
4H-4, 29–30	31.99	7.5	62.2
4H-4, 115–116	32.85	7.0	57.9
5H-1, 73–74	37.43	8.6	71.4
5H-3, 73–74	40.43	10.2	84.6
6H-4, 73–74	51.43	11.0	91.3
7H-2, 73–74	57.93	8.5	71.0
7H-3, 73–74	59.43	10.3	85.6
8H-5, 137–138	72.57	11.0	91.6
8H-6, 74–75	73.44	4.6	38.4
9H-1, 13–14	74.83	7.0	58.4
9H-1, 107–108	75.77	10.9	90.9
9H-4, 32–33	79.52	10.4	86.3
10H-1, 75–76	84.95	7.4	62.0
10H-3, 70–71	87.90	8.8	73.4
10H-5, 60–61	90.80	10.7	89.2
11H-2, 83–84	96.03	5.2	43.5
11H-5, 70–71	100.40	10.8	89.8
12H-2, 73–74	105.43	10.3	85.8
12H-4, 45–46	108.15	0.6	4.9
12H-4, 68–69	108.38	9.6	79.7
12H-4, 97–98	108.67	9.3	77.2
12H-5, 73–74	109.93	10.5	87.3
12H-6, 104–105	111.74	11.0	91.6
13H-1, 74–75	113.44	11.2	93.1
13H-4, 74–75	117.94	11.4	94.6
15H-1, 66–67	132.36	11.1	92.1
15H-7, 19–20	140.39	6.3	52.1
16H-5, 36–37	146.85	11.1	92.3
16H-6, 83–84	148.82	11.4	95.3
17H-2, 72–73	152.92	11.5	95.6
17H-5, 31–32	157.01	11.5	95.8
17H-6, 73–74	158.93	10.7	89.1
18H-2, 73–74	162.43	11.6	96.7
18H-3, 72–73	163.92	11.4	95.0
19H-4, 68–69	174.88	11.4	94.5
19H-6, 70–71	177.90	11.6	96.2
20H-1, 66–67	179.86	11.4	95.1
20H-2, 73–74	181.43	11.6	96.3
20H-5, 73–74	185.93	11.5	95.4
20H-7, 19–20	188.39	8.6	71.6
22H-2, 65–66	200.35	9.7	81.0
22H-6, 73–74	206.43	11.6	96.4
23H-1, 73–74	208.43	11.5	95.8
23H-3, 74–75	211.44	11.0	91.3
23H-5, 75–76	214.45	11.4	94.7
24H-2, 48–49	219.18	11.4	94.8
24H-5, 13–12	223.32	10.3	86.0
24H-5, 73–74	223.93	11.6	96.5
26H-1, 90–91	237.10	11.6	96.6
26H-4, 62–63	241.32	11.6	96.6
27X-1, 73–74	246.43	11.7	97.1
27X-3, 73–74	249.43	11.6	96.9
28X-1, 70–71	251.60	11.6	96.3
28X-3, 72–73	254.62	11.6	96.9

Table T11. Results of geochemical analyses, Hole 1209A.

Core, section, interval (cm)	Depth (mbsf)	pH	Alkalinity (mM)	Salinity	Cl^- (mM)	SO_4^{2-} (mM)	Na^+ (mM)	Mg^{2+} (mM)	Ca^{2+} (mM)	K^+ (mM)	H_4SiO_4 (µM)	NH_4^+ (µM)	HPO_4^{2-} (µM)	Sr^{2+} (µM)	Fe^{2+} (µM)	Mn^{2+} (µM)	Li^+ (µM)	Ba^{2+} (µM)	H_3BO_3 (µM)
198-1209A-																			
1H-4, 145–150	5.95	7.54	3.1	35.0	551	28.1	473	52.3	10.8	11.8	610	59	2.8	104	46.7	8.1	22.2	1.3	458
2H-4, 145–150	14.15	7.40	2.9	35.0	552	27.0	469	53.0	11.2	11.7	583	57	0.9	132	43.2	6.4	20.4	0.3	435
3H-4, 145–150	23.65	7.37	3.3	35.0	556	27.3	473	52.7	11.9	11.9	637	64	0.8	169	20.0	2.7	19.1	0.3	437
4H-4, 145–150	33.15	7.37	3.3	35.0	558	26.2	477	51.1	11.6	11.6	698	61	0.9	200	17.3	1.7	19.2	0.3	446
5H-4, 145–150	42.65	7.20	3.3	35.0	557	25.9	476	50.4	11.8	11.5	698	64	0.8	221	16.3	1.2	18.2	0.6	434
6H-4, 145–150	52.15	7.37	3.2	35.0	558	25.3	478	49.5	11.7	11.3	654	60	0.6	238	19.4	1.2	18.3	1.5	446
7H-4, 140–150	61.60	7.12	3.1	35.0	556	25.1	476	48.8	12.1	11.3	631	56	0.3	249	22.9	0.9	17.5	0.2	442
8H-4, 140–150	71.10	7.41	3.1	35.0	558	25.2	478	49.0	12.1	11.3	625	54	0.5	260	14.5	1.6	17.8	0.3	431
9H-4, 140–150	80.60	7.30	3.1	35.0	562	24.7	481	48.6	12.7	11.1	606	47	0.3	271	16.7	2.7	18.5	0.3	434
10H-4, 140–150	90.10	7.30	2.9	35.0	557	24.8	476	47.8	13.6	11.0	568	40	0.3	286	19.9	8.9	20.6	0.2	431
11H-4, 140–150	99.60	7.37	2.9	35.0	558	24.4	477	47.7	13.2	10.5	511	29	0.3	278	27.7	7.2	21.8	0.7	432
15H-4, 140–150	137.65	7.43	2.6	35.0	561	24.3	479	47.3	14.0	10.2	287	21	0.2	283	18.3	2.4	28.7	0.7	461
18H-3, 140–150	164.60	7.41	2.5	35.0	569	24.3	484	47.4	15.3	10.2	228	23	0.2	300	28.9	0.9	41.7	0.3	469
27X-1, 145–150	247.15	7.47	2.2	35.0	560	23.5	478	44.8	15.7	9.9	197	46	0.2	334	11.1	1.7	69.0	0.6	465

Table T12. Discrete index properties measurements, Holes 1209A and 1209B. (Continued on next two pages.)

Core, section, interval (cm)	Depth (mbsf)	Water content (wt%)		Density (g/cm^3)			Porosity (%)	Void ratio
		Bulk mass	Dry mass	Bulk	Dry	Grain		
198-1209A-								
1H-1, 74–76	0.74	47.5	90.5	1.52	0.80	2.72	70.6	2.41
1H-2, 70–72	2.20	53.0	112.7	1.44	0.68	2.68	74.7	2.95
1H-3, 70–72	3.70	45.6	83.9	1.54	0.84	2.67	68.6	2.19
1H-4, 70–72	5.20	47.5	90.4	1.53	0.80	2.77	71.0	2.45
1H-5, 70–72	6.70	47.2	89.5	1.53	0.81	2.71	70.3	2.37
1H-6, 70–72	7.70	44.7	80.9	1.56	0.86	2.68	67.9	2.12
2H-1, 70–72	8.90	45.2	82.4	1.56	0.85	2.71	68.6	2.18
2H-2, 70–72	10.40	47.2	89.6	1.54	0.81	2.78	70.8	2.43
2H-3, 70–72	11.90	46.6	87.2	1.55	0.83	2.79	70.4	2.38
2H-4, 70–72	13.40	43.3	76.3	1.60	0.91	2.81	67.6	2.09
2H-5, 70–72	14.90	42.4	73.8	1.61	0.92	2.76	66.6	1.99
2H-6, 65–67	16.35	41.4	70.7	1.61	0.94	2.69	64.9	1.85
2H-7, 45–47	17.65	47.9	91.9	1.54	0.80	2.85	71.9	2.56
3H-1, 70–72	18.40	46.2	85.8	1.55	0.84	2.79	70.1	2.34
3H-2, 70–72	19.90	48.1	92.7	1.53	0.80	2.85	72.1	2.58
3H-3, 70–72	21.40	48.1	92.6	1.51	0.79	2.70	71.0	2.44
3H-4, 70–72	22.90	39.9	66.5	1.64	0.99	2.75	64.1	1.78
3H-5, 70–72	24.40	45.9	85.0	1.56	0.84	2.79	69.9	2.32
3H-6, 70–72	25.90	39.7	65.9	1.64	0.99	2.70	63.5	1.74
4H-1, 70–72	27.90	42.1	72.8	1.60	0.93	2.71	65.8	1.92
4H-2, 61–63	29.31	43.0	75.6	1.59	0.90	2.72	66.8	2.01
4H-3, 69–71	30.89	42.4	73.6	1.61	0.93	2.79	66.7	2.00
4H-4, 70–72	32.40	46.4	86.7	1.53	0.82	2.68	69.4	2.27
4H-5, 70–72	33.90	43.0	75.5	1.59	0.91	2.74	66.8	2.02
4H-6, 70–72	35.40	41.8	71.9	1.61	0.94	2.73	65.7	1.92
5H-1, 70–72	37.40	46.1	85.5	1.54	0.83	2.70	69.3	2.25
5H-2, 70–72	38.90	40.9	69.2	1.61	0.95	2.66	64.2	1.80
5H-3, 70–72	40.40	41.3	70.4	1.61	0.94	2.69	64.9	1.85
5H-4, 76–78	41.96	41.6	71.2	1.61	0.94	2.71	65.3	1.88
5H-5, 73–75	43.43	44.1	78.7	1.58	0.88	2.75	67.9	2.12
5H-6, 70–72	44.90	40.9	69.2	1.63	0.96	2.73	64.9	1.85
5H-7, 46–48	46.16	40.7	68.6	1.63	0.96	2.72	64.6	1.82
6H-1, 70–72	46.90	40.5	68.0	1.63	0.97	2.73	64.4	1.81
6H-2, 70–72	48.40	40.9	69.3	1.61	0.95	2.67	64.4	1.81
6H-3, 70–72	49.90	41.3	70.4	1.60	0.94	2.63	64.4	1.81
6H-4, 70–72	51.40	39.5	65.2	1.64	0.99	2.70	63.2	1.72
6H-5, 70–72	52.90	42.0	72.3	1.60	0.93	2.70	65.6	1.91
6H-6, 70–72	54.40	42.5	74.0	1.58	0.91	2.66	65.8	1.93
7H-1, 70–72	56.40	42.7	74.4	1.59	0.91	2.69	66.2	1.96
7H-2, 70–72	57.90	48.9	95.7	1.50	0.77	2.71	71.7	2.53
7H-3, 70–72	59.40	41.4	70.6	1.61	0.94	2.70	65.0	1.86
7H-4, 70–72	60.90	39.2	64.4	1.65	1.00	2.73	63.2	1.72
7H-5, 70–72	62.40	40.6	68.3	1.64	0.97	2.79	65.0	1.86
7H-6, 70–72	63.90	39.4	64.9	1.65	1.00	2.75	63.5	1.74
8H-1, 70–72	65.90	44.1	79.0	1.57	0.88	2.72	67.7	2.10
8H-2, 70–72	67.40	39.5	65.4	1.63	0.99	2.67	63.0	1.70
8H-3, 70–72	68.90	42.7	74.7	1.60	0.91	2.74	66.6	2.00
8H-4, 68–70	70.38	40.3	67.4	1.63	0.98	2.72	64.2	1.79
8H-5, 70–72	71.90	39.7	65.8	1.64	0.99	2.71	63.5	1.74
8H-6, 70–72	73.40	49.3	97.2	1.49	0.76	2.68	71.7	2.54
9H-1, 70–72	75.40	44.5	80.3	1.57	0.87	2.72	68.0	2.13
9H-2, 68–70	76.88	41.0	69.4	1.63	0.96	2.74	65.0	1.86
9H-3, 70–72	78.40	43.1	75.6	1.60	0.91	2.79	67.4	2.06
9H-4, 71–73	79.91	40.8	69.1	1.62	0.96	2.72	64.7	1.83
9H-5, 70–72	81.40	40.4	67.7	1.63	0.97	2.73	64.4	1.81
9H-6, 70–72	82.90	40.1	66.9	1.65	0.99	2.77	64.4	1.81
10H-1, 60–62	84.80	38.7	63.2	1.66	1.02	2.73	62.8	1.69
10H-2, 70–72	86.40	41.2	70.0	1.62	0.95	2.73	65.1	1.87
10H-3, 70–72	87.90	39.7	66.0	1.65	0.99	2.75	63.9	1.77
10H-4, 70–72	89.40	39.6	65.6	1.64	0.99	2.72	63.6	1.74
10H-5, 70–72	90.90	37.5	60.1	1.70	1.06	2.80	62.2	1.64
10H-6, 70–72	92.40	39.3	64.9	1.65	1.00	2.74	63.4	1.74
11H-1, 70–72	94.40	40.3	67.4	1.64	0.98	2.76	64.5	1.81
11H-2, 70–72	95.90	45.5	83.6	1.55	0.84	2.69	68.7	2.19
11H-3, 70–72	97.40	39.7	66.0	1.64	0.99	2.71	63.6	1.74
11H-4, 70–72	98.90	41.3	70.3	1.62	0.95	2.73	65.2	1.88

Table T12 (continued).

Core, section, interval (cm)	Depth (mbsf)	Water content (wt%)		Density (g/cm³)			Porosity (%)	Void ratio
		Bulk mass	Dry mass	Bulk	Dry	Grain		
11H-5, 70–72	100.40	37.7	60.5	1.69	1.05	2.77	62.1	1.64
11H-6, 70–72	101.90	39.1	64.1	1.66	1.01	2.74	63.2	1.71
12H-1, 70–72	103.90	39.5	65.4	1.64	0.99	2.72	63.4	1.73
12H-2, 70–72	105.40	38.5	62.6	1.67	1.03	2.74	62.6	1.67
12H-3, 70–72	106.90	40.9	69.2	1.62	0.96	2.73	64.9	1.85
12H-4, 90–92	108.60	36.3	57.0	1.70	1.08	2.73	60.3	1.52
12H-5, 70–72	109.90	37.3	59.4	1.69	1.06	2.74	61.3	1.59
12H-6, 100–102	111.70	34.2	52.1	1.74	1.14	2.73	58.2	1.39
13H-1, 70–72	113.40	34.9	53.6	1.72	1.12	2.72	58.7	1.42
13H-2, 70–72	114.90	35.0	53.7	1.71	1.11	2.68	58.5	1.41
13H-3, 70–72	116.40	36.5	57.5	1.70	1.08	2.73	60.5	1.53
13H-4, 70–72	117.90	34.9	53.5	1.73	1.13	2.74	58.8	1.43
13H-5, 70–72	119.40	35.5	55.1	1.71	1.10	2.71	59.3	1.46
13H-6, 70–72	120.90	35.4	54.8	1.71	1.11	2.71	59.2	1.45
15H-1, 70–72	132.40	31.7	46.3	1.79	1.23	2.75	55.4	1.24
15H-2, 70–72	133.90	29.1	41.1	1.84	1.30	2.73	52.2	1.09
15H-3, 70–72	135.40	33.9	51.3	1.74	1.15	2.72	57.7	1.36
15H-5, 70–72	138.40	34.6	52.9	1.72	1.13	2.69	58.1	1.39
15H-6, 70–72	139.90	34.1	51.7	1.74	1.15	2.73	57.9	1.38
15H-7, 68–70	140.88	34.2	51.9	1.73	1.14	2.71	57.8	1.37
16H-2, 70–72	142.69	35.9	56.0	1.71	1.09	2.73	59.8	1.49
16H-3, 70–72	144.19	35.2	54.3	1.73	1.12	2.75	59.3	1.46
16H-4, 70–72	145.69	36.9	58.5	1.70	1.07	2.75	61.1	1.57
16H-5, 70–72	147.19	35.7	55.5	1.71	1.10	2.73	59.6	1.48
16H-6, 50–52	148.49	36.8	58.3	1.69	1.07	2.74	60.9	1.56
17H-1, 70–72	151.40	36.5	57.5	1.69	1.07	2.69	60.2	1.51
17H-2, 70–72	152.90	32.5	48.2	1.77	1.19	2.72	56.1	1.28
17H-3, 70–72	154.40	33.0	49.3	1.76	1.18	2.71	56.6	1.31
17H-4, 70–72	155.90	32.9	49.1	1.78	1.19	2.78	57.1	1.33
17H-5, 70–72	157.40	34.1	51.7	1.74	1.15	2.72	57.8	1.37
17H-6, 70–72	158.90	34.9	53.5	1.72	1.12	2.71	58.6	1.42
18H-1, 70–72	160.90	30.0	42.8	1.82	1.28	2.74	53.4	1.15
18H-2, 70–72	162.40	29.9	42.6	1.84	1.29	2.78	53.7	1.16
18H-3, 70–72	163.90	31.8	46.6	1.81	1.24	2.82	56.2	1.28
18H-4, 20–22	164.90	31.3	45.6	1.80	1.24	2.76	55.1	1.23
18H-6, 94–96	167.93	30.2	43.2	1.83	1.28	2.76	53.8	1.17
19H-1, 70–72	170.40	33.6	50.7	1.77	1.17	2.80	58.1	1.38
19H-2, 70–72	171.90	34.0	51.5	1.74	1.15	2.72	57.8	1.37
19H-3, 70–72	173.40	32.7	48.6	1.77	1.19	2.73	56.5	1.30
19H-4, 70–72	174.90	32.9	49.0	1.77	1.19	2.75	56.8	1.31
19H-5, 70–72	176.40	30.7	44.2	1.82	1.26	2.77	54.5	1.20
19H-6, 70–72	177.90	28.3	39.5	1.86	1.33	2.74	51.4	1.06
20H-1, 70–72	179.90	29.7	42.2	1.83	1.28	2.72	52.9	1.12
20H-2, 70–72	181.40	25.5	34.1	1.93	1.44	2.76	47.9	0.92
20H-3, 70–72	182.90	28.8	40.5	1.84	1.31	2.71	51.7	1.07
20H-4, 70–72	184.40	32.6	48.4	1.77	1.19	2.74	56.5	1.30
20H-5, 70–72	185.90	31.7	46.3	1.79	1.22	2.74	55.3	1.24
20H-6, 70–72	187.40	31.3	45.5	1.79	1.23	2.73	54.8	1.21
22H-1, 70–72	198.90	29.2	41.3	1.83	1.29	2.70	52.1	1.09
22H-2, 70–72	200.40	32.2	47.5	1.77	1.20	2.70	55.6	1.25
22H-3, 70–72	201.90	31.2	45.4	1.79	1.23	2.72	54.7	1.21
22H-7, 29–31	206.99	31.2	45.3	1.79	1.23	2.71	54.6	1.20
23H-1, 70–72	208.40	32.8	48.8	1.77	1.19	2.74	56.6	1.30
23H-2, 70–72	209.90	31.2	45.3	1.79	1.23	2.70	54.4	1.20
23H-3, 70–72	211.40	32.5	48.2	1.76	1.19	2.70	56.0	1.27
23H-4, 70–72	212.90	32.9	49.0	1.76	1.18	2.70	56.4	1.29
23H-5, 70–72	214.40	30.6	44.0	1.81	1.26	2.74	54.0	1.18
23H-6, 70–72	215.90	31.4	45.9	1.80	1.23	2.75	55.2	1.23
24H-1, 70–72	217.90	31.6	46.2	1.79	1.22	2.72	55.1	1.23
24H-2, 70–72	219.40	32.7	48.7	1.77	1.19	2.73	56.5	1.30
24H-3, 70–72	220.90	32.2	47.5	1.77	1.20	2.71	55.7	1.26
24H-4, 70–72	222.40	32.4	47.8	1.77	1.20	2.71	55.9	1.27
24H-5, 70–72	223.90	33.2	49.8	1.75	1.17	2.70	56.8	1.31
24H-6, 70–72	225.40	34.5	52.8	1.72	1.13	2.70	58.1	1.39
26H-1, 70–72	236.90	31.8	46.6	1.79	1.22	2.73	55.4	1.24
26H-2, 70–72	238.40	32.4	48.0	1.78	1.20	2.74	56.3	1.29
26H-3, 70–72	239.90	31.3	45.5	1.80	1.23	2.73	54.9	1.22
26H-4, 70–72	241.40	31.2	45.4	1.78	1.23	2.69	54.4	1.19
26H-7, 48–50	245.68	31.7	46.5	1.79	1.22	2.74	55.5	1.25

Table T12 (continued).

Core, section, interval (cm)	Depth (mbsf)	Water content (wt%)		Density (g/cm³)			Porosity (%)	Void ratio
		Bulk mass	Dry mass	Bulk	Dry	Grain		
27X-1, 69–71	246.39	34.4	52.3	1.74	1.14	2.75	58.4	1.41
27X-2, 70–72	247.90	32.7	48.5	1.76	1.18	2.69	56.0	1.28
27X-3, 70–72	249.40	32.1	47.3	1.77	1.20	2.71	55.6	1.25
27X-4, 70–72	250.90	33.0	49.3	1.77	1.18	2.74	56.9	1.32
28X-1, 70–72	251.60	35.4	54.7	1.71	1.10	2.68	58.9	1.43
28X-2, 70–72	253.10	33.7	50.8	1.74	1.16	2.71	57.3	1.34
28X-3, 70–72	254.60	35.7	55.4	1.70	1.10	2.69	59.3	1.46
28X-4, 70–72	256.10	34.5	52.7	1.73	1.14	2.73	58.4	1.41
198-1209B-								
27H-1, 70–72	243.30	31.7	46.4	1.77	1.21	2.68	54.9	1.22
27H-2, 70–72	244.80	31.3	45.6	1.79	1.23	2.72	54.7	1.21
27H-3, 70–72	246.30	31.9	46.9	1.77	1.20	2.67	55.0	1.22
27H-4, 70–72	247.80	33.2	49.7	1.74	1.16	2.67	56.4	1.30
27H-5, 70–72	249.30	32.9	49.1	1.74	1.17	2.66	56.1	1.28
27H-6, 70–72	250.80	33.6	50.7	1.74	1.16	2.71	57.3	1.34
31H-1, 70–72	281.30	35.2	54.2	1.72	1.12	2.72	59.0	1.44
31H-2, 70–72	282.80	34.6	53.0	1.75	1.15	2.81	59.3	1.45
31H-3, 70–72	284.30	35.2	54.4	1.72	1.11	2.71	59.0	1.44
31H-4, 70–72	285.80	35.0	53.7	1.73	1.12	2.74	58.9	1.44
31H-5, 70–72	287.30	33.4	50.2	1.76	1.17	2.74	57.3	1.34
31H-6, 65–67	288.75	34.5	52.7	1.73	1.14	2.73	58.4	1.40

Table T13. Discrete measurements of *P*-wave velocity, Site 1209. (Continued on next two pages.)

Core, section, interval (cm)	Depth (mbsf)	Velocity (m/s)
198-1209A-		
1H-1, 70	0.70	1495.7
1H-2, 67	2.17	1488.4
1H-3, 67	3.67	1503.2
1H-4, 66	5.16	1508.3
1H-5, 66	6.66	1493.4
1H-6, 35	7.35	1498.4
2H-1, 77	8.97	1522.9
2H-2, 76	10.46	1501.2
2H-3, 76	11.96	1523.8
2H-4, 75	13.45	1516.9
2H-5, 76	14.96	1528.2
2H-6, 61	16.31	1522.0
2H-7, 40	17.60	1516.8
3H-1, 67	18.37	1516.7
3H-2, 67	19.87	1523.6
3H-3, 67	21.37	1521.5
3H-4, 76	22.96	1523.8
3H-5, 67	24.37	1503.1
3H-6, 66	25.86	1518.6
4H-1, 75	27.95	1510.5
4H-2, 58	29.28	1510.8
4H-3, 62	30.82	1512.5
4H-4, 77	32.47	1503.0
4H-5, 76	33.96	1511.6
4H-6, 78	35.48	1504.0
5H-1, 67	37.37	1521.6
5H-2, 66	38.86	1517.4
5H-3, 68	40.38	1524.1
5H-4, 84	42.04	1516.0
5H-5, 78	43.47	1511.1
5H-6, 66	44.86	1527.0
5H-7, 43	46.13	1530.0
6H-1, 66	46.86	1525.2
6H-2, 66	48.36	1531.1
6H-3, 65	49.85	1526.5
6H-4, 66	51.36	1519.0
6H-5, 67	52.87	1526.8
6H-6, 65	54.35	1515.8
7H-1, 65	56.35	1517.5
7H-2, 64	57.83	1505.2
7H-3, 66	59.35	1516.9
7H-4, 62	60.82	1520.4
7H-5, 65	62.35	1521.4
7H-6, 64	63.84	1535.7
8H-1, 63	65.83	1514.1
8H-2, 77	67.47	1538.9
8H-3, 66	68.86	1517.6
8H-4, 61	70.31	1525.1
8H-5, 65	71.85	1521.3
8H-6, 66	73.36	1524.2
9H-1, 67	75.37	1519.8
9H-2, 65	76.85	1531.9
9H-3, 67	78.37	1520.9
9H-4, 67	79.87	1527.4
9H-5, 65	81.35	1522.4
9H-6, 67	82.87	1517.5
10H-1, 56	84.76	1532.1
10H-2, 66	86.36	1504.8
10H-3, 67	87.87	1534.0
10H-4, 67	89.37	1529.6
10H-5, 67	90.87	1527.7
10H-6, 65	92.35	1520.0
11H-1, 66	94.36	1519.5
11H-2, 64	95.84	1515.8
11H-3, 66	97.36	1522.5
11H-4, 66	98.86	1521.7
11H-5, 67	100.37	1531.6
11H-6, 67	101.86	1535.6
12H-1, 75	103.95	1531.3
12H-2, 67	105.37	1521.3
12H-3, 77	106.97	1520.8
12H-4, 96	108.66	1535.9
12H-5, 75	109.95	1535.1
12H-6, 105	111.75	1551.7
13H-1, 66	113.36	1538.0
13H-2, 65	114.85	1542.1
13H-3, 66	116.36	1536.2
13H-4, 63	117.83	1534.1
13H-5, 64	119.34	1541.9
13H-6, 64	120.84	1545.2
14H-1, 63	122.83	1553.6
14H-2, 74	124.43	1543.7
14H-3, 70	125.90	1544.0
14H-4, 70	127.40	1552.7
14H-5, 76	128.96	1550.6
14H-6, 72	130.42	1570.6
15H-1, 65	132.35	1574.3
15H-2, 64	133.84	1588.4
15H-3, 63	135.33	1550.9
15H-5, 64	138.34	1557.2
15H-6, 64	139.84	1556.0
15H-7, 33	140.53	1561.9
16H-2, 65	142.64	1544.0
16H-3, 65	144.13	1539.5
16H-4, 65	145.64	1530.3
16H-5, 66	147.15	1538.4
16H-6, 45	148.44	1525.0
17H-1, 62	151.32	1541.5
17H-2, 62	152.82	1545.1
17H-3, 63	154.33	1552.7
17H-4, 60	155.80	1561.2
17H-5, 63	157.33	1550.6
17H-6, 62	158.82	1553.3
18H-1, 65	160.85	1560.1
18H-2, 63	162.33	1583.2
18H-3, 64	163.84	1549.2
18H-4, 14	164.84	1552.7
19H-1, 64	170.34	1544.9
19H-2, 63	171.83	1553.4
19H-3, 62	173.32	1539.7
19H-4, 63	174.82	1549.1
19H-5, 64	176.34	1565.9
19H-6, 64	177.84	1587.5
20H-1, 63	179.83	1554.5
20H-2, 65	181.35	1553.9
20H-3, 65	182.85	1549.5
20H-4, 62	184.32	1553.7
20H-5, 65	185.85	1554.2
20H-6, 65	187.35	1555.3
21H-1, 71	189.41	1566.1
21H-2, 74	190.93	1598.8
21H-3, 73	192.43	1563.6
21H-5, 63	195.33	1558.5
21H-6, 73	196.93	1555.3
21H-7, 21	197.91	1545.7
21H-7, 38	198.08	1545.8
22H-1, 62	198.82	1576.0
22H-2, 62	200.32	1580.9
22H-3, 61	201.81	1573.4
22H-7, 34	207.04	1569.3
23H-1, 61	208.31	1568.5
23H-2, 60	209.80	1569.4
23H-3, 56	211.26	1556.1
23H-4, 77	212.97	1559.1
23H-5, 61	214.31	1570.7
23H-6, 60	215.80	1565.5
24H-1, 62	217.82	1584.0
24H-2, 63	219.33	1567.9
24H-3, 63	220.83	1557.9
24H-4, 56	222.26	1568.9
24H-5, 63	223.83	1554.5
24H-6, 62	225.32	1548.0
25H-1, 70	227.40	1556.0
25H-3, 67	230.37	1555.2
25H-4, 60	231.80	1585.7
25H-5, 74	233.44	1640.0
25H-6, 81	235.01	1635.2
25H-7, 33	236.03	1557.2
26H-1, 62	236.82	1552.1
26H-2, 60	238.30	1549.4
26H-3, 61	239.81	1560.3
26H-4, 64	241.34	1570.8
26H-7, 42	245.62	1560.6
27X-1, 61	246.30	1544.4
27X-2, 64	247.84	1554.9
27X-3, 65	249.35	1557.9
27X-4, 63	250.83	1549.0
28X-1, 61	251.51	1531.4
28X-2, 64	253.04	1548.2
28X-3, 66	254.56	1557.1
28X-4, 65	256.05	1548.4
198-1209B-		
1H-1, 61	0.61	1548.4
1H-2, 71	2.21	1514.2
1H-3, 50	3.50	1514.4
1H-4, 46	4.46	1514.0
2H-1, 67	5.77	1498.9
2H-2, 66	7.26	1506.8
2H-3, 60	8.70	1516.5
2H-4, 65	10.25	1516.8
2H-5, 72	11.82	1520.2
2H-6, 60	13.20	1513.9
3H-1, 71	15.31	1506.9
3H-2, 70	16.80	1513.1
3H-3, 70	18.30	1515.3
3H-4, 80	19.90	1519.2
3H-5, 77	21.37	1518.5
3H-6, 75	22.85	1515.4
3H-7, 39	23.99	1514.4
4H-1, 59	24.69	1499.6
4H-2, 71	26.31	1508.2
4H-3, 75	27.85	1523.7
4H-4, 68	29.28	1525.9
4H-5, 66	30.76	1507.9
4H-6, 73	32.33	1521.1
5H-1, 86	34.46	1509.5
5H-2, 65	35.74	1521.5
5H-3, 55	37.15	1518.5
5H-4, 54	38.64	1517.5
5H-5, 72	40.32	1528.5
5H-6, 74	41.84	1525.8
5H-7, 54	43.14	1520.6
6H-1, 70	43.80	1517.2
6H-2, 68	45.28	1514.1
6H-3, 66	46.76	1531.0
6H-4, 77	48.37	1525.6
6H-5, 73	49.83	1523.5
6H-6, 80	51.40	1527.9
6H-7, 38	52.48	1518.6
7H-1, 74	53.34	1540.4
7H-2, 69	54.78	1509.2
7H-3, 76	56.36	1518.9
7H-4, 91	58.01	1518.3

Table T13 (continued).

Core, section, interval (cm)	Depth (mbsf)	Velocity (m/s)
7H-5, 75	59.35	1515.7
7H-6, 73	60.83	1521.4
7H-7, 34	61.94	1515.9
8H-1, 68	62.78	1534.0
8H-2, 75	64.35	1522.5
8H-3, 75	65.85	1523.3
8H-4, 68	67.28	1528.3
8H-5, 70	68.80	1514.5
8H-6, 72	70.32	1530.4
8H-7, 38	71.48	1542.3
9H-1, 73	72.33	1530.5
9H-2, 65	73.75	1529.6
9H-3, 66	75.26	1517.0
9H-4, 73	76.83	1538.2
9H-5, 74	78.34	1531.0
9H-6, 73	79.83	1537.4
9H-7, 33	80.93	1543.0
10H-1, 66	81.76	1537.2
10H-2, 73	83.33	1526.9
10H-3, 75	84.85	1533.5
10H-4, 74	86.34	1526.1
10H-5, 72	87.82	1525.5
10H-6, 62	89.22	1539.2
10H-7, 26	90.36	1523.4
11H-1, 68	91.28	1520.9
11H-2, 76	92.86	1527.0
11H-3, 58	94.18	1518.0
11H-4, 80	95.90	1526.9
11H-5, 75	97.35	1532.2
11H-6, 72	98.82	1517.1
11H-7, 39	99.99	1545.4
12H-1, 67	100.77	1547.3
12H-2, 76	102.36	1535.4
12H-3, 80	103.90	1541.7
12H-4, 71	105.31	1532.4
12H-5, 75	106.85	1527.3
12H-6, 57	108.17	1543.7
12H-7, 28	109.38	1538.1
13H-1, 77	110.37	1599.6
13H-2, 79	111.89	1549.8
13H-4, 61	114.71	1569.9
13H-5, 74	116.34	1531.3
13H-6, 72	117.82	1540.1
13H-7, 40	119.00	1557.8
14H-1, 91	120.01	1552.4
14H-2, 80	121.40	1532.6
14H-3, 63	122.73	1538.8
14H-4, 78	124.38	1557.2
14H-5, 66	125.76	1548.7
14H-6, 83	127.43	1554.7
15H-1, 66	129.26	1543.9
15H-2, 70	130.80	1551.9
15H-3, 68	132.28	1569.3
15H-4, 104	134.14	1591.0
15H-5, 110	135.70	1558.8
15H-6, 53	136.63	1566.5
16H-1, 82	138.92	1597.1
16H-2, 67	140.27	1539.5
16H-3, 72	141.82	1533.7
16H-4, 67	143.27	1538.9
16H-5, 68	144.78	1536.2
16H-6, 50	146.10	1538.5
17H-1, 60	148.20	1559.4
17H-2, 65	149.75	1554.5
17H-3, 57	151.17	1549.7
17H-4, 69	152.79	1545.7
17H-5, 75	154.35	1547.4
17H-6, 77	155.87	1554.7
18H-1, 89	157.99	1553.3
18H-2, 66	159.26	1541.3
18H-3, 81	160.91	1554.2
18H-4, 82	162.42	1556.1
18H-5, 95	164.05	1562.9
18H-6, 78	165.38	1553.2
19H-1, 76	167.36	1579.5
19H-2, 67	168.77	1571.8
19H-3, 65	170.25	1573.2
19H-4, 71	171.81	1581.9
19H-5, 72	173.32	1563.7
19H-6, 60	174.70	1572.5
20H-1, 63	176.73	1573.4
20H-2, 73	178.33	1589.2
20H-3, 66	179.76	1566.5
20H-4, 73	181.33	1577.1
20H-5, 72	182.82	1571.3
20H-6, 69	184.29	1562.3
21H-1, 53	186.13	1566.8
21H-2, 91	188.01	1583.9
21H-3, 77	189.37	1576.6
21H-4, 70	190.80	1577.5
21H-5, 79	192.39	1556.5
21H-6, 71	193.81	1566.3
22H-2, 76	197.36	1557.3
22H-3, 82	198.92	1577.6
22H-4, 73	200.33	1548.2
22H-5, 86	201.96	1561.9
22H-6, 81	203.41	1558.7
23H-1, 78	205.38	1602.6
23H-2, 78	206.88	1576.2
23H-3, 71	208.31	1562.9
23H-4, 81	209.90	1552.2
23H-5, 75	211.35	1582.1
23H-6, 80	212.90	1574.3
23H-7, 32	213.92	1571.0
24H-1, 70	214.80	1573.1
24H-2, 72	216.32	1572.7
24H-3, 73	217.83	1568.7
24H-6, 71	222.31	1577.2
24H-7, 36	223.46	1560.9
25H-1, 74	224.34	1570.0
25H-2, 75	225.85	1560.6
25H-3, 66	227.26	1552.1
25H-4, 67	228.77	1554.6
25H-5, 79	230.39	1565.5
25H-6, 69	231.79	1576.1
25H-7, 36	232.96	1578.3
26H-1, 56	233.66	1561.7
26H-2, 63	235.23	1546.5
26H-3, 67	236.77	1558.2
26H-4, 50	238.10	1557.8
27H-1, 87	243.47	1570.5
27H-2, 63	244.73	1562.1
27H-3, 62	246.22	1567.1
27H-4, 63	247.73	1552.1
27H-5, 62	249.22	1548.9
27H-6, 62	250.72	1546.6
28H-1, 66	252.76	1547.8
28H-2, 71	254.31	1546.0
28H-3, 81	255.91	1544.5
28H-4, 82	257.42	1544.7
28H-5, 72	258.82	1551.2
28H-6, 65	260.24	1556.6
29H-1, 68	262.28	1549.2
29H-2, 76	263.86	1549.1
29H-3, 85	265.45	1560.0
29H-4, 76	266.86	1544.6
29H-5, 76	268.36	1551.9
29H-6, 74	269.84	1554.4
30H-1, 90	271.99	1575.9
30H-2, 68	273.28	1562.2
30H-3, 78	274.88	1551.3
30H-4, 74	276.23	1575.8
30H-5, 68	277.61	1556.8
30H-6, 44	278.87	1567.9
31H-1, 64	281.24	1573.9
31H-2, 54	282.64	1575.9
31H-3, 61	284.20	1554.1
31H-4, 61	285.71	1563.5
31H-5, 64	287.24	1559.5
31H-6, 58	288.68	1568.0
32H-1, 73	290.83	1571.3
32H-2, 65	292.25	1579.4
32H-3, 64	293.74	1541.9
32H-4, 73	295.33	1565.5
32H-5, 69	296.79	1553.7
32H-6, 45	298.05	1565.7
198-1209C-		
1H-1, 67	98.67	1521.9
1H-2, 75	100.25	1521.4
1H-3, 61	101.61	1538.5
1H-4, 67	103.17	1538.4
1H-5, 66	104.66	1536.5
1H-6, 81	106.31	1542.4
1H-7, 41	107.41	1547.1
2H-1, 78	108.28	1546.0
2H-2, 69	109.69	1522.3
2H-3, 77	111.27	1545.5
2H-4, 72	112.72	1538.2
2H-5, 71	114.21	1523.1
2H-6, 78	115.78	1533.2
2H-7, 36	116.86	1541.9
3H-1, 73	117.73	1556.0
3H-2, 73	119.23	1544.1
3H-3, 70	120.70	1540.3
3H-4, 77	122.27	1545.2
3H-5, 76	123.76	1547.6
3H-6, 72	125.22	1560.1
4H-1, 74	127.24	1551.5
4H-2, 76	128.76	1546.6
4H-3, 79	130.29	1568.1
4H-4, 71	131.71	1557.7
4H-5, 73	133.23	1569.0
4H-6, 55	134.55	1562.1
5H-1, 73	136.73	1545.1
5H-2, 77	138.27	1536.4
5H-3, 76	139.76	1545.8
5H-4, 81	141.31	1549.8
5H-5, 68	142.68	1547.8
5H-6, 77	144.27	1540.3
6H-1, 64	146.14	1552.0
6H-2, 69	147.68	1542.1
6H-3, 66	149.16	1535.2
6H-4, 67	150.67	1545.7
6H-5, 16	151.66	1568.0
6H-6, 76	153.06	1538.3
6H-7, 61	154.41	1561.1
7H-1, 67	155.66	1564.1
7H-2, 66	157.16	1550.7
7H-3, 70	158.70	1548.4
7H-4, 69	160.19	1552.5
7H-5, 69	161.69	1559.3
7H-6, 78	163.28	1567.1
8H-1, 62	165.12	1563.4
8H-2, 64	166.63	1579.5
8H-3, 68	168.18	1572.9
8H-4, 70	169.70	1569.6

Table T13 (continued).

Core, section, interval (cm)	Depth (mbsf)	Velocity (m/s)
8H-5, 70	171.20	1553.2
8H-6, 70	172.70	1555.0
9H-1, 76	174.76	1554.0
9H-2, 70	176.20	1557.0
9H-3, 67	177.67	1561.5
9H-4, 64	179.14	1589.2
9H-5, 62	180.62	1583.9
9H-6, 62	182.12	1564.1
10H-1, 75	184.25	1585.8
10H-2, 66	185.66	1557.2
10H-3, 64	187.14	1566.7
10H-4, 71	188.71	1560.9
10H-5, 76	190.26	1566.4
10H-6, 60	191.60	1559.0
10H-7, 35	192.85	1571.4
11H-1, 62	193.62	1575.2
11H-2, 75	195.25	1564.5
11H-3, 69	196.69	1559.9
11H-4, 63	198.13	1552.8
11H-5, 77	199.77	1574.1
11H-6, 64	201.14	1582.0
12H-1, 66	203.16	1564.8
12H-2, 70	204.70	1572.4
12H-3, 71	206.21	1579.3
12H-4, 83	207.83	1569.0
12H-5, 63	209.13	1565.2
12H-6, 48	210.48	1559.4
13H-1, 70	212.70	1548.6
13H-2, 67	214.16	1560.8
13H-3, 71	215.71	1568.9
13H-4, 61	217.10	1560.0
13H-5, 73	218.73	1554.0
13H-6, 69	220.19	1566.2
13H-7, 42	221.42	1577.6
14H-1, 72	222.22	1568.5
14H-2, 76	223.76	1553.3
14H-3, 75	225.25	1557.4
14H-4, 77	226.77	1559.1
14H-5, 73	228.23	1549.3
14H-6, 73	229.73	1542.1
14H-7, 35	230.85	1553.7
15H-1, 72	231.71	1583.1
15H-2, 75	233.24	1602.8
15H-4, 82	235.82	1576.3
15H-5, 80	237.30	1584.4
15H-6, 65	238.65	1566.7
15H-7, 49	239.99	1554.6
16H-1, 86	241.36	1564.4
16H-2, 70	242.70	1564.8
16H-3, 75	244.25	1564.0
16H-4, 71	245.71	1557.5
16H-5, 72	247.22	1552.0
16H-6, 68	248.68	1545.1
17H-1, 69	250.69	1547.9
18H-1, 72	253.22	1537.4
18H-2, 72	254.72	1555.4
18H-3, 66	256.16	1553.5
18H-4, 61	257.61	1564.4
18H-5, 63	259.13	1555.9
18H-6, 64	260.64	1558.2
19H-1, 66	262.66	1549.7
19H-2, 67	264.17	1548.3
20H-1, 66	269.06	1580.0
20H-2, 75	270.65	1560.3
20H-3, 70	272.10	1575.4
20H-4, 75	273.65	1570.1
20H-5, 63	275.03	1574.3
20H-6, 62	276.52	1579.9
21H-1, 75	278.65	1573.7
21H-2, 91	280.31	1581.7
21H-3, 64	281.54	1573.3
21H-4, 68	283.08	1568.5
21H-5, 67	284.57	1585.3
21H-6, 43	285.83	1577.3
21H-7, 35	286.55	1590.8
22H-2, 88	289.78	1595.7
22H-3, 80	291.20	1594.6
22H-4, 61	292.51	1580.6
22H-5, 70	294.10	1584.2
22H-6, 80	295.70	1580.0

Table T14. Discrete measurements of thermal conductivity, Holes 1209A and 1209B.

Core, section, interval (cm)	Depth (mbsf)	Thermal conductivity (W/[m·K])
198-1209A-		
1H-1, 55	0.55	0.89
1H-3, 55	3.55	0.90
2H-1, 55	8.75	0.99
2H-3, 60	11.80	0.99
3H-1, 55	18.25	1.09
3H-3, 55	21.25	0.95
4H-1, 55	27.75	1.05
4H-3, 55	30.75	1.03
5H-1, 55	37.25	1.03
5H-3, 55	40.25	1.09
6H-1, 55	46.75	1.09
6H-3, 55	49.75	1.09
7H-1, 55	56.25	1.03
7H-3, 55	59.25	0.94
8H-1, 55	65.75	1.03
8H-3, 55	68.75	1.12
9H-1, 55	75.25	0.96
9H-3, 55	78.25	1.14
10H-1, 55	84.75	1.08
10H-3, 55	87.75	1.14
11H-1, 55	94.25	1.12
11H-3, 55	97.25	1.15
12H-1, 55	103.75	1.10
12H-3, 55	106.75	1.16
13H-1, 55	113.25	1.25
13H-3, 55	116.25	1.14
14H-1, 55	122.75	0.94
14H-3, 55	125.75	0.99
15H-1, 55	132.25	0.92
15H-3, 55	135.25	1.31
16H-1, 55	141.75	1.11
16H-3, 55	144.04	1.09
17H-1, 55	151.25	1.07
17H-3, 55	154.25	1.26
18H-1, 55	160.75	1.13
18H-3, 55	163.75	1.09
19H-1, 55	170.25	0.97
19H-3, 55	173.25	1.20
20H-1, 55	179.75	1.04
20H-3, 55	182.75	1.32
21H-1, 55	189.25	1.13
21H-3, 55	192.25	1.31
22H-1, 55	198.75	1.12
22H-3, 55	201.75	1.15
23H-1, 55	208.25	1.07
23H-3, 55	211.25	1.32
24H-1, 55	217.75	1.22
24H-3, 55	220.75	1.17
25H-1, 55	227.25	1.26
25H-3, 55	230.25	1.27
26H-1, 55	236.75	1.28
26H-3, 55	239.75	1.33
27X-1, 55	246.25	1.17
27X-3, 55	249.25	1.31
28X-1, 55	251.45	1.21
28X-3, 55	254.45	1.19
198-1209B-		
8H-1, 55	62.65	1.18
8H-3, 55	65.65	1.09
10H-1, 55	81.65	0.95
10H-3, 55	84.65	1.16
12H-1, 55	100.65	1.15
12H-3, 55	103.65	1.15

Table T15. In situ Adara temperature tool measurements, Hole 1209B.

Depth (mbsf)	Bottom-water temperature (°C)	Sediment thermal conductivity* (W/[m·K])	Sediment temperature (°C)
0	2.2†	NA	NA
71.6	NA	1.14	4.3
90.6	NA	1.06	4.8
109.6	NA	1.15	4.9

Notes: * = see Table **T14,** p. 101, for sediment thermal conductivity values. † = mean of six calculations, using seawater thermal conductivity of 1.2 W/[m·K]. NA = not applicable.